1-5-2017

Biophysics of Dendritic Spine Morphogenesis

Olena Marchenko
Uconn Health Center, marchenko.olena@gmail.com

Biophysics of Dendritic Spine Morphogenesis

Olena O. Marchenko, PhD

University of Connecticut, 2017

Dendritic spines receive the majority of synaptic inputs in the mammalian central nervous system and constitute the foundation for a healthy nervous system. Cognitive and motor delays, and other symptoms of impaired neurodevelopment are associated with abnormal dendritic spine shape and densities. Understanding of spine stability and spine formation in neurodevelopmental conditions remains elusive. Spine formation is determined by the stability of its transient precursor: the dendritic filopodium. First, we aim to understand dendritic filopodium motility and stability mechanism that underlies its transition into a spine. We hypothesized that mechanical feedback among the actin retrograde flow, myosin activity and substrate adhesion gives rise to various filopodial behaviors. We have formulated a minimal one-dimensional partial differential equation model that reproduces the range of observed motility. The model predicts the response of the system to each of these experimental perturbations, supporting the hypothesis that our actomyosin-driven mechanism controls dendritic filopodia dynamics and therefore identifies the main parameters in spine formation and stability. Spine development is deficient in Angelman (AS) and overabundant in Dup15q Syndromes as suggested by the corresponding animal models. In human cells, the phenotypic outcome and the timepoint in neurodevelopment at which the phenotype emerges, have not previously been studied. Therefore, we investigated dendritic spine morphology in Dup15q and AS human induced pluripotent stem cell (hiPSC)-derived neurons, characterizing filopodia motility, spine shape, maturation and neurite branching at different time points of development. Our findings suggest that the first phenotypic differences in Dup15q Syndrome arise during early neurodevelopment at week 7 with increased dendritic filopodia density and protrusion/retraction rates compared to control. We further show that the spine number and density are increased in Dup15q and decreased in AS. For future studies, syndrome-specific spine formation can be explored with a morphologically realistic 2-dimensional partial differential equation model of a dendritic spine solved on moving boundaries.

Biophysics of Dendritic Spine Morphogenesis

Olena O. Marchenko

B.A., Colby College, 2010

A Dissertation

Submitted in Partial Fulfillment of the

Requirements for the Degree of

Doctor of Philosophy

at the

University of Connecticut

2017

APPROVAL PAGE

Doctor of Philosophy Dissertation

Biophysics of Dendritic Spine Morphogenesis

Presented by

Olena O. Marchenko, B.A.

Major Advisor _____
Leslie M. Loew

Associate Advisor _____
Vladimir I. Rodionov

Associate Advisor _____
Charles W. Wolgemuth

Associate Advisor _____
Stormy J. Chamberlain

University of Connecticut
2017

Acknowledgements

I am very grateful to Dr. Les Loew for the opportunity to learn under his mentorship, for his patience, advice and training. Through his dedication to science, hard work and unlimited drive for new frontiers Dr. Loew has become a great scientist model for me.

I am extremely lucky to have had an opportunity to work in Dr. Stormy Chamberlain lab during Stem Cell project. I am grateful for the detailed feedback, zealous approach to data analysis and valuable advice that I have gotten there. I couldn't have done it without the help of Dr. Noelle Germain who taught me numerous subtleties of working with stem cells and performing neurodifferentiation.

I am very grateful to Dr. Wolgemuth for taking time to teach me mathematical, physical and philosophical aspects of the applications of Fluid Dynamics in the biological world of low Reynolds numbers. I have learned a lot about modeling biological systems and continue to come back to our lectures throughout the years of my PhD training.

I am especially thankful to Dr. Rodionov for his collaboration, mentorship, support and guidance during all my years of training as a PhD student. Dr. Rodionov always has helpful suggestions and his office door was always open for me when I had questions on experiments, writing or science in general.

Dedication

To my husband Igor and my children, Ariel and Esther, who are my sources of strength.

To my dad, who is no longer with us, but who shared with me love to all creatures and the great mystery that is life.

Table of Contents

List of Figures and Tables……x

List of Abbreviations……xii

Chapter 1. Introduction

1.1 Role of Dendritic Filopodia in Dendritic Spine Development**……...2**

1.2 Dendritic Spine Pathology in Neurodevelopmental Disorders**…….. 3**

1.3 Mathematical Models of Dendritic Spines and Filopodia**……..6**

Figures**……9**

Bibliography**…….16**

Chapter 2. Mechanism of Dendritic Filopodia Motility.

2.1 Introduction**……19**

2.2 Formulation of a model based on experimental constraints **…….24**

2.3 Parameter Estimation for the Dendritic Filopodia Model**…….27**

2.4 The Model Can Recapitulate Experimentally Observed Behaviors**…….30**

2.4.1. Actin Polymerization Rate Regulates Filopodia Motility**…….32**

2.4.2 The Effect of Substrate Adhesion on Filopodia Dynamics is Biphasic**…….33**

2.4.3 Dendritic Filopodia Lengths and Motility are Increased by Blebbistatin Treatment**…….35**

2.5 Discussion**……..37**

2.6 Materials and Methods**……..42**

Bibliography**……...46**

Figures……**50**

Supplemental Materials……..**63**

List of Supplementary Movies…….…..**68**

Legends to Supplementary Movies……**70**

Chapter 3. FiloTracker – High-throughput Software for Tracking Subcellular Structures

3.1 Introduction……..**71**

3.2 Description of FiloTracker Algorithm……**72**

3.3 Algorithm Validation……..…**74**

Figures……...**75**

Bibliography……..…...**78**

Chapter 4. Dendritic Spine Morphogenesis in Dup15q and Angelman Syndrome.

4.1 Introduction…….....**79**

4.2 Results…….....**81**

4.2.1 Process Arborization is Increased in Dup15q and Decreased in Angelman Patient iPSC-derived Neurons at 28 weeks…….....**81**

4.2.2. Dendritic spine density is increased in Dup15q and decreased in Angelman patient iPSC-derived neurons at 28 weeks…….**82**

4.2.3. Dendritic filopodia density and motility is increased in Dup15q Syndrome neurons at 7 weeks……..…...**82**

4.3 Discussion……...**83**

4.4 Materials and Methods……..….**85**

Figures…….**90**

List of Supplemental Movies…….……**94**

Bibliography…….**98**

Chapter 5. Conclusions and Suggestions for Future Research: Preliminary study of 2D Model

5.1 Proceedings from the Results of the Previous Chapters……..**102**

5.2 2D Model Formulation and Governing Equations……...**104**

5.3 Preliminary Results on Fixed Boundary…….**106**

5.4 Integrating UBE3A and RhoA Signaling into Spine Morphology Model…….....**107**

Figures……...**108**

Bibliography……..**112**

List of Tables and Figures

1.1 Dendritic Filopodium Transition into Spine……..9

1.2 Spine Shapes and Densities…….....10

1.3 Signaling pathways in the Dendritic Spine……...11

1.4 AS and Dup15q Genetics……..13

1.5 Actin Cytoskeleton Motility Models……..15

2.1. Analysis of filopodia motility with automated tracking software FiloTracker…….53

2.2. Cartoon that illustrates the balance of forces in a dendritic filopodium described by the minimal model……54

2.3. Model solutions correspond to experimental data…….55

2.4 Localization of myosin (MLC) in dendrites using PALM imaging……56

2.5. Filopodia dynamics depends on the resistive force applied at the base by the microtubule network…….57

2.6 Effect of actin polymerization rate on filopodial motility……58

2.7 pLL-substrate adhesion strength regulates filopodial motility…….59

2.8 Dependence of filopodial lengths and retraction rates on myosin Kd……..60

2.9 Summary of filopodium non-motile and motile behavior mechanisms……61

2.10 Table Parameter values for nominal case……63

2.11 Montage of sequential phase-contrast images…….64

2.12 Sensitivity analysis for parameters , Tκ, β……..65

2.13 Nocodazole treatment reduces filopodia motility and number…….66

2.14 Cytochaasin D and DMSO treatment do not impact cytoskeleton integrity……67

3.1 Screenshot of the FiloTracker software…….....75

3.2 FiloTracker Workflow……....76

3.3 Software validation with artificial filopodium……77

3.4 Software validation with handtracking……78

4.1 Occurrence of ASD and Intellectual Disability in General Population……..90

4.2 Dup15q Syndrome Genetic Map and Cell Lines……92

4.3 Schematized protocols for neurodifferentiation used for Dendritic Filopodia Motility and Morphology Analysis. ……..93

4.4 Live imaging of transfected cells for Sholl Analysis…….94

4.5 Morphology Analysis in control, Angelman and Dup15q neurons at 28 weeks……95

4.6 Dendritic Protrusion Density Analysis in Dup15q, Angelman and control neurons at 28 weeks……96

4.7 Filopodia Density and Motility in iPSC-derived Dup15q and Control lines at 7 weeks ……...97

5.1 Cartoon description of Dendritic spine 2D Model……....109

5.2 Boundary conditions for 2D spine…….110

5.3 Distribution of bound myosin (A) and actin polymerization (B)……..111

5.4 Model of Spine Morphogenesis…….112

List of abbreviations

ARF – actin retrograde flow

ASD – Autism Spectrum Disorder

AS - chromosome 15q11-q13.1 deletion syndrome

Dup15q - chromosome 15q11-q13.1 duplication syndrome

FXS – Fragile X Syndrome

PSD-95 – postsynaptic density

MAP2 – microtubule associated protein 2

SK2 - Small conductance calcium-activated potassium channel

WT- wild type

EB - embryoid body

NMDA receptor - N-methyl-D-aspartate receptor

AMPA receptor - α-amino-3-hydroxy-5-methyl-4-isoxazolepropionic acid receptor

LTP – long term potentiation

LTD – long term depression

DIV - days in vitro,

PLL – poly-L-lysine,

RT – room temperature,

MLC – myosin light chain,

PALM – photoactivated localization microscopy.

BDNF -brain-derived neurotrophic factor

MAPK - mitogen-activated protein kinase)

PI3K - phosphoinositide 3-kinase

PTEN - phosphatase and tensin homologue

TSC - tuberous sclerosis,

FMRP - fragile X mental retardation protein

F-actin – filamentous actin

CDC42 -cell division control protein 42

RAC1 -Ras-related C3 botulinum toxin substrate 1

PAKs -p21-activated kinases

PSD95 - postsynaptic density protein of 95 kDa

1D – one-dimensional

2D – two-dimensional

ODE – ordinary differential equations

PDE – partial differential equations

Chapter 1

Introduction[1]

The mammalian nervous system is one of the most intricate biological structures known. This continuously evolving interconnected cell network with inherent ability to create and retain information makes our brain a fascinating subject to study.

Formation of synapses and their maintenance are required for correct functioning of neuronal circuitry. The majority of synaptic inputs in CNS is received by dendritic spines, a micrometer-scale protrusion that emanate from the neuronal dendrites (Figure 1.1). They morph from filopodia protrusions into a variety of shapes routinely classified as stubby, thin or mushroom. An average dendritic spine has a length of 1-2 μm (but up to 6 μm in CA3 area of hippocampus), has a head volume between 0.1 and 0.8 μm^3(Harris 1999) and a neck diameter between 0.09 to 0.51 μm (Arellano et al. 2007). Spines are typically found in a linear density of 1-10 spines per μm of dendrite in an adult brain(Harris 1999). Abnormal spine shape density and spine morphology have been associated with impaired motor and cognitive functions, underlying neurodevelopmental disorders such as Autism Spectrum Disorder (ASD), tuberous sclerosis, Schizophrenia, Fragile-X syndrome (FXS)(Purpura 1974; Comery et al. 1997; Yasuda et al. 2014; Toro et al. 2010)(Figure 1.2). While phenotypical outcomes of dendritic spines are important for study and classification of brain pathologies, the events that take place during neurodevelopment and disruptions that lead to the functional defects remain elusive, and this knowledge is required for the development of novel therapeutic venues. This chapter provides background on dendritic spine structure formation in the context of neurodevelopment and neurodevelopmental disorders.

[1] Section 1.3 Mathematical Models of Dendritic Spine and Filopodia is a part of chapter Modeling Actin Dynamics Borinskaya S., Marchenko O., Loew LM (2016). In *Encyclopedia of Cell Biology* Vol 4., pp10-12

1.1 Role of Dendritic Filopodia in Dendritic Spine Development

Dendritic spine morphogenesis starts from development of precursor structures: dendritic filopodia. Filopodia are highly dynamic protrusions that sprout on neuronal dendrites to explore their extracellular environment and connect with presynaptic axons. The direct link between dendritic filopodia and dendritic spines formation was demonstrated in time sequence in live hippocampal slice culture(Ziv & Smith 1996) and morphology studies in serial electron microscopy studies(Harris 1999). All spines observed were matched with a filopodium precursor at an earlier developmental time point, but not all filopodia were replaced by mature spines later. Notably, most filopodia were motile during early neurogenesis (DIV11) and non-motile towards the end of the study (DIV28)(Ziv & Smith 1996). Postsynaptic density (PSD), ordinarily found in mature spines in functional synapses, was visualized in dendritic filopodia at the tip, middle or base. Thus, after filopodia retracted or stabilized, they were replaced with mushroom, stubby or shaft synapses as confirmed in slice culture in vitro and in first postnatal week in vivo.(Ziv & Smith 1996; Harris 1999).

Dendritic filopodia are filled with a branched actin network that undergoes constant remodeling during protrusion, retraction and maturation processes. Complex signaling cascades reorganize the actin cytoskeleton, which determines filopodia density, motility and sensitivity to the neighboring axons and include a wide variety of interlocking, antagonistic or redundant pathways (Lohmann & Bonhoeffer 2008; Kayser et al. 2008; Rubio et al. 2011). The eph-ephrin trans-synaptic signaling plays an important role in the spine development and maturation by clustering NMDA and AMPA glutamate receptors on the surface of dendritic spines. In filopodium, EhpB receptor tyrosine kinase localizes to the tip and works by phosphorylating guanine exchange factors (GEFs) Tiam1, kalirin-7, that activate Rho family GTPases Rac1 and Cdc42. Each of these molecules is a gatekeeper for signaling cascades that lead to actin cytoskeleton remodelling. For example, Cdc42 activates N-WASP and Arp2/3 complex that increase branching points on actin filaments, upregulating nucleation and promoting filopodium/spine head expansion(Yang & Svitkina 2011; Lohmann & Bonhoeffer 2008; Fiala et al. 1998). Similarly, Rac1 activation upregulates

actin polymerization by phosphorylation of p21-activated kinase(PAK)(Kayser et al. 2008). The same Rac1 molecule increases actin filament turnover by activation of LIMK1 and cofilin cascades and thus promoting filopodia motility and elongation, while RhoA downregulates both nucleation and elongation of filopodia thus working as an antagonist (Tashiro et al. 2000).

Besides the increased filopodial motility guided by the biochemical events described above, a physical contact between an axon and filopodium is required for the spine stabilization to take place and relies on physical events such as filopodial protrusion, retraction and adhesion to the substrate. For example, formation of spine-like structures enriched in actin was triggered by contacts between dendritic filopodia and N-cadherin–coated beads (Chazeau et al. 2015). However, the fundamental mechanism of filopodium dynamics and functional significance of filopodia motility for spine formation are unknown and can shed light on the process of spine stabilization and filopodia pruning. In the next chapter I define three types of filopodial motility and use pharmacological treatments and mathematical modeling to outline and test the proposed filopodia motility mechanism. The developed biophysical model of filopodia dynamics is a modeling platform for testing biochemical pathways implicated in filopodia dynamics.

1.2 Dendritic Spine Pathology in Neurodevelopmental Disorders.

After the dendritic filopodia stabilize and transform into spines, their malleable nature is conserved. Spines respond with shape changes to input from the connected axons, frequency of firing, ion channels and signaling receptors that populate the spine membrane. Integration of these events determines the short and long term changes to spine shape and size.(Hotulainen & Hoogenraad 2010; Chazeau et al. 2014). Dendritic spines change shape by pushing of polymerizing actin filaments against the lipid bilayer., and the rate of protrusion is controlled by myosin-mediated F-actin dissasembly in the spine neck. Therefore, as in filopodia, actin cytoskeleton rearrangements are directly related to spine shape and motility. Extensive studies have been published focusing on function of individual actin binding proteins (Tashiro et al. 2000; Saneyoshi et al. 2010; Rubio et al. 2011; Ivanov et al. 2009; Pi et al. 2010), and large-scale models have been developed that conglomerate all reactions on the actin network (Ditlev et al. 2009; Brown et al. 2011;

Kotaleski & Blackwell 2010). However, despite the vast knowledge available on the subject, it is unclear how synaptic function and actin cytoskeleton in dendritic spines are connected in a context of a neurological disease.

Dependent on synaptic activity, dendritic spine density undergoes variations during early neurogenesis at different rates among brain regions. In primate visual cortex maximum spine density is 90 synapses/100μm^3 of neuropil(Bourgeois & Rakic 1993) and is reached by the third postnatal month. 40% decrease in spine density takes place between 2.7 and 5 years primarily by loss of asymmetric synapses on dendritic spines and constitutes 40-50 synapses/100μm^3. The high density phase lasts longer (up to a year) in thalamus (Bourgeois & Rakic 1993). Region specific deviations from the normal course of neurodevelopment during any of those stages have been associated with cognitive and motor impairments in animal primate and human post-mortem studies(Bourgeois & Rakic 1993; Comery et al. 1997; Penzes et al. 2011). Nonetheless, distinguishing normal from pathological in dendritic spine shapes and density is still a great challenge in the field of neurodevelopment and begs for more attention and study tools.

Human chromosome 15q11.2-q13 region is implicated in a variety of neurodevelopmental disorders comorbid with autistic phenotypes and mental retardation (Hogart et al. 2010). Candidate genes that directly or indirectly influence synaptic function have been identified, however there is limited experimental evidence on the structural abnormalities in these cells. Dup15q and Angleman Syndromes are congenital neurodevelopmental conditions that arise due to duplications or deletions respectively in 15q11.2-q13 region and harbor genes directly and indirectly implicated in synapse function. (Pi et al. 2010; Yuste & Denk 1995; Hill & Zito 2013) thus paving a study ground for neurodevelopment.

Ubiquitin Protein Ligase E3A (UBE3A) is the main contender for impaired neurodevelopment in Angelman and Dup15q Syndromes. UBE3A deficiency causes Angelman syndrome (AS) whereas its overexpression is linked to an increased risk of autistic spectrum disorder (Weeber et al. 2003; Pignatelli et al. 2014; Sun et al. 2015; Yashiro et al. 2009; Chamberlain et al. 2010; Dindot et al. 2008). UBE3A directly ubiquitinates C2-terminal domain of small-conductance calcium-activated potassium channel SK2, thereby facilitating

its internalization. SKs participate in various CNS functions, from regulating neuronal intrinsic excitability to network rhythmic activity and higher brain functions. Membrane-associated synaptic SK2 levels are increased in UBE3A-deficient mouse and are correlated with reduced endocytotic SK2 levels compared to WT. Lack of internalized SK2 causes LTP impairment as shown by reduced actin polymerization after theta-burst stimulation in Angelman Syndrome mouse model (Sun et al. 2015).

Interaction with Ephexin5 is among many other functions of UBE3A. One set of receptors and ligands that appear to impact both the development and the mature function of synapses are Eph receptors (erythropoietin-producing human hepatocellular carcinoma cell line) and their surface associated ligands, ephrins (Eph family receptor interacting proteins). Ephs can initiate new synaptic contacts, recruit and stabilize glutamate receptors at nascent synapses and regulate dendritic spine morphology. EphrinB-Ephexin5-UBE3A provides direct regulation of spine density. Ephexin5 is a RhoA guanine nucleotide exchange factor that blocks synapse development until EphB receptor tyrosine kinase binds to EphrinB. This event triggers phosphorylation and degradation of Ephexin5 by UBE3A and mediates spine growth via Rac pathway.

The pathways described above are very likely to have an effect on dendritic spine morphology and density, and thus **we hypothesize that there is neuronal phenotype associated with the developmental disorders Angelman and Dup15q**. In chapter 4 we present preliminary data on neuron morphology studies in Dup15q and Angelman patient-specific neurons and its comparison to control individuals. These data in combination with electrophysiological and genetic studies will aid our understanding of AS, Dup15q and neurodevelopment in general. In the past years, the treatment of complex neurological disorders has been limited by discovery of few therapeutic agents, i.e. serotonin and dopamine D2 receptor antagonists. In the absence of reliable predictive parameters for assessment of medication responsiveness and lack of reproducible studies, the patients face frequent medication changes, polypharmacy with significant risk of combined side-effects, uncertainty of the treatment efficacy or no treatment at all(Parent & Anderson 2015; Vissers et al. 2015). Thus, the discovery of cellular phenotypes would directly facilitate drug discovery

experiments by providing a test platform and also help further investigation of neurological dysfunctions that unravel during neurodevelopment.

1.3 Mathematical Models of Dendritic Spines and Filopodia.

The complexity of the pathways that converge on actin cytoskeleton and mediate spine shape change and synaptic function is intractable and calls for interdisciplinary approach. Given that dendritic filopodia and spines are actin-rich structures, and the force due to actin filament pushing onto cellular membrane constitutes the basis for spine shape change, simulating the actin network rearrangement with the resulting forces is crucial for understanding spine stability and shape formation. As we have seen in the previous section, large biochemical networks converge on actin cytoskeleton to control its reorganization, which governs filopodia and spine structure and motility. Conceptual models of actin dynamics are typically minimal models focused on various biomechanical aspects of cell motility. The model is based on fundamental laws of thermodynamics and mechanics, specifically, on force balance within the cell cytoskeleton and mass conservation of actin. The treatment of the actin filament as an elastic spring launched a new generation of models that use familiar mechanical components to describe actin network flow and deformation: springs, dashpots, and motors(*Figure 1.5*). The differential treatment of G and F-actin anticipated the two-phase treatment of the cytosol which led to development of continuum models that integrate contractile stress, F-actin and cytosol flow with traction forces and cytoskeletal densities on the whole cell scale (Danuser et al. 2013)

The possibility that actin filament polymerization at the cell membrane is capable of generating protrusion force was first explained in the Brownian ratchet formalism derived by Peskin, Odel and Oster (Peskin et al., 1993) for the dependence of polymerization velocity on the effective load size. A study by Mogilner and Oster 1996 extended this hypothesis by considering an elastic filament; by including the bending fluctuations of the filament, they showed that the velocity is independent of the size of the cargo for situations where the polymerization rate is limiting (i.e. at low monomer concentrations) (Mogilner and Oster, 1996). This demonstrated a fundamental concept that polymerization rate remains largely the same

in various actin-driven motility scenarios and also led to models of microorganism motility, such as Listeria and Shigella. Since that study, actin network models of various complexity have been used by biophysicists for reproducing and understanding cell motility and cell shapes for decades. Dembo and colleagues developed a continuum model of the contractile and viscoelastic cytoplasm that considers a two-phase treatment of the cytosol and cytoskeleton components and their interaction with the cell membrane (Herant et al., 2003). To understand which components, fluid or solid, plays a major role in cell shape and locomotion, they develop two hypotheses for the active force generation on the cell membrane: cytoskeletal swelling force model and polymerization force model. A study by Wolgemuth et al. (2012) goes further adding moving-boundary algorithm to the model of keratocyte cell-shape dynamics. The main goal of the study is to understand how four seemingly redundant biochemical mechanisms that may underlie cell motility directly translate into changes in the cell shape and locomotion. Wolgemuth's study concludes that the redundancy in biochemical and biophysical mechanisms is necessary for robust cellular migration.

The conceptual modeling approach has been successful in solving shape and motility patterns in axon growth cone (Craig et al. 2012). Filopodia models have been proposed before (Mogilner & Rubinstein 2005; Yang & Svitkina 2011). However, since the models describe bundled actin filaments dynamics in conventional filopodia, they cannot be applied to simulate dendritic filopodia behavior. Furthermore, the models referenced above focus only on the processes involved in protrusion and initiation. Thus, we constructed our own minimal model on a moving boundary that can help understanding filopodia dynamics in relation to dendritic spine formation.

There are no published structural models of dendritic spine that can answer our questions. While the three-dimensional nature of the problem demands significant computational resources, and there is no stable algorithm to solve the PDE system accurately on a moving boundary, such model would be of benefit to the field of neurogenesis. First, it would enable to couple F-actin network reorganization to the signaling cascades that are activated as a result of LTP or LTD and model shape and motility changes in real-time. Second, it would allow simulation of the electrophysiological and pharmacological experiments. Finally,

and most importantly, it would allow simulation of outcomes of long-term experiments such as how dendritic spine morphogenesis changes in the course of neurodevelopment as a function of the genotype.

In chapter 5 we expand the filopodium 1D model proposed above to model the spine morphology in 2D. Next, we will test if the identified abnormalities in spine shape can be rescued by manipulating the substrate adhesion, actin polymerization pattern, myosin localization and/or actin myosin contractility parameters in our mathematical model. In future projects, the 2D biophysical model can be complemented with biochemical pathways of interest such as Rac-RhoA or CYFIP1-FMRP- armadillo protein p0071 to model dendritic spine morphology in neurodevelopmental disorders.

Figures

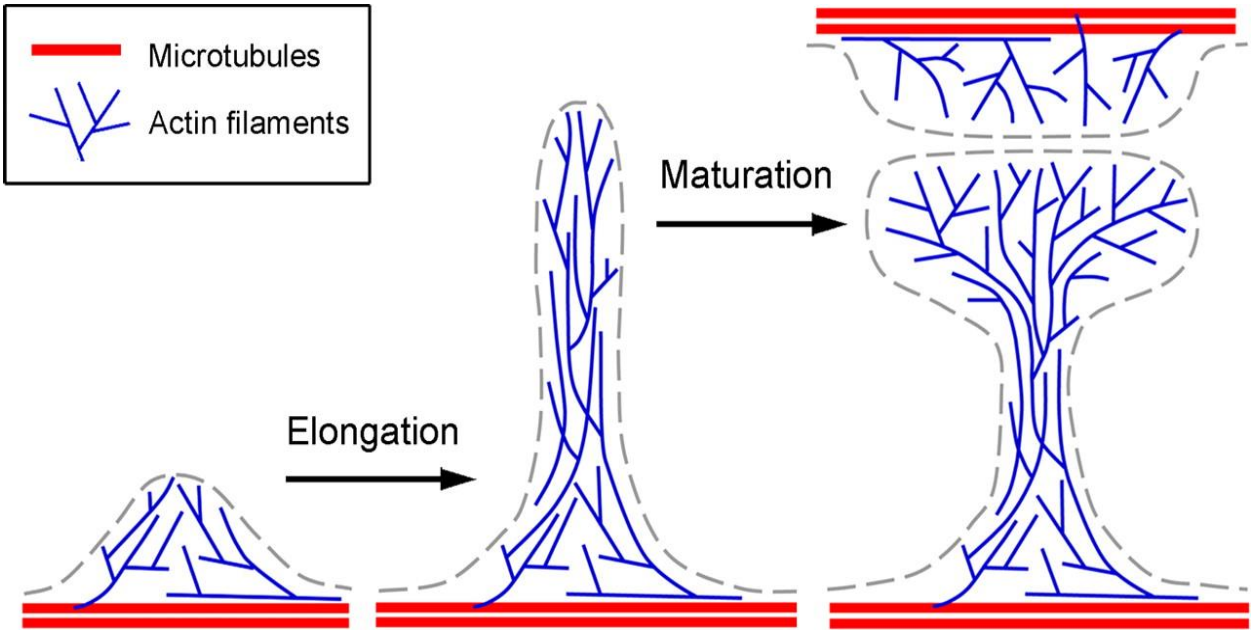

Figure 1.1 Dendritic filopodium transition into spine. Actin network rearrangement under influence of extracellular signaling and contact with the neighboring cells results in expansion into a dendritic spine head (Figure from Korobova & Svitkina 2010). Used with permission Copyright©2010 by The American Society for Cell Biology.

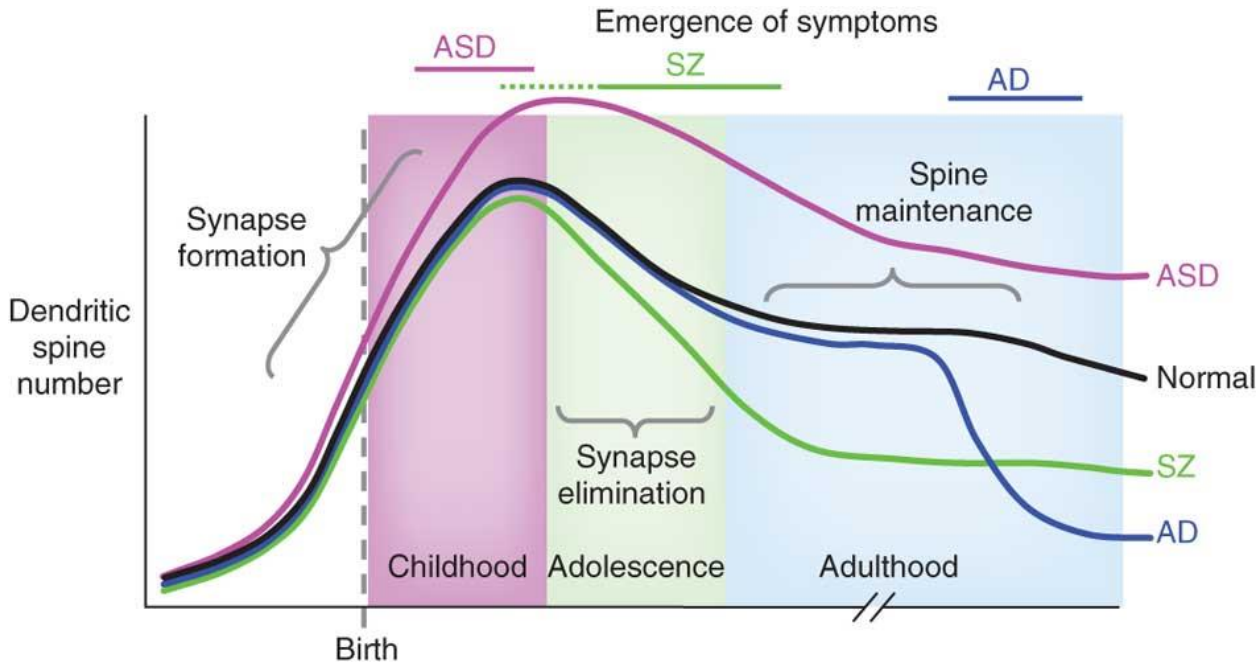

Figure 1.2 Spine Shapes and Densities. A. Top lines indicate the timeframe of symptoms emergence and diagnosis. In normal subjects, spine densities increase before and after birth, and spines are selectively eliminated during childhood and adolescence to adult levels in a process called pruning. In ASD, overabundant spine formation may occur in childhood leading to increased spine densities. In schizophrenia (SZ), overzealous spine pruning during adolescence may lead to the disease onset. (Figure from(Penzes et al. 2011)). Copyright © 2011 Nature Publishing Group used with permission

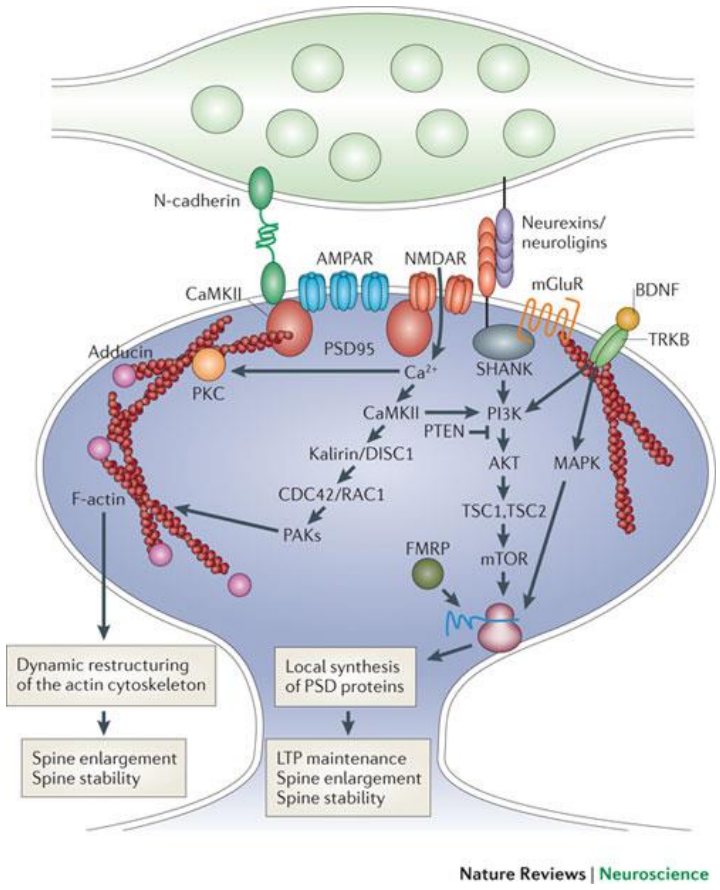

Figure 1.3 Signaling Pathways in the Dendritic Spine. Induction of synaptic plasticity at individual synapses is associated with a rapid enlargement of the spine head, an increase in synaptic efficacy and a switch in the stability of the synapse. Multiple molecules are engaged in this process: protein kinases like CaMKII (calcium/calmodulin protein kinase II)), local protein synthesis (for example of BDNF (brain-derived neurotrophic factor), TRKB (tyrosine kinase B), MAPK (mitogen-activated protein kinase), PI3K, (phosphoinositide 3-kinase), PTEN (phosphatase and tensin homologue), AKT, TSC1 (tuberous sclerosis 1), and FMRP (fragile X mental retardation protein)) contribute to long-term potentiation (LTP) maintenance and spine enlargement. Proteins involved in the regulation of the actin cytoskeleton (F-actin): CDC42 (cell division control protein 42), RAC1 (Ras-related C3 botulinum toxin substrate 1), PAKs (p21-activated kinases)), contribute to LTP maintenance and spine enlargement. Adhesion molecules and molecules of the postsynaptic density (including PSD95 (postsynaptic density protein of 95 kDa), SHANKs (SH3 and multiple ankyrin repeat domains proteins), neuroligins, N-cadherins, AMPA

receptors (AMPARs) and NMDA receptors (NMDARs)) participate in LTP maintenance, spine enlargement and spine stability.(Figure from Caroni et al. 2012) used with permission Copyright © 2012 Nature Publishing Groups.

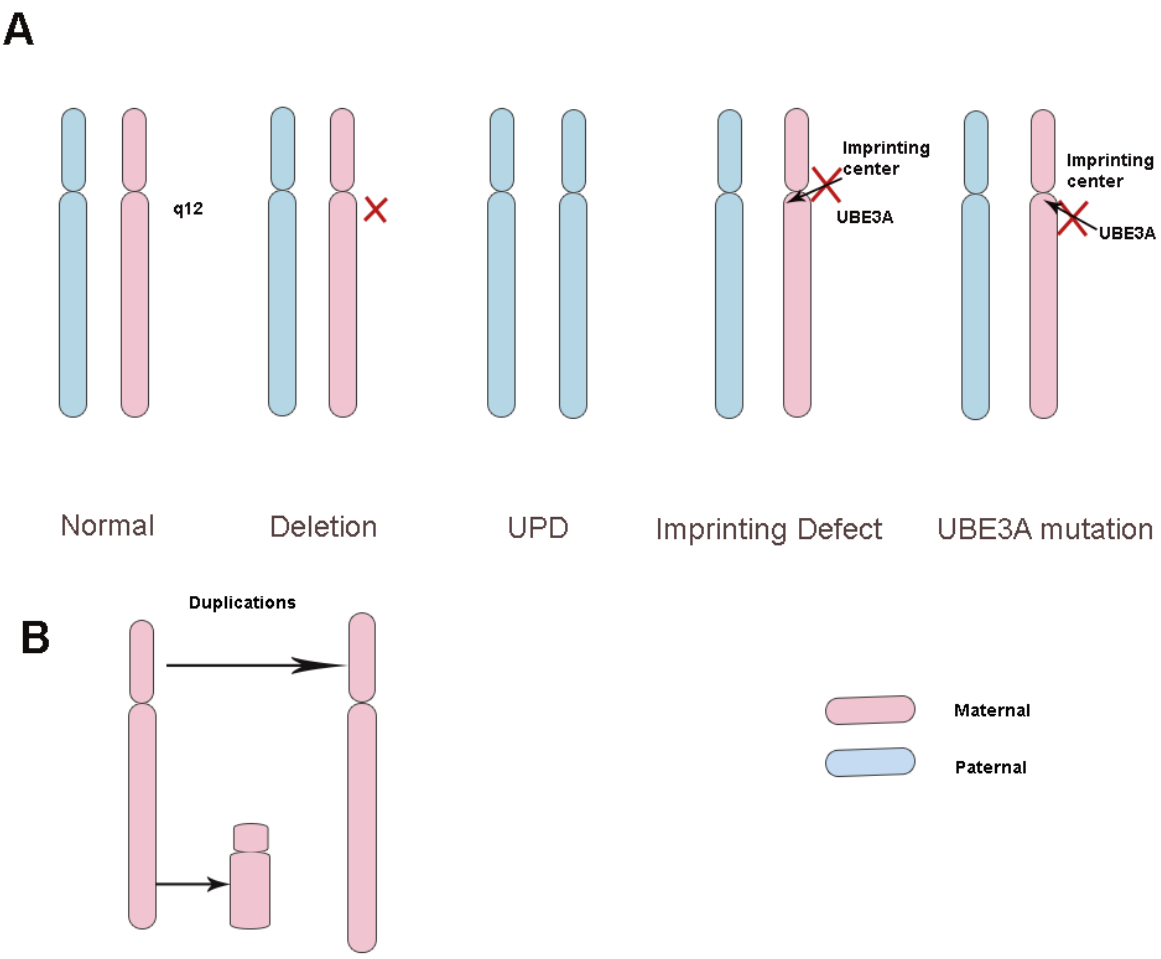

Figure 1.4 AS and Dup15q genetics. A. AS is caused by the functional absence of the maternal copy of 15q11-q13, which happens in the following scenarios: deletion on the maternal chromosome, uniparental disomy (inheritance of two paternal copies), defect in the imprinting region that silences UBE3A transcription and mutations in UBE3A gene itself that render it inactive.

B. Duplication events in 15q11.-12 include interstitial duplications, duplicated regions within chromosome 15, or isodicentric chromosome that comprises from two portions of chromosome 15.

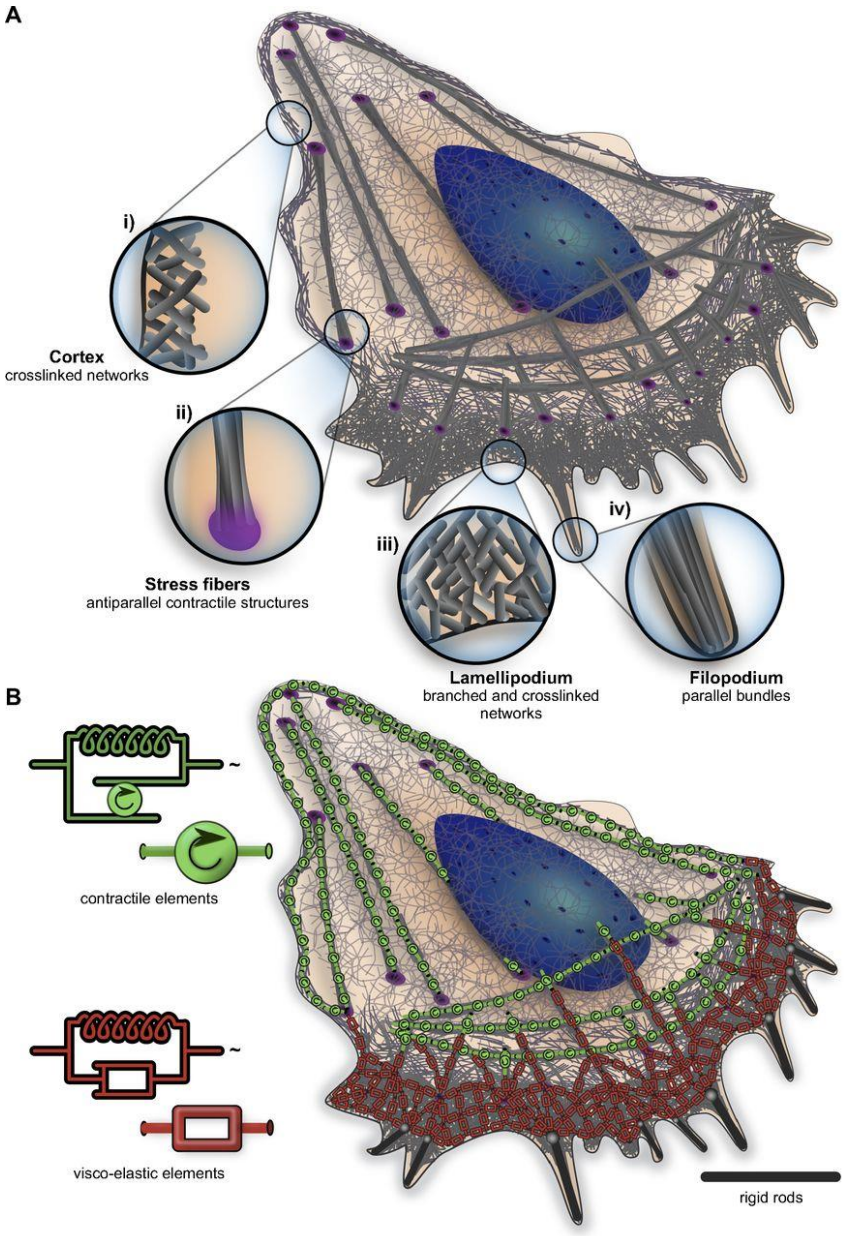

Figure 1.5. **Actin cytoskeleton Motility Models** Diversity of actin architecture and mechanics in the moving cell. A. schematics of the cell with the actin architectures: i) the cell cortex; ii) the stress fiber; iii) the lamellipodium; and iv) filopodia. Zoomed regions highlight specific actin filament arrangements..B. The mechanical profile of the actin architectures in A. The red rectangles are dashpots, viscous components, that represent the actin network, while the green circles are elastic springs due to myosin motor activity. Figure from (Blanchoin et al. 2014) used with permission Copyright © 2014 the American Physiological Society.

Bibliography

Arellano, J.I. et al., 2007. Ultrastructure of dendritic spines: correlation between synaptic and spine morphologies. *Frontiers in neuroscience*, 1(1), pp.131–143.

Blanchoin, L. et al., 2014. Actin dynamics, architecture, and mechanics in cell motility. *Physiol.Rev.*, 94(1), pp.235-63

Borinskaya S., Marchenko O., Loew L.M., 2016. Modeling Actin Dynamics *Encyclopedia of Cell Biology* Vol 4., pp.10-12

Bourgeois, J.P. & Rakic, P., 1993. Changes of synaptic density in the primary visual cortex of the macaque monkey from fetal to adult stage. *J Neurosci*, 13(7), pp.2801–20.

Brown, S.A. et al., 2011. Virtual NEURON: A strategy for merged biochemical and electrophysiological modeling. *Journal of Computational Neuroscience*, 31(2), pp.385–400.

Caroni, P., Donato, F. & Muller, D., 2012. Structural plasticity upon learning: regulation and functions. *Nature Reviews Neuroscience*, 13(7), pp.478–490. Available at: http://dx.doi.org/10.1038/nrn3258.

Chamberlain, S.J. et al., 2010. Induced pluripotent stem cell models of the genomic imprinting disorders Angelman and Prader-Willi syndromes. *Proceedings of the National Academy of Sciences of the United States of America*, 107(41), pp.17668–73. Available at: http://www.ncbi.nlm.nih.gov/pubmed/20876107\nhttp://www.pubmedcentral.nih.gov/articlerender.fcgi?artid=PMC2955112.

Chazeau, A. et al., 2015. Mechanical coupling between transsynaptic N-cadherin adhesions and actin flow stabilizes dendritic spines. *Molecular Biology of the Cell*, 26, pp.859–873. Available at: http://www.molbiolcell.org/cgi/doi/10.1091/mbc.E14-06-1086.

Chazeau, A. et al., 2014. Nanoscale segregation of actin nucleation and elongation factors determines dendritic spine protrusion. *The EMBO journal*, 33(23), pp.1–20. Available at: http://www.ncbi.nlm.nih.gov/pubmed/25293574.

Comery, T. a et al., 1997. Abnormal dendritic spines in fragile X knockout mice: maturation and pruning deficits. *Proceedings of the National Academy of Sciences of the United States of America*, 94(10), pp.5401–5404.

Craig, E.M. et al., 2012. Membrane tension, myosin force, and actin turnover maintain actin treadmill in the nerve growth cone. *Biophysical Journal*, 102(7), pp.1503–1513.

Danuser, G., Allard, J. & Mogilner, A., 2013. Mathematical modeling of eukaryotic cell migration: insights beyond experiments. *Annual review of cell and developmental biology*, 29(July), pp.501–28.

Dindot, S. V. et al., 2008. The Angelman syndrome ubiquitin ligase localizes to the synapse and nucleus, and maternal deficiency results in abnormal dendritic spine morphology. *Human Molecular Genetics*, 17(1), pp.111–118.

Ditlev, J.A. et al., 2009. An open model of actin dendritic nucleation. *Biophysical Journal*, 96(9), pp.3529–3542.

Fiala, J.C. et al., 1998. Synaptogenesis via dendritic filopodia in developing hippocampal area CA1. *J Neurosci*, 18(21), pp.8900–8911.

Harris, K.M., 1999. Structure, development, and plasticity of dendritic spines. *Current Opinion in Neurobiology*, 9(3), pp.343–348.

Hill, T.C. & Zito, K., 2013. LTP-Induced Long-Term Stabilization of Individual Nascent Dendritic Spines. *Journal of Neuroscience*, 33(2), pp.678–686.

Hogart, A. et al., 2010. The comorbidity of autism with the genomic disorders of chromosome 15q11.2-q13. *Neurobiology of Disease*, 38(2), pp.181–191.

Hotulainen, P. & Hoogenraad, C.C., 2010. Actin in dendritic spines: Connecting dynamics to function. *Journal of Cell Biology*, 189(4), pp.619–629.

Ivanov, A. et al., 2009. Drebrin A regulates dendritic spine plasticity and synaptic function in mature cultured hippocampal neurons. *Journal of cell science*, 122(3), pp.524–534.

Kayser, M.S., Nolt, M.J. & Dalva, M.B., 2008. EphB Receptors Couple Dendritic Filopodia Motility to Synapse Formation. *Neuron*, 59(1), pp.56–69.

Korobova, F. & Svitkina, T., 2010. Molecular Architecture of Synaptic Actin Cytoskeleton in Hippocampal Neurons Reveals a Mechanism of Dendritic Spine Morphogenesis. *Molecular Biology of the Cell*, 21, pp.165–176.

Kotaleski, J.H. & Blackwell, K.T., 2010. Modelling the molecular mechanisms of synaptic plasticity using systems biology approaches. *Nature reviews. Neuroscience*, 11(4), pp.239–251.

Lohmann, C. & Bonhoeffer, T., 2008. A role for local calcium signaling in rapid synaptic partner selection by dendritic filopodia. *Neuron*, 59(2), pp.253–260. Available at: http://www.ncbi.nlm.nih.gov/pubmed/18667153.

Mogilner, A. & Rubinstein, B., 2005. The Physics of Filopodial Protrusion. *Biophysical Journal*, 89(2), pp.782–795.

Parent, J.M. & Anderson, S.A., 2015. Reprogramming patient-derived cells to study the epilepsies. *Nature neuroscience*, 18(3), pp.360–6.

Penzes, P. et al., 2011. review Dendritic spine pathology in neuropsychiatric disorders. *Nature Publishing Group*, 14(3), pp.285–293.

Phillips, M. & Pozzo-Miller, L., 2014. Dendritic spine dysgenesis in autism related disorders. *Neuroscience Letters*, 601, pp.30–40.

Pi, H.J. et al., 2010. CaMKII control of spine size and synaptic strength: role of phosphorylation states and nonenzymatic action. *Proceedings of the National Academy of Sciences of the United States of America*, 107(32), pp.14437–42.

Pignatelli, M. et al., 2014. Changes in mGlu5 receptor-dependent synaptic plasticity and coupling to homer proteins in the hippocampus of Ube3A hemizygous mice modeling angelman syndrome. *The Journal of neuroscience : the official journal of the Society for Neuroscience*, 34(13), pp.4558–66.

Purpura, D.P., 1974. Dendritic spine “dysgenesis” and mental retardation. *Science (New York, N.Y.)*, 186(4169), pp.1126–1128.

Rubio, M.D. et al., 2011. Cellular/Molecular Regulation of Synapse Structure and Function by Distinct Myosin II Motors. *Journal of Neuroscience*, 31(4), pp.1448–1460.

Saneyoshi, T., Fortin, D.A. & Soderling, T.R., 2010. Regulation of spine and synapse formation by activity-dependent intracellular signaling pathways. *Current Opinion in Neurobiology*, 20(1), pp.108–115.

Sun, J. et al., 2015. UBE3A Regulates Synaptic Plasticity and Learning and Memory by Controlling SK2 Channel Endocytosis. *Cell reports*, 12(3), pp.449–461. Available at:

Tashiro, A., Minden, A. & Yuste, R., 2000. Regulation of dendritic spine morphology by the Rho family of small GTPases: antagonistic roles of Rac and Rho. *Cerebral Cortex*, 10(10), pp.927–938.

Toro, R. et al., 2010. Key role for gene dosage and synaptic homeostasis in autism spectrum disorders. *Trends in Genetics*, 26(8), pp.363–372.

Vissers, L.E.L.M., Gilissen, C. & Veltman, J.A., 2015. Genetic studies in intellectual disability and related disorders. *Nature Reviews Genetics*, 17(1), pp.9–18.

Weeber, E.J. et al., 2003. Derangements of hippocampal calcium/calmodulin-dependent protein kinase II in a mouse model for Angelman mental retardation syndrome. *The Journal of neuroscience : the official journal of the Society for Neuroscience*, 23(7), pp.2634–2644.

Yang, C. & Svitkina, T., 2011. Filopodia initiation: focus on the Arp2/3 complex and formins. *Cell adhesion & migration*, 5(5), pp.402–408.

Yashiro, K. et al., 2009. Ube3a is required for experience-dependent maturation of the neocortex. *Nature neuroscience*, 12(6), pp.777–83.

Yasuda, S. et al., 2014. Activation of Rheb, but not of mTORC1, impairs spine synapse morphogenesis in tuberous sclerosis complex. *Scientific reports*, 4, p.5155.

Yuste, R. & Denk, W., 1995. Dendritic spines as basic functional units of neuronal integration. *Nature*, 375(6533), pp.682–684.

Ziv, N.E. & Smith, S.J., 1996. Evidence for a role of dendritic filopodia in synaptogenesis and spine formation. *Neuron*, 17(1), pp.91–102.

Chapter 2

A Minimal Actomyosin-based Model Predicts the Dynamics of Filopodia on Neuronal Dendrites[2]

Abstract

Dendritic filopodia are actin-filled dynamic subcellular structures that sprout on neuronal dendrites during neurogenesis. The exploratory motion of the filopodia is crucial for synaptogenesis but the underlying mechanisms are poorly understood. To study the filopodial motility, we collected and analyzed image data on filopodia in cultured rat hippocampal neurons. We hypothesized that mechanical feedback among the actin retrograde flow, myosin activity and substrate adhesion gives rise to various filopodial behaviors. We have formulated a minimal one-dimensional partial differential equation model that reproduced the range of observed motility. To validate our model, we systematically manipulated experimental correlates of parameters in the model: substrate adhesion strength, actin polymerization rate, myosin contractility and the integrity of the putative microtubule-based barrier at the filopodium base. The model predicts the response of the system to each of these experimental perturbations, supporting the hypothesis that our actomyosin-driven mechanism controls dendritic filopodia dynamics.

Introduction

Formation of synapses during development and their maintenance in the adult organism are required for the proper functioning of neuronal circuitry. Spines, micrometer-scale protrusions from neuronal

---

[2] The work presented in this chapter is a manuscript submitted to MBoC. The following authors contributed their work to various sections and review of the manuscript: Olena O. Marchenko[1], Sulagna Das[2], Ji Yu[1] , Igor L. Novak[1], Vladimir I. Rodionov[1], Nadia Efimova[3], Tatyana Svitkina[3], Charles W. Wolgemuth[4] and Leslie M. Loew[1] ·Authors affiliations: [1]R. D. Berlin Center for Cell Analysis and Modeling, University of Connecticut Health Center, Farmington, CT [2]Department of Anatomy and Structural Biology, Albert Einstein College of Medicine, New York, NY, [3] Department of Biology, University of Pennsylvania, Philadelphia, PA, [4] Departments of Physics and Molecular and Cellular Biology University of Arizona Tucson, AZ

dendrites, receive the majority of synaptic inputs in the central nervous system. Regulation of spine density, morphology and spatial distribution is required for synaptic stability and plasticity. Abnormal density and morphology are associated with impaired motor and cognitive functions underlying neurological disorders such as autism, schizophrenia and fragile-X syndrome (Segal, 1995; Irwin *et al.*, 2000; Lin and Koleske, 2010; Wilson *et al.*, 2010).

Spine morphogenesis is a delicate process that starts from the formation of the dendritic filopodium (Ziv and Smith, 1996; Hotulainen and Hoogenraad, 2010; Korobova and Svitkina, 2010). Dendritic filopodia are dynamic protrusions up to 15μm in length that explore their extracellular environment and connect with the presynaptic axons (Kayser *et al.*, 2008) . The population of motile filopodia is highest during early neuron development and gradually decreases as the neuron ages. Starting from the 4th day of *in vitro* (DIV4) hippocampal cell culture, when neurites are fully differentiated into axons and dendrites, filopodia are numerous and highly motile (Ziv and Smith, 1996). They extend 2-10 microns away from the dendritic shaft to establish contact with nearby axons and also can retract back toward the dendrite. The protrusion/retraction cycle repeats until filopodia stabilize or dissolve back into their parent dendrite. By DIV13 most of the filopodia observed in culture are non-motile, whether solitary or connected to an axon. In the same time frame, the first spines start to appear on the dendrites. The initial axon-dendritic contact and its stabilization are considered to be the key events in spinogenesis (Kayser *et al.*, 2008; Hotulainen and Hoogenraad, 2010). However, the dynamics of spine morphogenesis from filopodia has not been fully characterized and the mechanism of dendritic filopodial motility is poorly understood.

What is known is that dendritic filopodial motility is actin-based. The main components of actin network dynamics in motile cells have been extensively studied, resulting in models that describe various mechanisms of leading edge protrusion (Leibler and Huse, 1993; Mogilner and Rubinstein, 2005; Lammermann and Sixt, 2009). From models of keratocyte and nerve growth cone motility we know that actin-based motility arises from the force that polymerizing actin filaments exert on the membrane, which is opposed by membrane tension (Medeiros *et al.*, 2006). Myosin II contracts the actin filaments generating the actin retrograde flow that pulls filaments away from the leading edge (Verkhovsky *et al.*,

1995). If the actin filament polymerization rate overcomes the retrograde flow, a local protrusion forms. How are actin polymerization, contraction and local adhesion mechanisms marshaled to control dendritic filopodial motility and stability? Previous models of filopodial dynamics treat the system as a stiff elastic rod compressed by the membrane resistance force without considering adhesion or contractility (Mogilner and Rubinstein, 2005) ; others have focused on the adhesion to and compliance of the substrate (Chan and Odde, 2008). These earlier studies do not consider the unique molecular composition of dendritic filopodia.

The molecular composition of the actin network in dendritic filopodia, which lack filament bundling proteins found in conventional filopodia (Korobova and Svitkina, 2010), affects the rheological properties making it more viscous compared to bundled actin (Kim *et al.*, 2009). For example, the actin network in dendritic spines is 4-5 times more viscous than the average cell cytoskeleton (Smith *et al.*, 2007). The actin cytoskeleton inside a dendritic filopodium consists of short branched filaments of mixed polarity (Portera-Cailliau *et al.*, 2003; Korobova and Svitkina, 2010), which can make them sensitive to myosin contractile stresses. Adhesion to the substrate can affect actin retrograde flow and govern the retraction phase of the filopodia motility cycle (Yamashiro and Watanabe, 2014). Furthermore, substrate adhesion is required for neurogenesis (Lin and Koleske, 2010) and may be important for dendritic filopodia behavior.

Therefore, we expect the dynamics of dendritic filopodia to differ from that of conventional filopodia. Such a range of behaviors could be involved in the establishment and stabilization of initial synaptic connections in the developing nervous system (Portera-Cailliau *et al.*, 2003). Indeed, in this paper we characterize a wide range of motility states, from non-motile to persistently fluctuating filopodia. To understand these diverse motility behaviors, we develop a minimal mathematical model of dendritic filopodia dynamics that explains the spatiotemporal regulation of actin and myosin dynamics and describes conditions under which dynamic filopodia are maintained. The model employs partial differential equations that balance the forces of substrate adhesion, actin retrograde flow, and myosin contractility, while accounting for actin polymerization and diffusion. To validate the proposed

mechanism experimentally, we perturbed key model parameters using various manipulations, comparing the model predictions with the results of motility analysis of dendritic filopodia on hippocampal neurons in culture.

Results

To collect sufficient data on filopodia dynamics, we performed 2hr (Δt=1s) time-lapse recordings of filopodia extending and retracting from the dendrites of young neurons (DIV4-12) (Figure 1A). Filopodial dynamics were then quantified by tracking filopodia length automatically using our custom-written software FiloTracker (*Movie S1A, Figure 1, B and C*). Having collected trajectories from 938 filopodia (83 neurons), we classified dendritic filopodia by their motility patterns into filopodia with transient and continual dynamics, and non-motile filopodia (*Figure S1 A and C*). Filopodia with continual dynamics displayed lifetimes t>20min with regular protrusion/retraction cycles (*Figure S1A*). Filopodia with transient motility were defined by irregular short-lived bursts of motility (Figure S1B), and filopodia with constant length did not exhibit any motility, displaying invariable length for the duration of the recording session (20min or more) (*Figure S1C*). Filopodia were more motile during early neurodevelopment with a motile fraction of 41%±22 for DIV 3-9 that reduced to 11%±6 after DIV10 (*Figure 1D).* This result is consistent with the earlier reported trend(Smith *et al.*, 2007) .

In all filopodia trajectories with continual dynamics, we calculated the protrusion rates (length increase per time during extension) and retraction rates (length decrease per time during retraction) with the Peakfinder algorithm, which was set to detect large changes in length (see Methods). We determined that the lengths fluctuate with similar protrusion and retraction rates of 0.37±0.080 μm/s and 0.32+0.054μm/s in DIV4-7, respectively.

Formulation of a model based on experimental constraints

We hypothesized that feedback among the actin retrograde flow (ARF), myosin activity and substrate adhesion are the principal factors that drive the range of filopodia behaviors observed in primary neuron culture, and a deterministic mathematical model was developed to quantitatively explore this hypothesis. Since growth and retraction events observed in filopodia are due to stochastic events involving small numbers of molecules and filaments, the protrusion and retraction rates measured from the trajectories are expected to be higher than the rates estimated from a deterministic mathematical

model. This is because the experimental procedure, employing the Peakfinder algorithm, only detects growth or retraction events and does not account for resting phases between events. Thus the reported experimental protrusion and retraction rates will always be much faster than those produced by the deterministic model. Additionally, the experimental measurements of protrusion and retraction rates were necessarily performed on motile filopodia. The deterministic model necessarily corresponds to behavior that is essentially integrated over all filopodia in a given state. However, because the simplicity of the deterministic model allows for ready analysis and exploration of hypotheses, it has real advantages for the purposes of this study. Thus, the deterministic model serves well to explain the overall behavior of the system and any trends or patterns due to experimental manipulations.

We considered a minimal number of biophysical mechanisms as sufficient to describe filopodium dynamics, with its extension driven by actin polymerization and retraction by myosin contraction. The total contractile force exerted within the filopodium is proportional to the total amount of bound myosin. When the filopodium length is short, there is only a small amount of bound myosin, and consequently a small contractile force. Therefore, polymerization of the actin at the tip causes the filopodium to extend. As the filopodium gets longer, the contractile force gets larger due to binding of myosin, and the tip extension slows. At some point, myosin contraction can outstrip polymerization and the filopodium shrinks. As shrinking proceeds, the density of bound myosin increases and accelerates contraction. Ultimately, myosin dissociation reduces the contractile force and the filopodium length reaches its minimum before extension resumes. It is therefore possible that standard actomyosin dynamics can account for all ranges of filopodia dynamics. However, other factors such as the viscoelasticity of the actin network and the adhesion of the filopodium to the substrate may affect the overall system behavior. These and other features of the system can be quantitatively explored with a mathematical model based on five essential processes (Figure 2): a) polymerization of F-actin at the tip of the filopodium; b) binding and unbinding of myosin to F-actin; c) isotropic contractile stresses exerted by myosin on F-actin; d) viscous flow of F-actin (ARF) induced by these contractile stresses; e) friction between the filopodium and the substrate due to adhesion(Kim, 2012).

We implemented the model filopodium as a linear 1D object whose length $L(t)$ varies with time. The state of the system is described by two variables, the distribution of bound myosin, $m_b(x,t)$ and the local velocity of the actin network $v(x,t)$, $x \in [0,L]$, where $x=0$ corresponds to the base of the filopodium and $x=L$ to the tip. Myosin can bind and unbind from the actin cytoskeleton with rate constants k_{on} and k_{off}, respectively. The unbound myosin is assumed to diffuse rapidly on the length scale of the filopodium and, on the timescale of filopodial dynamics, to be in equilibrium with the large reservoir contained in the adjacent dendrite; therefore its concentration, m, is assumed to be constant.

Bound myosin moves with the F-actin at the velocity $v(x)$ and can also diffuse due to random motion of the actin filaments (Kruse *et al.*, 2004). The dynamics of the bound myosin is then described by the following continuity (transport) equation:

$$\frac{\partial m_b}{\partial t} = D\frac{\partial^2 m_b}{\partial x^2} - \frac{\partial}{\partial x}(m_b v) + k_{on}m_0 - k_{off}m_b, \qquad (1)$$

where D is the diffusion coefficient.

The bound myosin exerts a contractile stress on the actin network. We assume that this contractile stress is isotropic and proportional to the concentration of bound myosin. On the timescales relevant to filopodial motility, the actin network can be approximated as a viscous fluid with viscosity η (Bausch *et al.*, 1998). Adhesion between the filopodial membrane and the extra-cellular matrix resists the movement of the filopodium. We account for this as a resistive force proportional to the velocity. Therefore, myosin contractile stresses will induce a viscous flow of F-actin governed by the mechanical balance equation,

$$\zeta v = \eta\frac{\partial^2 v}{\partial x^2} + \sigma_0\frac{\partial m_b}{\partial x}, \qquad (2)$$

which takes into account the three major forces present in the system: viscous stress, the contractile stress exerted by bound myosin, $\sigma_0 m_b$, and the resistive drag force, ζv, due to adhesive interactions with the substrate. In *Eq.2*, σ_0 is a myosin contractility coefficient that should be approximately proportional to the maximum force that can be applied by a single myosin molecule.

Eqs (1, 2) are solved with the following initial conditions:

$$L = 0, \quad m_b(x,0) = 0, \quad v(x,0) = 0, \tag{3}$$

and L, m_b and v allowed to evolve over time and along the one dimensional space. With regard to boundary conditions, we assume that F-actin and its bound myosin do not flow into or out of the dendritic shaft based on previous experimental findings (Tatavarty *et al.*, 2012) and possibly due to a barrier formed by microtubules in the adjacent dendritic shaft (this idea will be further explored below); therefore, the flux of bound myosin is zero at the base:

$$\left(D\frac{\partial m_b}{\partial x} - v m_b\right)\Big|_{x=0} = 0, \tag{4}$$

We use a resistive force proportional to the velocity, βv, to model the stress balance at the base of filopodium:

$$\left(\eta\frac{\partial v}{\partial x} + \sigma_0 m_b\right)\Big|_{x=0} = -\beta v\Big|_{x=0}, \tag{5}$$

At the tip of the filopodium, membrane tension, T, exerts a force proportional to the curvature, κ, onto the actin network:

$$(\eta\frac{\partial v}{\partial x} + \sigma_0 m_b)|_{x=L} = -T\kappa, \tag{6}$$

where, effectively, $T\kappa$ is a single parameter. Using experimental data, we estimate that $T\kappa$ = 2 pN (see below). In addition, we find that the model is insensitive to $T\kappa$ values in the range from 0-2 pN. Therefore, we use this value of 2 pN in all of our calculations to simplify the number of free parameters without affecting the results.

The rate that the length of the filopodium changes is equal to the difference between the actin polymerization rate at the tip, v_p, which is set to be independent of other system variables, and the retrograde velocity of the F-actin network. Thus,

$$\frac{dL}{dt} = v_p + v(L,t)\ ; \tag{7}$$

Since the actin at the tip is newly polymerized, myosin will not have bound yet, leading to the boundary condition $m_b(L,t) = 0$. Model variables and parameters are listed in *Table S1*.

The model can recapitulate the experimentally observed motility behaviors

We analyzed equations (1-7) over a large range of parameters using a semi-implicit Crank-Nicolson scheme coded in MATLAB. We found that the model leads to three qualitatively different patterns of behavior: continuous increase of filopodium length, an equilibrium state with constant length, and periodic filopodium length fluctuations around a constant value. To begin, we focused on scenarios where the filopodium length fluctuated, similar to what has been observed during early neuron development (Ziv and Smith, 1996). To test the predictions of our model, we compared the model results to existing experimental measurements of actin retrograde flow (ARF) and myosin localization from live dendritic filopodia (Tatavarty *et al.*, 2012) . In these experiments, ARF was measured and averaged in motile and non-motile filopodia. We compared simulated ARF over protrusion and retraction phases and found striking agreement between the experiment and the model over a wide range of parameter values (Figure 3A). Experimental data and calculations were used to set the parameters: σ_0, v_p, k_{on}, and k_{off}, ζ, η and $T\kappa$ as described in the section below.

Parameter Justification for the Dendritic Filopodia Model

Our actomyosin model for dendritic filopodia has the following 11 parameters: η- actin viscosity, ζ- substrate drag coefficient, σ_0- myosin contractility, m_0- unbound myosin concentration, v_p- polymerization velocity of actin at the tip of the filopodium, T- membrane tension, κ- curvature of the membrane at the tip of the filopodium, β- drag coefficient at base of spine, D- bound myosin effective diffusion coefficient, k_{on}- myosin on rate, k_{off}- myosin off rate.

Of these parameters, T and κ are not independent, as it is possible to re-write the dynamic equations such that only the combination $T\kappa$ appears in the dynamic equations. Therefore, there are 10 parameters that determine the behavior of the model. The definitions, nominal values and units for each parameter are provided in Table S1 in the Supplemental Material. In what follows, we use experimental data from the literature to justify each of these parameters.

A. **Actin viscosity, η.** A number of experiments have probed the viscosity of actin networks in cells. This literature suggests a wide range of values for the cytoskeletal viscosity. For example, Kole, et al. performed passive microrheology on quiescent and motile Swiss 3T3 cells(Kole *et al.*, 2005). In motile cells, they measured the actin viscosity to be about 5 Pa s, whereas Bausch, et al. found a value of 2000 Pa s using magnetic bead microrheology(Bausch *et al.*, 1998). The model produces more accurate agreement with the experimental data for values of the viscosity that are closer to the larger value found by Bausch, et al. We used a value of 500 Pa s, as a baseline value. This viscosity, though, represents the three-dimensional viscosity of the actin network. Because our model is one-dimensional, we need to treat the net effect of the viscosity over the cross-section of the filopodium; i.e., the 1D viscosity is equal to 3D viscosity times the cross-sectional area of the filopodium. If the diameter of a dendritic filopodium is ~ 500 nm, then the cross-sectional area is ~ 0.2 μm^2 and our baseline value of the 1D viscosity is η = 100 pN s.

B. **Substrate drag coefficient, ζ.** To our knowledge, there have not been any experiments that have examined the substrate drag coefficient for dendritic filopodia. However, Chan and Odde simultaneously measured the traction force generated by axonal filopodia and the retrograde flow of actin (Chan and Odde, 2008). They found traction forces of 10-50 pN with actin retrograde flow rates of 80-100 nm/s. The ratio of the traction force to the retrograde flow rate should be approximately equal to the drag coefficient times the length of the filopodium. For an axonal filopodium of length 5 μm, we estimate ζ ~ 100 pN s/μm^2.

C. **The free concentration of myosin, m_0.** We estimate the concentration of unbound myosin molecules to be 0.5 – 5 μM (Wu and Pollard, 2005). In the 1D model, the myosin concentration m_0 is the number of molecules per length, which is then between 6 – 60 molecules/μm.

D. The stress from bound myosin, σ_0. In the 1D model, the combination $\sigma_0 m$ represents the net contractile force, F, that would be produced by a concentration m of myosin molecules distributed over the length L of the filopodium. Therefore, we estimate the total number of bound myosin molecules along the filopodium to be $N \sim mL$. Since the force from a single myosin molecule is ~ 2-3 pN (Norstrom *et al.*, 2010), the net force is $F \sim N$ (2-3 pN) ~ $\sigma_0 m$, or $\sigma_0 \sim L$ (2-3 pN). For a characteristic filopodium length of 2-3 μm, we then estimate σ_0 to be approximately 4 – 9 pN μm. To account for some cooperative effect between myosin molecules, we use a baseline value of 25 pN μm.

E. **Polymerization velocity, v_p.** In vitro, actin filaments elongate at approximately 0.1 μm/s (Kuhn and Pollard, 2005). These experiments were performed at an actin concentration of 1.5 μM, whereas concentrations of G-actin in the lamellipodia of motile cells can be as high as 150 μM(Koestler *et al.*, 2009). In principle, then, actin polymerization in vivo could occur up to 100-fold faster than in these in vitro experiments. However, we expect the velocity at which actin elongates at the tip of the filopodium to be comparable to these values and set a baseline value v_p = 0.9 μm/s.

F. **Membrane tension times curvature, $T\kappa$.** The quantity $T\kappa$ represents the stress that is exerted onto the actin cytoskeleton due to the membrane tension at the tip of the filopodium. Membrane tension in neuronal growSth cones was measured to be about 3 pN/μm (Hochmuth, 1996). The membrane curvature at the tip of the filopod is $\kappa = 4\ \mu m^{-1}$, for a filopodium with a diameter of 500 nm. Therefore, $T\kappa \sim 12\ pN/\mu m^2$. For the 1D model, we need to compute the net force that is exerted on the actin at the filopod tip due to the membrane tension and curvature. (Note that the tension in the membrane along the sides of the filopodium do not contribute any force in the 1D model, as tension on one side of the filopodium cancels the tension on the other side.) Therefore, the force at the tip of the filament is equal to $T\kappa$ times the cross-sectional area of the filopodium, which is then equal to 2.4 pN.

G. **Drag coefficient at the base of the filopodium, β.** We hypothesize that flow of actin out of the base of the filopodium is hindered, most likely due to steric interactions with microtubules in the dendritic shaft. We model this behavior using a resistive drag force that is proportional to the flow rate of actin(*Eq.5)*. To our knowledge, there is no data that will allow us to estimate a value for the constant of proportionality between the drag force and the flow rate. However, as demonstrated in Figure S2B, the system behavior is completely insensitive to β values over 100 and still displays robust oscillations with β = 0. We chose a value large enough to be well within the insensitive region of parameter space so that the actomyosin dynamics slows completely as it approaches the base of the filopodium.

H. **Myosin diffusion coefficient, *D*.** The diffusion coefficient *D* represents the diffusion of bound myosin on the actin. This represents random events, such as slipping of the myosin molecules and diffusion of the actin filaments. The diffusion coefficient for myosin light chain kinase moving on actin filaments was recently measured to be between 0.03 – 0.07 $\mu m^2/s$ (Hong *et al.*, 2015). We use a value of $D = 0.04\ \mu m^2/s$.

I. **Myosin on and off rates, k_{on} and k_{off}.** Nagy, et al. measured the dissociation rate constant for single myosin molecules to be ~ 0.4 s^{-1}. (Nagy A. et al., 2013, Norstrom, et al. 2010) measured the on-rate and off-rate of non-muscle myosin and found them to be comparable (Norstrom *et al.*, 2010). Based on this data, we set baseline values of $k_{off} = 0.13\ s^{-1}$ and $k_{on} = 0.12\ s^{-1}$.

Myosin activity is the main regulator of actin retrograde flow force. In the model, bound myosin is pushed by actin retrograde flow towards the dendrite, and accumulation of myosin at the base is largely due to the resistive barrier at the filopodium base, which prevents actin from flowing out of the filopodium (*Eqs.4 and 5*). Because of the barrier at the dendrite, the bound myosin remains highly localized at the filopodium base during all phases of the motility cycle. The output of the simulated motility cycle is shown in Figure 3B1. During the initial stage of protrusion, myosin begins to bind to the actin network which leads to generation of slow ARF and further promotes accumulation of myosin at the

base of the filopodium (Figure 3B2). When the protrusion rate reaches zero at the peak of the growth phase, bound myosin localizes in high concentration right near the filopodium base, while low concentrations are distributed along the filopodium length decaying to 0 at the tip. During the retraction phase the ARF is larger than during protrusion maintaining high concentrations of myosin at the filopodium base (Figure 3B3). While the deterministic nature of the model does not capture stochasticity present in the live filopodia movement, it does produce representative behavior between the extremes observed experimentally (Figure 3B4 and 5).

Thus, our model emphasizes that maintaining myosin localization at the base is required for persistent filopodial dynamics. To validate the model's prediction, we compared the simulated myosin gradient with the experimental results in the active myosin distribution in live filopodia. Neurons were transfected with Eos-MLC (myosin light chain) DNA construct (Tatavarty *et al.*, 2012). Single-molecule PALM imaging showed localization of active myosin II near the base of the dendritic filopodia (Figure 4A). The probability of myosin light chain (MLC) residence at the base changed from almost 80% at DIV8-10 to 50% at DIV14-15 (Figure 4B). Myosin localization was measured in dynamic and non-motile filopodia with both measurements showing maximum myosin concentration at the base (Figure 4B). The averaged myosin distribution over the course of simulation (Figure 4C) displays a base localization pattern similar to the one from the experimental results.

While the filopodium is filled with branched filamentous actin, the dendrite contains a prominent microtubule network, as shown by electron microscopy images (Figure 5A). The dense network of microtubules runs uninterrupted in the dendrites orthogonal to the filopodial actin filaments forming a barrier. We hypothesize that the microtubules at the base of the filopodium function as a barrier to retain bound myosin and actin inside the filopodium (Figure 5B), as expressed in the boundary condition of our model (*Eq. 4,5).* The no-flux condition for the actomyosin network at the filopodium base (*Eq. 4*) prevents filopodium collapse at the end of the retraction cycle, and is required for filopodium stability. By Newton's law, the microtubule network has to exert some stress on the actin network proportional to the retrograde flow generated in the filopodium. However, it is unclear, if the stress from the microtubule

network in the dendritic shaft plays any role in filopodia motility. Thus, to test the effect of the resistance force at the filopodium base we varied the resistance parameter β and observed its effect on filopodia dynamics. While all values of β resulted in motile filopodium with regular length oscillations (Figure 5Ci and S2B), removing the stress at the base by setting $\beta = 0$ produced shorter filopodia (Figure 5Cii). Therefore, large β values increase filopodial lengths and increase the range of other unconstrained parameters that result in oscillations (Supplemental materials, Figure S2B). Furthermore, treating the filopodia with low doses of nocodazole, a microtubule dissolving drug, abolished filopodia motility and significantly reduced their number (Supplemental materials, Figure S3). In conclusion, our data and model are consistent with the hypothesis that the force at the base of the filopodium, proportional to the actin retrograde flow in the filopodium, stabilizes filopodial length and promotes filopodial motility.

In summary, simulated actin retrograde flow and myosin dynamics recapitulated dynamic behavior of dendritic filopodia observed in live imaging experiments. We next explored whether the model can reproduce the effects of experimental manipulations. We have chosen a series of experimental manipulations that have direct correlates to the key parameters of the model.

Actin polymerization rate regulates filopodia motility.

Cytochalasin D (CD) is a pharmacological agent that disrupts actin polymerization by blocking G-actin incorporation into existing filaments. To understand the effect of polymerization rate on filopodia motility, we designed experiments to systematically decrease the actin polymerization rate with CD. We then compared these experimental results with results from our simulations where we decreased the polymerization rate v_p.

The application of 20 nM CD abolished filopodia motility at DIV9 (Movie S2A). Treatment of neurons with lower concentrations of CD resulted in dose-dependent attenuation of filopodia motility (Movie S2B). While 20nM cytochalasin D treatment “froze” all motile filopodia, a 5nM dose of CD resulted in a 20% reduction in the number of motile filopodia compared to control. (Figure 6A). Smaller concentrations of cytochalasin D (<5nM) did not produce statistically significant effects on the motility of

dendritic filopodia at DIV4-7. The low dose and short time over which cells were exposed to CD assured that the actin cytoskeleton remained intact during our measurements (Figure S4).

Since cytochalasin blocks incorporation of actin monomers into F-actin, the overall motility inhibiting effect of cytochalasin is not surprising (Figure 6A). However, we specifically expected, that the decrease in protrusion rate is reproduced in the model simulations by perturbing polymerization rate v_p. A step-wise reduction of the parameter v_p from 0.9 to 0.1 resulted in essentially non-motile filopodia with the steady-state lengths four-fold smaller than the average lengths of filopodia at v_p=0.9 (Figure 6B). The Experimental data showed a gradual decrease of protrusion rates in dendritic filopodia treated with increasing CD doses (Figure 6C). The trend we observed is reproduced by our mathematical model (Figure 6D).

The effect of substrate adhesion on filopodia dynamics is biphasic.

The drag force, generated by substrate adhesion, inhibits actin retrograde flow and supports polymerizing actin filaments in an elongating filopodium (San Miguel-Ruiz and Letourneau, 2014). Poly-L-lysine is a positively charged polymer that effectively mediates adhesion in cultured neurons. PLL stimulates integrin-substrate binding via syndecans (Beauvais and Rapraeger, 2003), and a range of pLL concentrations is used to obtain viable neurons in culture.

We plated hippocampal neurons on glass coverslip dishes coated with pLL concentrations of 0.01, 0.05, 0.5 1.0, or 10 mg/ml and measured filopodial density, and protrusion and retraction rates using our custom written tracking method described in Figure 1. The highest number of motile filopodia was measured at conc. 0.05mg/ml (Figure 7A), with significantly smaller values at conc. 0.01mg/ml and 1.0 mg/ml (Movies S3A-C*)*. Because protrusion and retraction rates were the same for the filopodia grown on corresponding pLL substrate, all rates were compared together (Figure 7B). Motile filopodia grown on pLL applied at conc. 0.05mg/ml had the highest protrusion and retraction rates of 0.37±0.080 μm/s and

0.32+0.054μm/s respectively, while filopodia grown at the other concentrations showed a significant reduction in protrusion and retraction rates (Figure 7B).

To examine whether these results correlate qualitatively with the modeling results, we simulated filopodia dynamics over a range of the drag force parameters ζ. A greater traction force with increasing drag force parameter resulted in changes in actin retrograde flow across the adhesion drag force range. As a result of this, the simulated protrusion and retraction rates in filopodia followed a biphasic trend corresponding to the net sum of forces

At ζ values below 20, the force due to friction was insufficient to generate motility and resulted in non-motile short filopodia, consistent with observations on live filopodia grown on low pLL concentrations. The protrusion and retraction rates were decreased compared to nominal case (This phenotype can be explained by lack of traction force and inability to generate sufficient actin retrograde flow necessary for retraction. Similarly, filopodia plated on poly-L-lysine taken at low concentrations were not able to undergo regular motility cycles and flailed during protrusion and retraction.

Filopodial protrusion rates decreased at ζ >110, and no regular motility was observed (Figure 7Ci). Interestingly, the retraction rates were greater compared to protrusion rates (Figure 7Cii). At larger values of the drag coefficient, friction forces counteract actin retrograde flow, and the resulting protrusion rate is small and insufficient to maintain retraction phase which halts motile cycle. This result is congruent with the observation that filopodia grown on poly-L-lysine taken at high concentrations were straight and immobile.

Since the effect of drag force coefficient on the filopodial motility is quite dramatic, we expected that filopodial lengths would also be affected by the changes in substrate adhesion. Indeed, when comparing experimental measurements between the lowest and highest PLL concentrations, filopodial lengths increased almost twice (Figure 7Di).

The increasing length trend was reproduced in simulations across the range drag force parameter ζ [20:120]. At ζ >100, the steady-state length of non-motile filopodia was greater than the average lengths of motile filopodia at lower values of ζ (Figure 7Dii).

Thus, in simulated filopodia as well as in live neurons, intermediate values of adhesion drug coefficient produced filopodia with the greatest protrusion/retraction rates undergoing regular cycles of protrusion and retraction.

Dendritic Filopodia Lengths and Motility are Increased by Blebbistatin Treatment

Experimentally, it has been shown that non-muscle myosin is a key regulating force in filopodia dynamics, and myosin inactivation by pharmacological agents, such as blebbistatin, abolishes filopodia motility (Medeiros *et al.*, 2006; Ryu *et al.*, 2006). The force opposing protrusion is generated by myosin contractile activity on the actin network and it affects both protrusion and retraction rates of the motile system. To evaluate how the myosin-actin interaction proposed in the model predicts and explains the live filopodia motility, we treated dendritic filopodia with a range of blebbistatin concentrations. To minimize the cytotoxicity and nonspecific effects of blebbistatin (Kepiro *et al.*), we limited the upper concentration to 2.5µM (Movie S4); at 10µM or higher, we observed collapse of filopodia and membrane blebbing.

The result of gradual myosin inactivation on filopodia dynamics was best captured by comparing filopodial lengths (*Figure 8A,B*) and retraction/protrusion rate patterns (*Figure 8C,D,E,F*) in the experiments and simulations. This is because the protrusion/retraction rates, and length measurements (as opposed to the fraction of motile filopodia) are most directly compared to the output of our deterministic partial differential equations simulations. In the experiment, the filopodia were significantly longer in cells treated with 2.5µM blebbistatin, when compared to control (*Figure 8A*). This is expected as the balance between the fixed actin polymerization rate and the decreasing myosin induced contractility moves the system toward increased average filopodial length. Likewise, blebbistatin increases the measured (*Figure 8D*) protrusion rate. Surprisingly, however, blebbistatin also increases the measured average contraction rate (*Figure 8C*). To explain the observed trends in filopodial motility rates and

lengths in terms of the drug effect on myosin activity, we looked at how simulated filopodia dynamics change when the myosin on-rate parameter, *kon*m0*, is decreased.

Blebbistatin binds to myosin in the ADP-Pi state and interferes with the phosphate release process, locking myosin in the actin-unbound state (Kovacs *et al.*, 2004). Thus, the effect of blebbistatin can be modeled as a decreased *m0* in *Eq. 1*, which effectively decreases the on-rate for formation of bound myosin, or, equivalently, increases the effective dissociation constant, Kd. In simulations, instantaneous protrusion rate was calculated at the half point between minimum and maximum lengths in the oscillation, and instantaneous retraction rate was calculated at the half point between the maximum and minimum lengths of the oscillation. In simulated filopodia dynamics, lower myosin on-rate resulted in longer filopodia compared to the control on-rate (*Figure8B*). Satisfyingly consistent with the experiments, the protrusion and retraction rates in these filopodia were both increased as the Kd parameter increased. The time it took for the myosin to accumulate at sufficient amounts to induce retraction increases with increase in Kd; however because of the increased duration of the protrusion phase, there is actually sufficient time for a significantly increased level of bound myosin at the peak of an oscillation, resulting in a faster retraction phase. In other words, the longer duration of the growth phase as well as the longer length of the filopodia allow more myosin to accumulate despite the higher Kd, resulting in faster retraction (*Figure 8E*). Of course, if we were to decrease Kd for myosin binding still further, the system would stop oscillating and protrusion would proceed unchecked (not shown). Thus, the simulation and experimental results are consistent, giving us confidence that our conceptually simple model is sufficient to explain the dynamic behavior of dendritic filopodia.

Discussion

In this study, we numerically simulated and experimentally characterized two types of dendritic filopodia, non-motile and fluctuating. We demonstrated that a complex interplay among the actin retrograde flow, myosin contractility and substrate adhesion regulate filopodia dynamics observed in primary neuron culture. Consequently, we formulated a simple mechanism that explains filopodia transition from motile to immotile state. Understanding filopodia dynamics is a necessary step for developing insight into the dendritic spine plasticity and stability. Analyzing the filopodia motility in high-resolution is of great utility for identification of cellular phenotypes in neurodevelopmental disorders and development of drug-screening platforms.

We found that filopodia protrusion rate is highly sensitive to actin polymerization. Cytochalasin inhibits polymerization by blocking free barbed ends resulting in reduced filopodia protrusion rate. Similarly, in neuronal growth cones, 5μM cytochalasin B (CB) treatment resulted in reversibly blocked motility (Medeiros *et al.*, 2006). Treatment with CD also decreases membrane tension by as much as ~50% (Lieber *et al.*, 2013). We define membrane protrusion kinematically using the parameter v_p, which implicitly contains the effects of membrane tension at the tip. Because the actin-generated protrusive force depends on the number of pushing actin filaments, more filaments with generate higher membrane tension values, whereas fewer filaments will yield lower membrane tension values (Lieber *et al.*, 2013).

The drug produced a dose-dependent reduction in filopodia protrusion and retraction rates, and steady state filopodia length. Thus, actin polymerization rate at the filopodium tip is one of the key parameters that determines the filopodia dynamics and lifetime. Continuous depolymerization rate has been reported at the dendritic filopodia base, where accumulation of myosin takes place, and it is significantly smaller than the polymerization rate (Tatavarty *et al.*, 2012). While we did not explicitly include depolymerization rate in the model, we assumed that the v_p parameter at the filopodia tip is a net actin polymerization rate and combines the polymerization and depolymerization rates. Because only the polymerization rate at the leading edge is inhibited by CD, the depolymerization rate is not affected and

contributes to the filopodia retraction rate. Therefore, the model can reproduce the experimental results well with the simplifying assumptions about the rates.

Next, we showed that traction force due to substrate adhesion promotes filopodia motility on surfaces with intermediate adhesiveness. Filopodia protrusion/retraction rates and motile fraction exhibited a biphasic dependence on adhesion strength, with filopodia at intermediate adhesion strength displaying the highest motility rates. The results of simulations also suggested that protrusion and retraction rates in dendritic filopodia are highly sensitive to the strength of substrate adhesion. At low and high values of the adhesion coefficient the actin retrograde flow was weaker producing stable or slightly motile filopodia. The highest simulated motility rates were observed at intermediate values of traction force. These results are consistent with the trend in actin retrograde flow measurements on various adhesion strengths in axonal growth cones (Geraldo and Gordon-Weeks, 2009). Similarly, actomyosin-based keratocyte motility on fibronectin, also shows a biphasic distribution of locomotion speed on substrates of increasing adhesion (Barnhart *et al.*, 2011). However, while the biphasic trend is reproduced by the model, the exact relationship between PLL concentration and adhesion coefficient value is not known.

Interestingly, the data suggests that the filopodia lengths are slightly greater at the high concentrations of PLL in the substrate. This effect can be due to the fact that while the retraction and protrusion rates are slower, the force required to overcome the friction of the substrate increases with the stickiness of the substrate, and thus the minimal length that filopodium can reach at the end of retraction phase increases, which consequently leads to longer filopodia on average.

The treatment of adhesion in our model assumes that the traction force arises from uniform adhesion between the filopodium and the substrate. The assumption can be applied only in case of very soft or very stiff surfaces (Bangasser et al., Biophys J, 2013), and a more elaborate description of the interaction between the substrate and filopodial membrane will yield more accurate results for all surface types. A stochastic physical model is needed to model motor-clutch interaction of myosin-substrate linkage, where tension along the engaged clutches sums to a traction force balanced by the tension and deformation of

the compliant substrate (Chan and Odde et al., 2008). However, in vivo substrates such as glial cells, neurons and laminin are very soft (0.04-0.3kPa) , while the experimental system uses thin PLL on glass surface and is considered a stiff substrate (Engler, 2003). Thus, a basic description of traction forces is relevant and recapitulates qualitatively the biphasic trend observed in the experiments. Nevertheless, measurements on the PLL substrate stiffness have not been done for the experimental system used and are necessary in deciding which model is more appropriate.

The next important parameter of filopodia dynamics is the effect of myosin activity. Experimentally, we show that bound myosin accumulates at the base *(Figure 4A-B),* and also consistent with the model simulations where bound myosin is highly biased toward the filopodium base during oscillatory dynamics *(Figure4C)*. This pattern reflects the fact that the actin filaments at the base region are the oldest and therefore have the most time to bind myosin. The myosin localization pattern maintains the actin retrograde flow, which in turn causes cyclic length contractions in filopodia.

To further explore the role of myosin for filopodium motility, we disrupted myosin binding to actin with low doses of blebbistatin (Loudon *et al.,* 2006). Treatments with a range of increasing blebbistatin concentrations led to dendritic filopodia with increased protrusion rates (Figure 8D), which is expected because protrusion is a competition between actin polymerization at the tip and actomyosin-dependent contraction. Similarly, the average length of filopodia also increases with increased blebbistatin concentration *(Figure 8A).* Both of these responses to inhibition of myosin binding are recapitulated by the model (*Figure 8F* and *8B*, respectively). However, unexpectedly and remarkably, retraction rates also increased with low doses of blebbistatin *(Figure 8C).* While this result seems counterintuitive, it is predicted by the model *(Figure 8E).* In addition, analysis of the model suggests a reason for this unexpected behavior: the longer duration of the fluctuations required to reach the maximum length when myosin binding is inhibited also gives the myosin more time to accumulate in the region of the filopodium base. Another way of thinking about this is to consider the oscillations as arising from a kinetic overshoot in the approach toward balance between actin polymerization and contractility; the overshoot is more severe when myosin binding is inhibited.

It is important to consider potential off-target effects of blebbistatin. While it has been reported previously that myosin inhibition with blebbistatin decreases myosin dependent F-actin disassembly and thus inhibits overall actin turnover rate (Ryu *et al.*, 2006), it was also suggested that blebbistatin decreases actin polymerization rate as an off-target effect, which can cause the decreased motility in filopodia (Tatavarty *et al.*, 2012). The findings also describe non-specific effects by blebbistatin in *Dictyostelium* myosin II-knockout cells(Kolega, 2006) . Indeed, we were unable to use blebbistatin concentrations in excess of 10μM in our experiments, as these concentrations caused complete loss of filopodia and even shrinkage of dendrites. To avoid any of these non-specific effects we limited our measurements to concentrations of 2.5μM and below. Therefore, we believe that effect of blebbistatin on myosin contractility in filopodia was highly specific.

Membrane tension has been shown to play a role in regulating cell motility in rapidly moving keratocytes (Lieber *et al.*, 2013). For thin projections like filopodia, the tension force is set by the force required to pull out a membrane tether, which depends on the membrane surface tension and the bending rigidity of the membrane(Sheetz, 2001). The force from membrane tension is proportional to the curvature of the membrane. Therefore, this force can vary spatially across the membrane. Since this is a one dimensional model that does not account for radial forces within the filopodium, the tension is necessarily 0 everywhere but at the tip.

To summarize, our model reproduces experimental actin flow patterns, as well as the effects of varying myosin, adhesion and actin polymerization that lead to emergence of dynamic filopodia through the following mechanism. Consider a filopodium with a stable steady state length (*Figure 9A*). In this scenario, the actin retrograde flow due to contraction and tension balance the polymerization rate. But this balance can only be attained if the myosin can enter and bind to the filopodial actin at a rate sufficient to keep up with the polymerization rate. Now consider a scenario where myosin binding and unbinding are slow compared to polymerization (*Figure9B*). If the polymerization velocity is fast compared with the on rate of the myosin, then the filopodium will grow to be longer than the balance point that would have been achieved if myosin were fully bound to actin. As time progresses, though, the myosin will bind to a

point where contractile velocity is equal to polymerization velocity. However, the delay caused by the slow myosin unbinding rate is such that the myosin continues to bind, leading to "overshoot" and producing a contractile stress that overcomes the polymerization velocity (*Figure9B*). At this point, the filopodium will start to contract. As the filopodium contracts, myosin continues to bind, which causes the contractile velocity to increase. In addition, as the filopodium shortens, there is less external drag (because the total external drag is proportional to the length of the filopodium). Therefore, the contraction accelerates even further. In the absence of any other effects, the filopodium can end up shrinking to zero size. However, the viscosity of the actin prevents the filopodium from shrinking too quickly and this effect increases as the filopodium gets smaller. Therefore, the actin viscosity can prevent total collapse of the filopodium. Once the unbinding of myosin finally reduces contractility enough for polymerization to once again dominate, the filopodium begins to grow again and the cycle repeats.

Whether filopodial dynamics and stability are important for spine formation is controversial (Portera-Cailliau *et al.*, 2003; Hotulainen and Hoogenraad, 2010). Because the actin network inside the dendritic spine consists mainly of the same components as filopodia, we suggest that the factors that play important role in filopodia stability will be also important in spine morphogenesis and stability. Thus, in future studies we plan to focus on three central aspects of spine morphogenesis: metamorphosis of filopodia into spines, diversity of spine shapes and their stability.

Materials and Methods

Cell culture

Hippocampal neuron cultures were prepared from E18 rat (Sprague–Dawley) hippocampi obtained from BrainBits, Springfield, IL and plated following BrainBits Kit Protocol http://www.brainbitsllc.com/brainbits-kits-primary-neuron-protocol/. Briefly, cells were plated at 20-30,000 cells/well on MatTek (MatTek Corporation, Ashland, MA) glass bottom culture dishes that were thoroughly cleaned by sonicating sequentially in 10% HCl, 20% NaOH and Millipore water or in plasma cleaner and coated with poly-L-lysine (Sigma-Aldrich, St. Louis, MO) overnight before use. Cell cultures were maintained for up to 25 DIV in neurobasal medium supplemented with B27.Samples were imaged with Nikon Plan NA1.25x100 objective on DIV 3-12 on Nikon diaphot 300 inverted microscope. Images were collected with back- illuminated CCD camera (CH350, Roper Scientific) driven by Metamorph image acquisition and analysis software (Metamorph, Sunnyvale, CA).

Drug treatments

For control conditions DMSO was added to Hibernate E, mixed well and the culture media was replaced with the DMSO solution at RT. The cells were imaged immediately following the media replacement for 20min. Blebbistatin(Sigma-Aldrich, St. Louis, MO) was used at 1.0, 2.5, 5.0, 12.5, 25, 50 μM final concentration in DMSO (2.5%) and Cytochalasin D (Sigma-Aldrich, St. Louis, MO) was used at 5.0, 10, 20 nM in DMSO (2%) final concentration at RT. At the start of the recording cell medium was replaced with the well-mixed solution of drug dissolved in DMSO and Hibernate E. The filopodia motility was recorded for 20 minutes after drug administration.

Eos-MLC imaging

To express Eos-MLC fusion, a Gateway cassette (Invitrogen) was inserted to the C-terminal of the tdEos sequence (a gift from J.Wiedenmann, University of Ulm), which converted the original vector into a Gateway vector. An entry clone of the myosin regulatory light chain, Mlrc2, was purchased from Open Biosystems (Thermo Biosystems, Huntsville, AL). The Mlrc2 sequence was then subcloned into the

tdEos

Gateway vector using the LR clonase (Invitrogen) following the manufacturer's procedure to produce the Eos-MLC fusion construct.

Single molecule imaging of Eos-MLC was performed using a modified epifluorescence microscope (Olympus IX81; Olympus, Tokyo, Japan) equipped with 60× microscope objective (numerical aperture, 1.45; Olympus) and a thermoelectric-cooled, electron-multiplying charge-coupled device camera (PhotonMax; Roper Scientific, Trenton, NJ). A 405-nm diode laser (Cube laser system; Coherent, Santa Clara, CA) was the light source for photoactivation. The MLC-green fluorescence of unactivated Eos was excited with the 488-nm laser line from an argon ion laser (CVI Melles Griot, Albuquerque, NM). Activated single molecules were imaged with a 532-nm, diode-pumped solid-state diode laser (Lambda Photometrics, Harpenden, UK). Time-lapse images were acquired every 0.3secs with 100-200ms exposure for each image. Image acquisition software was built on top of the μManager platform (http://micromanager.org). Image analysis was performed using a custom-built particle tracking algorithm as described before (Tatavarty *et al.*, 2009). Only stationary single molecules of Eos-MLC (which moved less than 1 pixel) were considered for generating PALM images (MLC-PALM immobile), since this is the MLC-fraction which is bound to the actin filaments (Tatavarty et al, 2012). Filopodia with length 2μm or longer were chosen for analysis, and were binned into 4 segments, each of minimum 0.5μm. Individual immobile MLC molecule was assigned to a particular bin segment along the filopodia.

Immunostaining

Cells were washed with PBS at RT and were fixed in gluteraldehyde 2% for 10min at 20°C, then washed with PBS for 30s and permealibized with Triton X-100 0.5% in PBS for 5min at 20°C. Cells are then rinsed with PBS twice at RT and incubated in BSA for 1hr. After 5min wash in PBS the cells were incubated with Acti-Stain 488 (Cytoskeleton Inc., Denver CO) or phalloidin 555 (Cytoskeleton Inc., Denver CO) for 30min.

Staining for β-tubulin was made as described in (Keating *et al.*, 1997). Briefly, the cells were fixed with gluteraldehyde and permeabilized with Triton X-100. Imaging was performed on Zeiss LSM 780, a

combined confocal/FCS/NLO system, mounted on an inverted Axio Observer Z1 with Plan Neofluar 63OilxNA1.25 objective.

Platinum replica electron microscopy

Dissociated rat embryo hippocampal neurons isolated as described previously (Wilcox *et al*., 1994) were obtained from the MINS Neuron Culture Service Center (University of Pennsylvania, Philadelphia, PA). In brief, hippocampi were dissected from brains of Sprague-Dawley rat embryos at embryonic day 18–20 and dissociated into individual cells by incubating in a trypsin-containing solution. The cells were then washed and plated on poly-L-lysine-coated (1 mg/ml) glass coverslips at a concentration of 150,000 cells per 35-mm dish in 1.5 ml neurobasal medium (Gibco) with 2% B27 supplement. Sample preparation for platinum replica electron microscopy was performed as described previously (Svitkina, 2007, 2009). In brief, neuron cultures were detergent extracted for 20 sec at room temperature with 1% Triton X-100 in PEM buffer (100 mM Pipes-KOH, pH 6.9, 1 mM MgCl2, and 1 mM EGTA) containing 2% polyethelene glycol (molecular weight of 35,000), 2 μM phalloidin, and 10 μM taxol. Detergent-extracted samples were sequentially fixed with 2% glutaraldehyde in 0.1 M Na-cacodylate buffer (pH 7.3), 0.1% tannic acid, and 0.2% uranyl acetate; critical point dried; coated with platinum and carbon; and transferred onto electron microscopic grids for observation. Samples were analyzed using JEM 1011 transmission electron microscope (JEOL USA, Peabody, MA) operated at 100 kV. Images were captured by ORIUS 832.10W CCD camera (Gatan, Warrendale, PA) and presented in inverted contrast. Color labeling and image overlays were performed using Adobe Photoshop (Adobe Systems, Mountain View, CA), as described previously (Shutova *et al.*, 2012).

Filopodia length tracking.

Custom-written software FiloTracker was used to track individual filopodia lengths. The use of an automated procedure excluded bias in selection of filopodia and increased the data throughput. Grayscale movies were segmented in ImageJ (National Institutes of Health, Bethesda, MD) and loaded into Matlab (MathWorks, Natick, MA). The individual filopodia length was measured and recorded into output file at each frame (dt=1s). Program output .mat and .csv files which were then imported into Matlab for further

quantitative analysis. For description of the FiloTracker software, refer to the Supplemental Materials (Section 1). The tracks of filopodia motility were smoothed using Gaussian filter to remove noise and the protrusion retraction rates were computed using custom-written script. Filopodium length was estimated as maximum length from the averaged timeseries for each filopodium (mobile and stationary).

The FiloTracker Code is publicly available on: https://github.com/olemarch/FiloTracker

Computational analysis

The model is solved numerically using a semi-implicit Crank-Nicolson scheme coded in Matlab. Filopodium protrusion and retraction rates were computed using peakfinder function by Nathan Yoder, available on Matlab FileExchange: http://www.mathworks.com/matlabcentral/fileexchange/25500-peakfinder-x0--sel--thresh--extrema--includeendpoints--interpolate-. with threshold value 75% from global minimum and maximum for finding local extremes.

Statistical analysis

Statistical analysis was conducted using one-way ANOVA tests with t-tests performed in Matlab. Error bars are mean ± SEM, unless noted otherwise.

Acknowledgements

We thank Dr. Boris Slepchenko, Dr. Yi Wu and Dr. Betty Eipper for valuable discussions on model validation, analysis and interpretations.

Bibliography

Barnhart, E.L., Lee, K.-C., Keren, K., Mogilner, A., and Theriot, J.A. (2011). An adhesion-dependent switch between mechanisms that determine motile cell shape. PLoS Biol *9*, e1001059.

Bausch, A.R., Ziemann, F., Boulbitch, A.A., Jacobson, K., and Sackmann, E. (1998). Local measurements of viscoelastic parameters of adherent cell surfaces by magnetic bead microrheometry. Biophysical journal *75*, 2038-2049.

Beauvais, D.M., and Rapraeger, A.C. (2003). Syndecan-1-mediated cell spreading requires signaling by alphavbeta3 integrins in human breast carcinoma cells. Exp Cell Res *286*, 219-232.

Chan, C.E., and Odde, D.J. (2008). Traction Dynamics of Filopodia on Compliant Substrates. Science *322*, 1687-1691.

Engler, A. (2003). Substrate compliance vs ligand density in cell on gel responses. . European Cells and Materials, 7-8.

Geraldo, S., and Gordon-Weeks, P.R. (2009). Cytoskeletal dynamics in growth-cone steering. J Cell Sci *122*, 3595-3604.

Hochmuth, F., Shao, JY, Dai J, and Sheetz, MP. (1996). Deformation and flow of membrane into tethers extracted from neuronal growth cones. Biophysical journal *70*, 358–369.

Hong, F., Brizendine, R.K., Carter, M.S., Alcala, D.B., Brown, A.E., Chattin, A.M., Haldeman, B.D., Walsh, M.P., Facemyer, K.C., Baker, J.E., and Cremo, C.R. (2015). Diffusion of myosin light chain kinase on actin: A mechanism to enhance myosin phosphorylation rates in smooth muscle. J Gen Physiol *146*, 267-280.

Hotulainen, P., and Hoogenraad, C.C. (2010). Actin in dendritic spines: connecting dynamics to function. J Cell Biol *189*, 619-629.

Irwin, S.A., Galvez, R., and Greenough, W.T. (2000). Dendritic spine structural anomalies in fragile-X mental retardation syndrome. Cereb Cortex *10*, 1038-1044.

Kayser, M.S., Nolt, M.J., and Dalva, M.B. (2008). EphB receptors couple dendritic filopodia motility to synapse formation. Neuron *59*, 56-69.

Keating, T.J., Peloquin, J.G., Rodionov, V.I., Momcilovic, D., and Borisy, G.G. (1997). Microtubule release from the centrosome. Proc Natl Acad Sci U S A *94*, 5078-5083.

Kepiro, M., Varkuti, B.H., Bodor, A., Hegyi, G., Drahos, L., Kovacs, M., and Malnasi-Csizmadia, A. Azidoblebbistatin, a photoreactive myosin inhibitor. Proc Natl Acad Sci U S A *109*, 9402-9407.

Kim, D.H., Khatau, S.B., Feng, Y., Walcott, S., Sun, S.X., Longmore, G.D., Wirtz, D., (2012). Actin cap associated focal adhesions and their distinct role in cellular mechanosensing. Scientific Reports *2*, 555.

Kim, T., Hwang, W., Lee, H., and Kamm, R.D. (2009). Computational analysis of viscoelastic properties of crosslinked actin networks. PLoS Comput Biol *5*, e1000439.

Koestler, S.A., Rottner, K., Lai, F., Block, J., Vinzenz, M., and Small, J.V. (2009). F- and G-actin concentrations in lamellipodia of moving cells. PLoS One *4*, e4810.
Kole, T.P., Tseng, Y., Jiang, I., Katz, J.L., and Wirtz, D. (2005). Intracellular mechanics of migrating fibroblasts. Mol Biol Cell *16*, 328-338.
Kolega, J. (2006). The role of myosin II motor activity in distributing myosin asymmetrically and coupling protrusive activity to cell translocation. Mol Biol Cell *17*, 4435-4445.
Korobova, F., and Svitkina, T. (2010). Molecular architecture of synaptic actin cytoskeleton in hippocampal neurons reveals a mechanism of dendritic spine morphogenesis. Mol Biol Cell *21*, 165-176.
Kovacs, M., Toth, J., Hetenyi, C., Malnasi-Csizmadia, A., and Sellers, J.R. (2004). Mechanism of blebbistatin inhibition of myosin II. J Biol Chem *279*, 35557-35563.
Kruse, K., Joanny, J.F., Julicher, F., Prost, J., and Sekimoto, K. (2004). Asters, vortices, and rotating spirals in active gels of polar filaments. Phys Rev Lett *92*, 078101.
Kuhn, J.R., and Pollard, T.D. (2005). Real-time measurements of actin filament polymerization by total internal reflection fluorescence microscopy. Biophys J *88*, 1387-1402.
Lammermann, T., and Sixt, M. (2009). Mechanical modes of 'amoeboid' cell migration. Curr Opin Cell Biol *21*, 636-644.
Leibler, S., and Huse, D.A. (1993). Porters versus rowers: a unified stochastic model of motor proteins. J Cell Biol *121*, 1357-1368.
Lieber, A.D., Yehudai-Resheff, S., Barnhart, E.L., Theriot, J.A., and Keren, K. (2013). Membrane tension in rapidly moving cells is determined by cytoskeletal forces. Curr Biol *23*, 1409-1417.
Lin, Y.-C., and Koleske, A.J. (2010). Mechanisms of synapse and dendrite maintenance and their disruption in psychiatric and neurodegenerative disorders. Annu Rev Neurosci *33*, 349-378.
Loudon, R.P., Silver, L.D., Yee, H.F., Jr., and Gallo, G. (2006). RhoA-kinase and myosin II are required for the maintenance of growth cone polarity and guidance by nerve growth factor. J Neurobiol *66*, 847-867.
Medeiros, N.A., Burnette, D.T., and Forscher, P. (2006). Myosin II functions in actin-bundle turnover in neuronal growth cones. Nat Cell Biol *8*, 215-226.
Mogilner, A., and Rubinstein, B. (2005). The physics of filopodial protrusion. Biophys J *89*, 782-795.
Nagy A., T.Y., Billington N., Sun S., Hong D., Homsher E., Wang A. and Sellers J. (2013). Kinetic Characterization of Nonmuscle Myosin IIB at the Single Molecule Level. . J. Biol. Chem *288*, 709-722.
Norstrom, M.F., Smithback, P.A., and Rock, R.S. (2010). Unconventional processive mechanics of non-muscle myosin IIB. J Biol Chem *285*, 26326-26334.
Portera-Cailliau, C., Pan, D.T., and Yuste, R. (2003). Activity-regulated dynamic behavior of early dendritic protrusions: evidence for different types of dendritic filopodia. J Neurosci *23*, 7129-7142.

Ryu, J., Liu, L., Wong, T.P., Wu, D.C., Burette, A., Weinberg, R., Wang, Y.T., and Sheng, M. (2006). A critical role for myosin IIb in dendritic spine morphology and synaptic function. Neuron *49*, 175-182.
San Miguel-Ruiz, J.E., and Letourneau, P.C. (2014). The role of arp2/3 in growth cone actin dynamics and guidance is substrate dependent. J Neurosci *34*, 5895-5908.
Segal, M. (1995). Morphological alterations in dendritic spines of rat hippocampal neurons exposed to N-methyl-D-aspartate. Neurosci Lett *193*, 73-76.
Sheetz, M.P. (2001). Cell control by membrane-cytoskeleton adhesion. Nat Rev Mol Cell Biol *2*, 392-396.
Shutova, M., Yang, C., Vasiliev, J.M., and Svitkina, T. (2012). Functions of nonmuscle myosin II in assembly of the cellular contractile system. PLoS One *7*, e40814.
Smith, B.A., Roy, H., De Koninck, P., Grutter, P., and De Koninck, Y. (2007). Dendritic spine viscoelasticity and soft-glassy nature: balancing dynamic remodeling with structural stability. Biophys J *92*, 1419-1430.
Svitkina, T. (2007). Electron microscopic analysis of the leading edge in migrating cells. Methods Cell Biol *79*, 295-319.
Svitkina, T. (2009). Imaging cytoskeleton components by electron microscopy. Methods Mol Biol *586*, 187-206.
Tatavarty, V., Das, S., and Yu, J. (2012). Polarization of actin cytoskeleton is reduced in dendritic protrusions during early spine development in hippocampal neuron. Mol Biol Cell *23*, 3167-3177.
Tatavarty, V., Kim, E.-J., Rodionov, V., and Yu, J. (2009). Investigating Sub-Spine Actin Dynamics in Rat Hippocampal Neurons with Super-Resolution Optical Imaging. PLoS ONE *4*, e7724.
Verkhovsky, A.B., Svitkina, T.M., and Borisy, G.G. (1995). Myosin II filament assemblies in the active lamella of fibroblasts: their morphogenesis and role in the formation of actin filament bundles. J Cell Biol *131*, 989-1002.
Wilcox, K.S., Buchhalter, J., and Dichter, M.A. (1994). Properties of inhibitory and excitatory synapses between hippocampal neurons in very low density cultures. Synapse *18*, 128-151.
Wilson, C.A., Tsuchida, M.A., Allen, G.M., Barnhart, E.L., Applegate, K.T., Yam, P.T., Ji, L., Keren, K., Danuser, G., and Theriot, J.A. (2010). Myosin II contributes to cell-scale actin network treadmilling through network disassembly. Nature *465*, 373-377.
Wu, J.Q., and Pollard, T.D. (2005). Counting cytokinesis proteins globally and locally in fission yeast. Science *310*, 310-314.
Yamashiro, S., and Watanabe, N. (2014). A new link between the retrograde actin flow and focal adhesions. J Biochem *156*, 239-248.

Ziv, N.E., and Smith, S.J. (1996). Evidence for a role of dendritic filopodia in synaptogenesis and spine formation. Neuron *17*, 91-102.

Figures.

Figure 1.

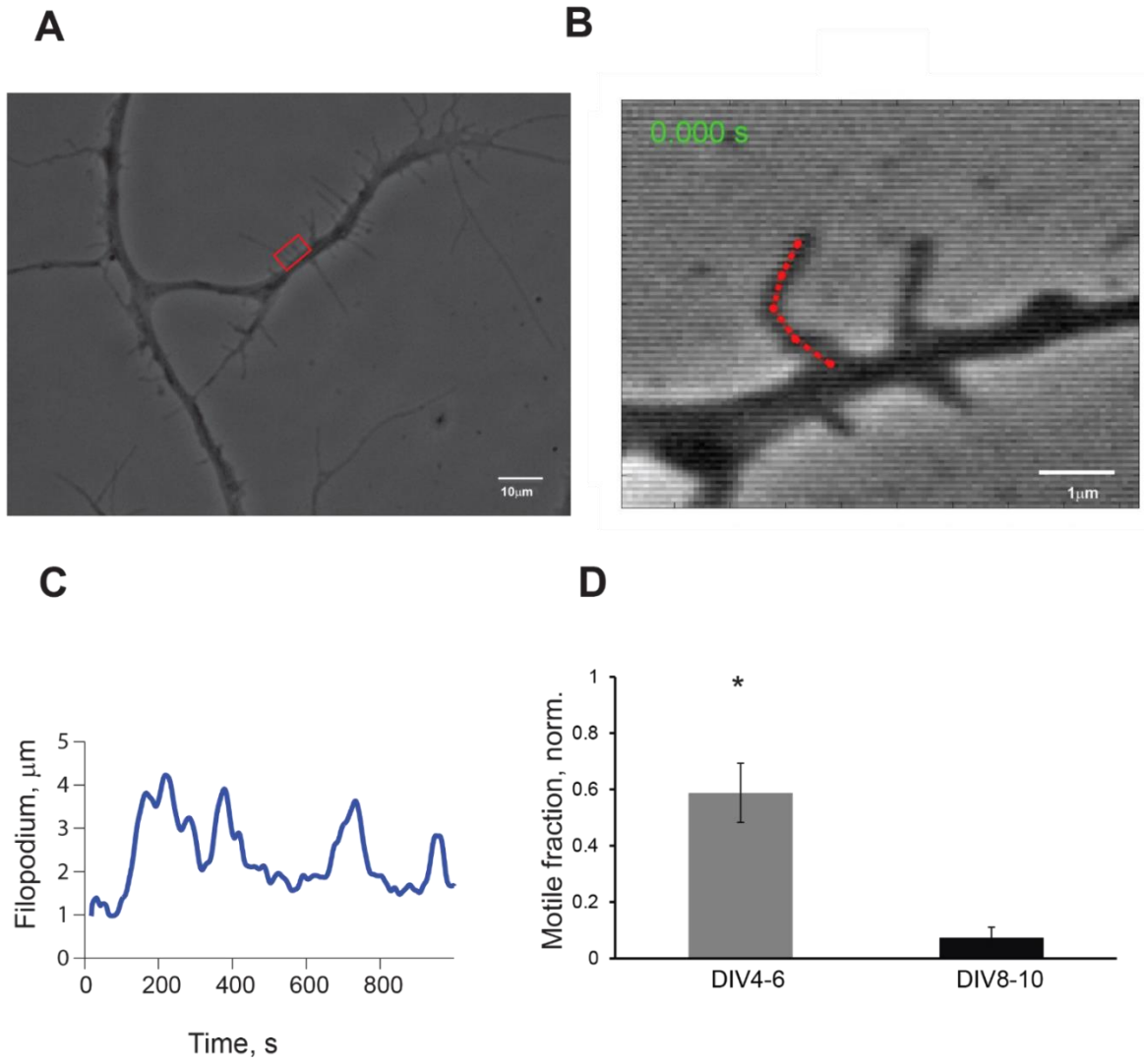

Figure 1. Analysis of filopodia motility with automated tracking software FiloTracker A. Phase-contrast image of hippocampal pyramidal neuron in culture, DIV5, with dendrites covered with filopodia; scale bar 10µm. B. High magnification image of boxed area shown in panel A during length tracking process in FiloTracker; red dotted line is a length estimate for the current frame; scale bar 2 µm. C. Output sample of length measurements from the filopodia on B (red), acquisition rate= 1f/s, periodicity of length is ~ 122±19s. D. Comparison of motile fraction of all filopodia in imaging session (t=30 mins) at DIV4-9 and DIV8-10 (t-test $P<0.05$).

Figure 2.

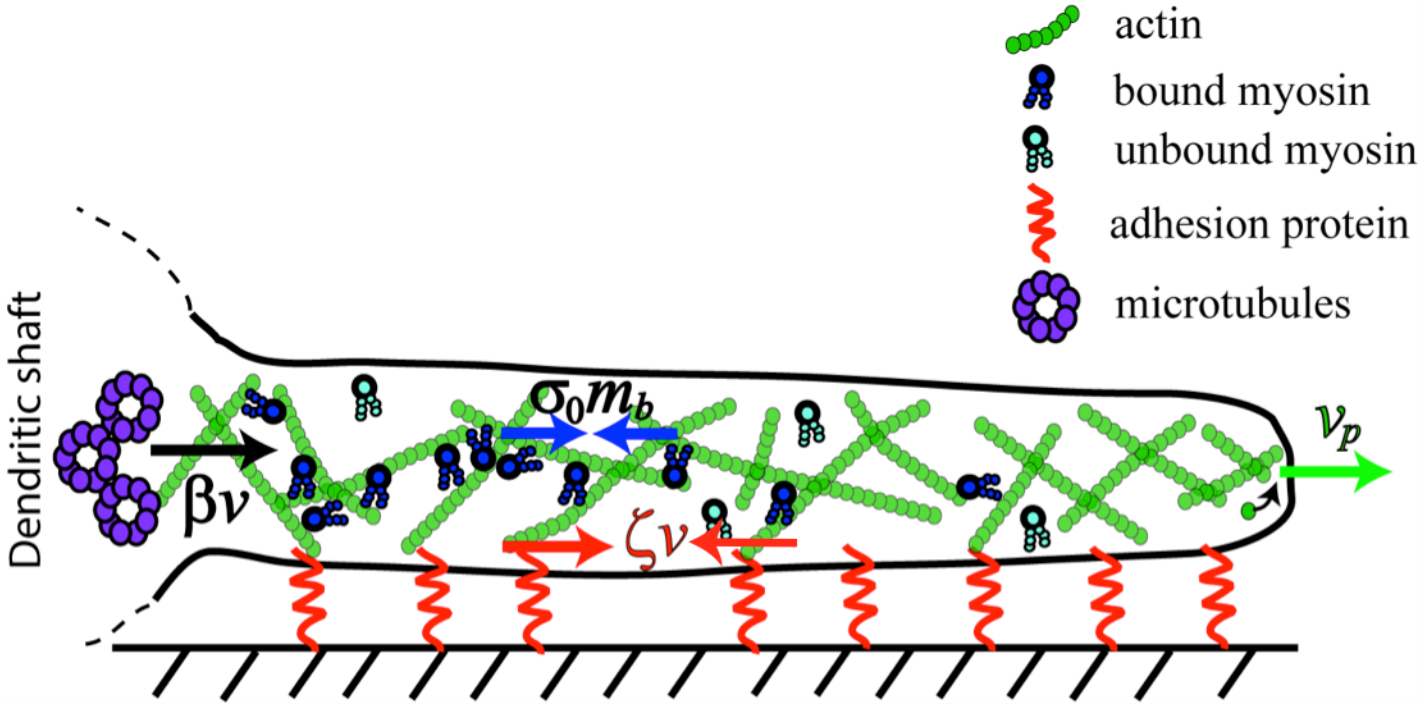

Figure 2. Cartoon that illustrates the balance of forces in a dendritic filopodium described by the minimal model. The model captures five essential processes: a) polymerization of F-actin at the tip of the filopodium; b) binding and unbinding of myosin to F-actin; c) isotropic contractile stresses exerted by bound myosin on F-actin; d) viscous flow of F-actin (ARF) induced by these contractile stresses and membrane tension; e) friction between the filopodium and the substrate due to adhesion. Bound myosin contractile stress is shown by blue arrows σ_0, m_b, v_p - polymerization rate, direction is indicated by green arrow, ζv – the substrate adhesion force is denoted by the red arrow, and black arrow is βv– resistance force at the base due to microtubule network inside the dendrite. Unbound myosin freely diffuses inside the filopodium.

Figure 3.

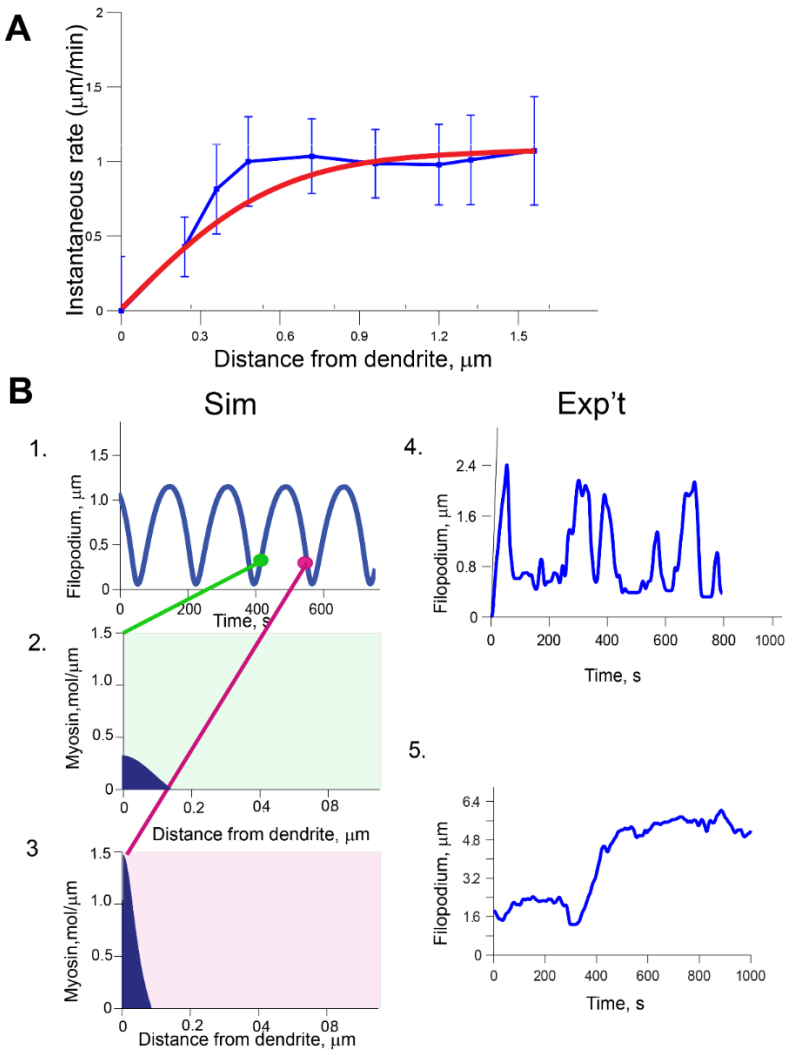

Figure 3. Model solutions correspond to experimental data. A. Fit of simulated actin flow velocity at steady state(red) (*Eq.1*) with experimental ARF distribution along normalized filopodium length (blue); (Tatavarty *et al.*, 2012), mean± S.D. Parameter values: L_0 =1, k_{off}=0.13, k_{on}=0.12,v_p=0.9, m_0 = 25, η =100, ζ=100, σ_0 =25, β=5250, D=0.04 B. 1. Simulated filopodium length fluctuations with retrograde flow from A. Myosin distribution taken close to the most rapid phases of (2.) protrusion and (3.) retraction. L_0 =1, k_{off}=0.13, k_{on}=0.12,v_p=0.9, m_0 = 25, η =100, ζ=100, σ_0 =25, β=5250, D=0.04
4. Representative dynamics of a live filopodium traced using automated software, acxcquisition rate = 1f/s. 5. Dynamics of a live filopodium with large amplitude of fluctuations traced using automated software, acquisition rate = 1f/s. (Note y axes in 4 and 5).

Figure 4.

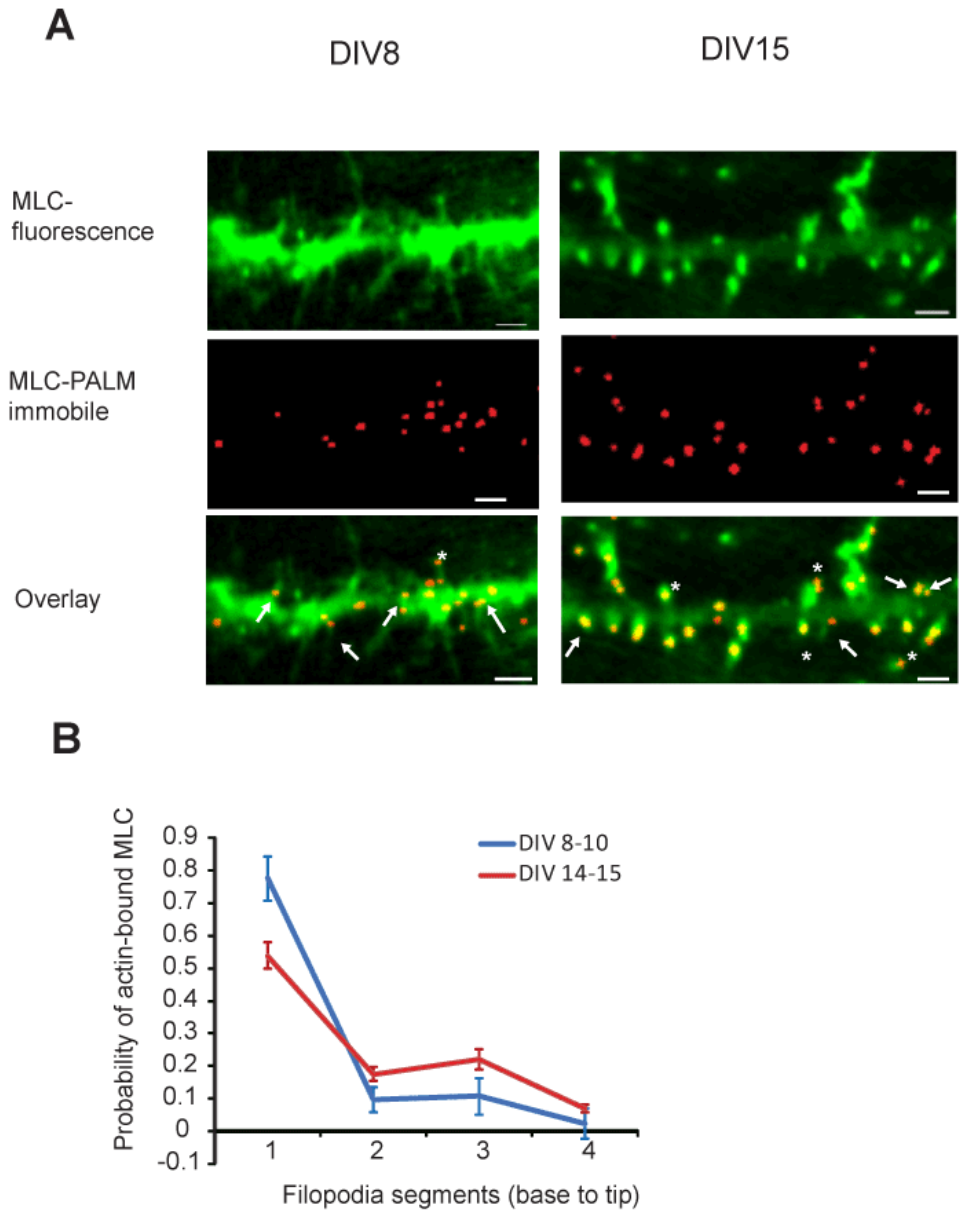

Figure 4. Localization of myosin (MLC) in dendrites using PALM imaging. A. Top, epifluorescence images of neurons transfected with Eos-MLC. Middle, corresponding PALM images constructed with only the immobile subpopulation of the molecules. Bottom, overlay of the top and middle images. Arrowheads indicate immobile MLC localization in the base of the filopodia. Asterisks indicate immobile MLC localization in the spine heads. Scale bar, 5 μm. B. Probability of MLC to be found in one of the four segments of the filopodium during early development (DIV8-10, 26 filopodia) vs late development (DIV 14-15, 25 filopodia), error bars represent SEM; numbers indicate relative distance from the base.

Figure 5.

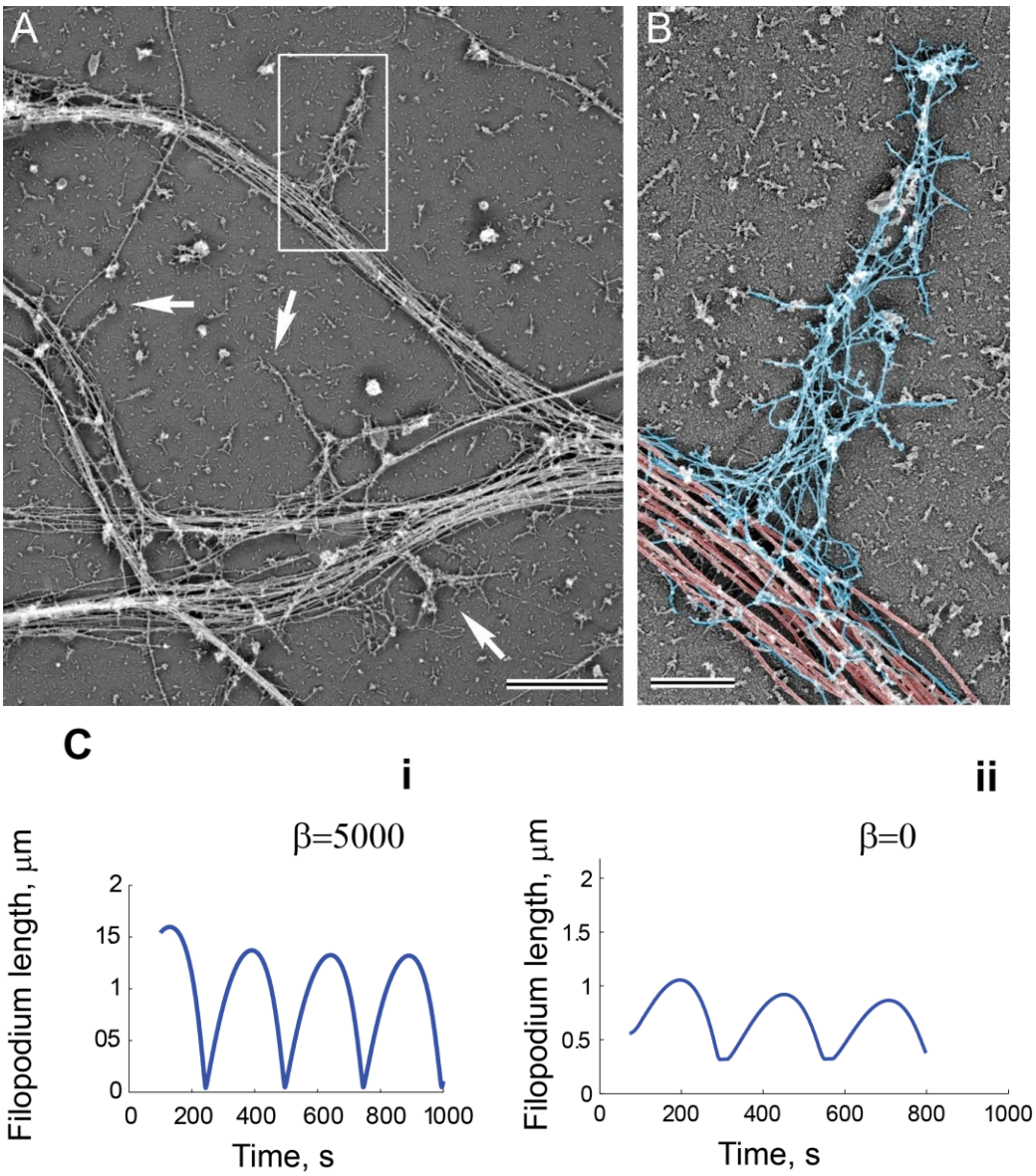

Filopodia dynamics depends on the resistive force applied at the base by the microtubule network. Cytoskeletal organization of dendritic filopodia revealed by platinum replica electron microscopy. (A) A network of dendrites from hippocampal neurons cultured for 8 days in vitro. Dendritic filopodia (boxed region and arrows) reside on dense arrays of microtubules in dendrites. (B) Dendritic filopodium from the boxed region in A is color-coded to show microtubules in the dendrite (red) and actin filaments in the filopodium (blue). Scale bars: 2 um (A) and 0.5 um (B). C. Simulated filopodia dynamics with i) and without ii) resistive force at the barrier. i) L_0 =1, k_{off}=0.13, k_{on}=0.12,v_p=0.9, m_0 = 25, η =100, ζ=100, σ_0 =25, β=5250, D=0.04 ii) L_0 =1, k_{off}=0.13, k_{on}=0.12,v_p=0.9, m_0 = 25, η =100, ζ=100, σ_0 =25, β=0, D=0.04

Figure 6.

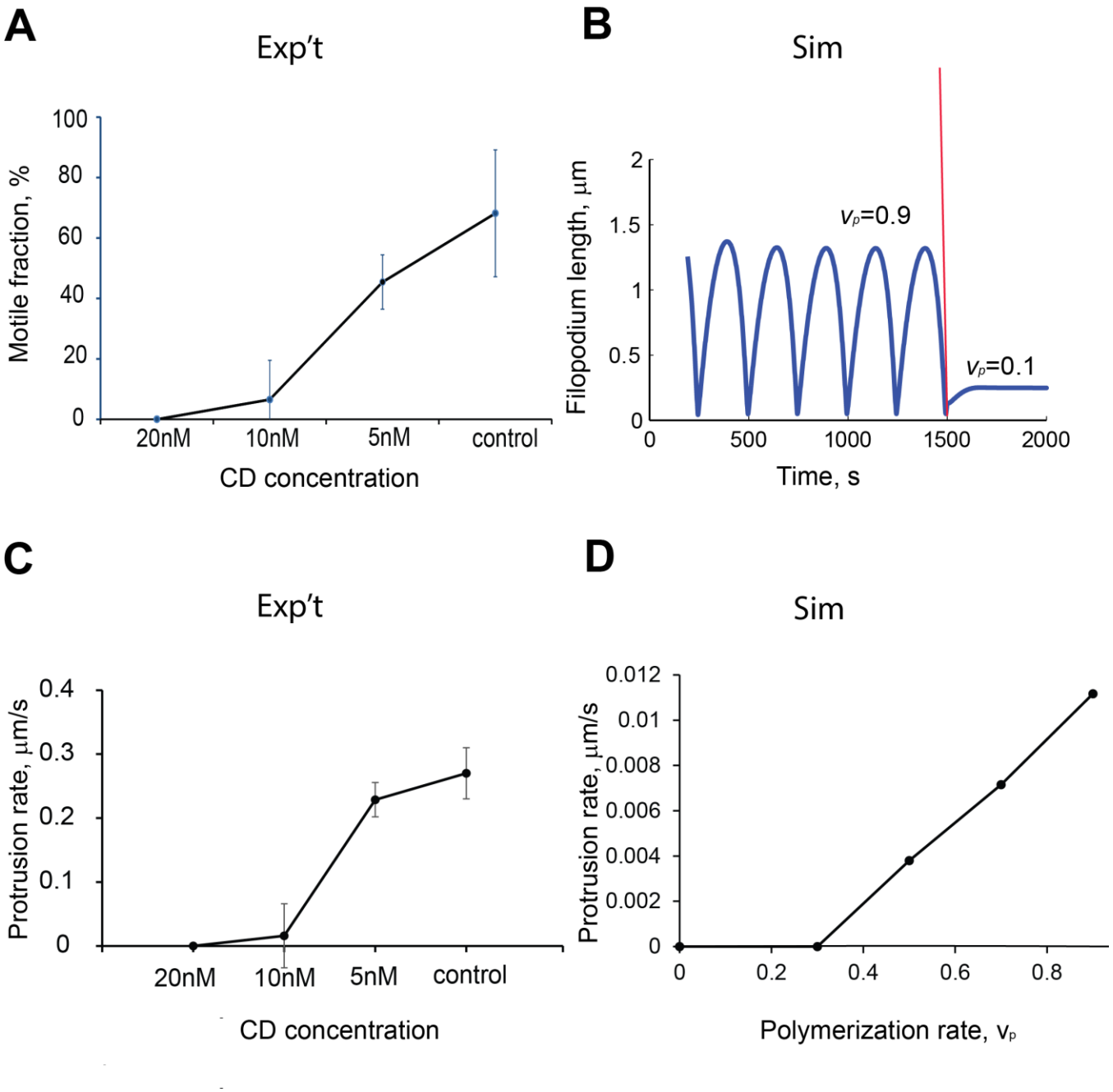
A
Exp't
Motile fraction, %
100
80
60
40
20
0
20nM
10nM
5nM
control
CD concentration
B
Sim
Filopodium length, µm
2
1.5
1
0.5
0
v_p=0.9
v_p=0.1
0
500
1000
1500
2000
Time, s
C
Exp't
Protrusion rate, µm/s
0.4
0.3
0.2
0.1
0
20nM
10nM
5nM
control
CD concentration
D
Sim
Protrusion rate, µm/s
0.012
0.01
0.008
0.006
0.004
0.002
0
0
0.2
0.4
0.6
0.8
Polymerization rate, v_p

Effect of actin polymerization rate on filopodial motility. A. Percent motile filopodia as a function of CD concentration; one-way ANOVA $P<0.001$ for the 20nM dose compared to each of the lower doses (201 filopodia, 21 neurons, error bars are SD). B. Simulated changes in filopodial motility after decreasing actin polymerization rate, v_p from 0.9 to 0.1. Other parameter values are: L_0 =1, k_{off}=0.13, k_{on}=0.12, m_0 = 25, η =100, ζ=100, σ_0 =25, β=5250, D=0.04 (Eq.7) C. Effect of CD treatment on the protrusion rate of motile filopodia, one-way ANOVA $P<0.001$, for the 20nM dose compared to each of the lower doses (124 filopodia, 18 neurons; error bars are SEM). D. Protrusion rates from simulated filopodial dynamics using a range of polymerization rate values, vp [0-0.9]. Other parameters used in the simulations L_0 =1, k_{off}=0.13, k_{on}=0.12,v_p=0.9, m_0 = 25, η =100, ζ=100, σ_0 =25, β=5250, D=0.04.

Figure 7.

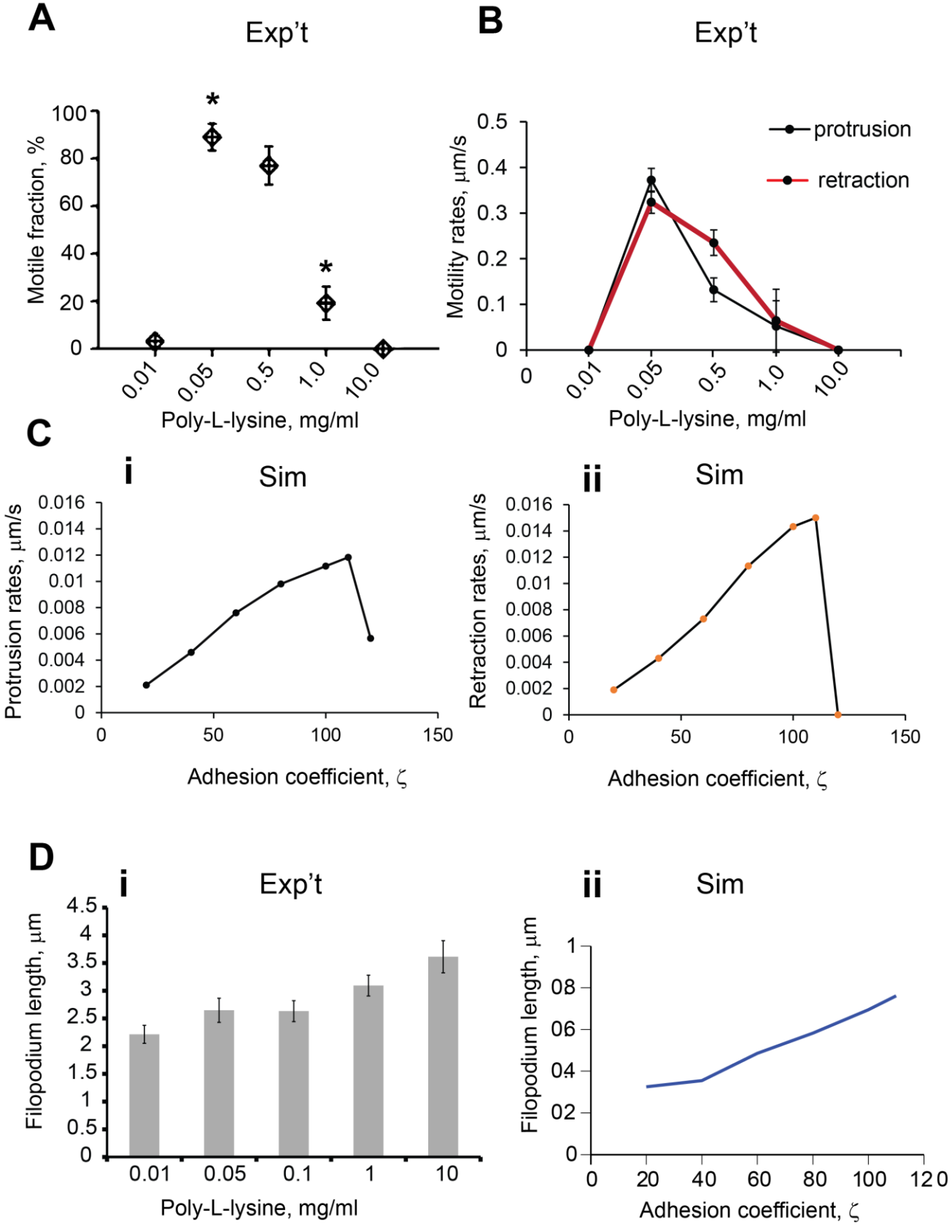
A
Exp't
Motile fraction, %
100
80
60
40
20
0
*
*
0.01
0.05
0.5
1.0
10.0
Poly-L-lysine, mg/ml
B
Exp't
Motility rates, µm/s
0.5
0.4
0.3
0.2
0.1
0
protrusion
retraction
0
0.01
0.05
0.5
1.0
10.0
Poly-L-lysine, mg/ml
C
i
Sim
Protrusion rates, µm/s
0.016
0.014
0.012
0.01
0.008
0.006
0.004
0.002
0
0
50
100
150
Adhesion coefficient, ζ
ii
Sim
Retraction rates, µm/s
0.016
0.014
0.012
0.01
0.008
0.006
0.004
0.002
0
0
50
100
150
Adhesion coefficient, ζ
D
i
Exp't
Filopodium length, µm
4.5
4
3.5
3
2.5
2
1.5
1
0.5
0
0.01
0.05
0.1
1
10
Poly-L-lysine, mg/ml
ii
Sim
Filopodium length, µm
1
08
06
04
02
0
0
20
40
60
80
100
120
Adhesion coefficient, ζ

Figure 7. pLL-substrate adhesion strength regulates filopodial motility. A. The highest number of motile filopodia was observed on substrates with medium pLL concentration; using one-way ANOVA, motile fraction at 0.05 and 0.5 mg/ml were not significantly different from each other, but they were each significantly different than the filopodia at 0.01, 1.0 and 10.0mg/ml (433 filopodia, 36 neurons, $P<0.001$; ANOVA, error bars are SEM). B. Protrusion and retraction rates from filopodia grown on substrates of different pLL concentration (DIV4-5, 316 filopodia, 20 neurons); using one-way ANOVA, motility rates at 0.05 and 0.5 mg/ml were significantly different from each other, and they were each significantly different from the less motile filopodia at 0.01, 1.0 and 10.0mg/ml ($P<0.001$; error bars are SEM). C. Protrusion and retraction rates from simulated filopodia within adhesion coefficient range (20:115) demonstrate a biphasic relationship between adhesion forces and filopodial dynamics. The simulations are initiated with bound myosin (m_b) = 0 and Length ($L_{0)}$ =1μm; they both quickly approach non-motile steady state lengths, bracketing the intermediate ζ values that produce oscillations. Other parameters in these simulations are: L_0 =1, k_{off}=0.13, k_{on}=0.12,v_p=0.9, m_0 = 25, η =100, σ_0 =25, β=5250, D=0.04. D. Comparison of filopodial length change in modeling and experimental results: i) average filopodial lengths on the range of pLL concentrations (433 filopodia, 36 neurons, ANOVA, $P<0.005$; error bars are SEM; Tukey post hoc test: Group 0.1mg/ml has mean not statistically different from other groups; other four groups have means statistically different from each other. ii) simulated filopodia lengths in the range of the drag force parameter ζ[20,110].

Figure 8.

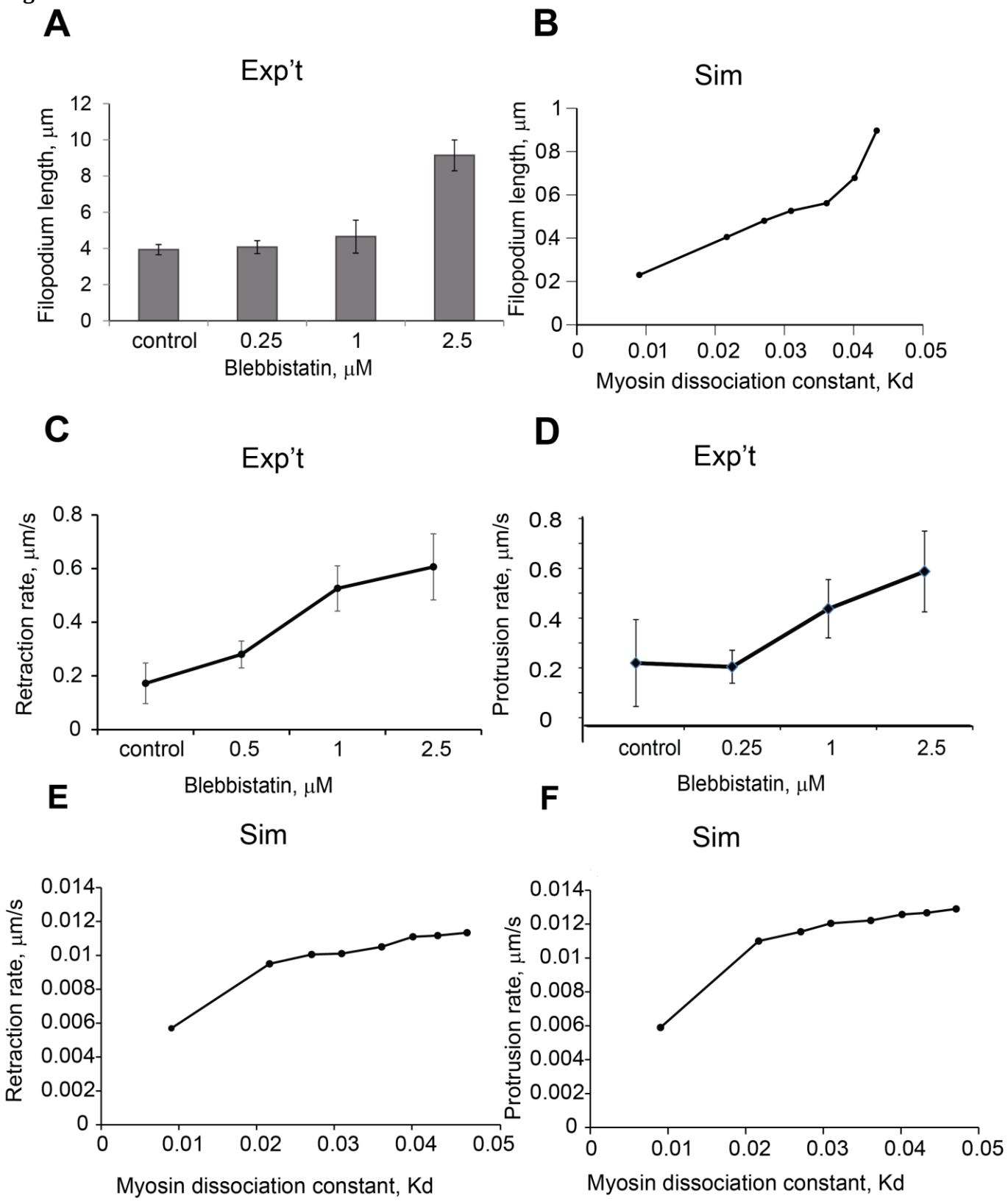
A
Exp't
Filopodium length, μm
12
10
8
6
4
2
0
control
0.25
1
2.5
Blebbistatin, μM
B
Sim
Filopodium length, μm
1
08
06
04
02
0
0
0.01
0.02
0.03
0.04
0.05
Myosin dissociation constant, Kd
C
Exp't
Retraction rate, μm/s
0.8
0.6
0.4
0.2
0
control
0.5
1
2.5
Blebbistatin, μM
D
Exp't
Protrusion rate, μm/s
0.8
0.6
0.4
0.2
0
control
0.25
1
2.5
Blebbistatin, μM
E
Sim
Retraction rate, μm/s
0.014
0.012
0.01
0.008
0.006
0.004
0.002
0
0
0.01
0.02
0.03
0.04
0.05
Myosin dissociation constant, Kd
F
Sim
Protrusion rate, μm/s
0.014
0.012
0.01
0.008
0.006
0.004
0.002
0
0
0.01
0.02
0.03
0.04
0.05
Myosin dissociation constant, Kd

Figure 8. Dependence of filopodial lengths and retraction rates on myosin Kd. A. Filopodial lengths after treatment with blebbistatin; significantly longer filopodia were observed after treatment with 1.0μM and 2.5μM doses of blebbistatin, when compared to control, one-way ANOVA $P<0.001$ (95 filopodia, 12 neurons), error bars are SEM. B. Simulated filopodial lengths on the range of Kd [0.01, 0.05] C. Filopodial retraction rates after treatment with blebbistatin;the highest retraction rate was observed at blebbistatin treatment of 2.5μM (DIV4-5, 78 filopodia, 12 neurons, ANOVA, $P<0.001$. D) Filopodial protrusion rates after treatment with blebbistatin; the highest protrusion rate was observed at blebbistatin treatment of 2.5μM (DIV4-5, 78 filopodia, 12 neurons, ANOVA, $P<0.001$. E) Simulated filopodial retraction rates on the range of Kd [0.01, 0.05]; the highest retraction rate was observed at the highest Kd. Parameters used for the simulations are: L_0 =1, k_{off}=0.13, k_{on}=0.12,v_p=0.9, m_0 = [23-120], η =100, ζ=100, σ_0 =25, β=5250, D=0.04. F) Simulated filopodial protrusion rates on the range of Kd [0.01, 0.05]; the highest protrusion rate was observed at the highest Kd. Parameters used for the simulations are: L_0 =1, k_{off}=0.13, k_{on}=0.12,v_p=0.9, m_0 = [23-120], η =100, ζ=100, σ_0 =25, β=5250, D=0.04.

Figure 9.

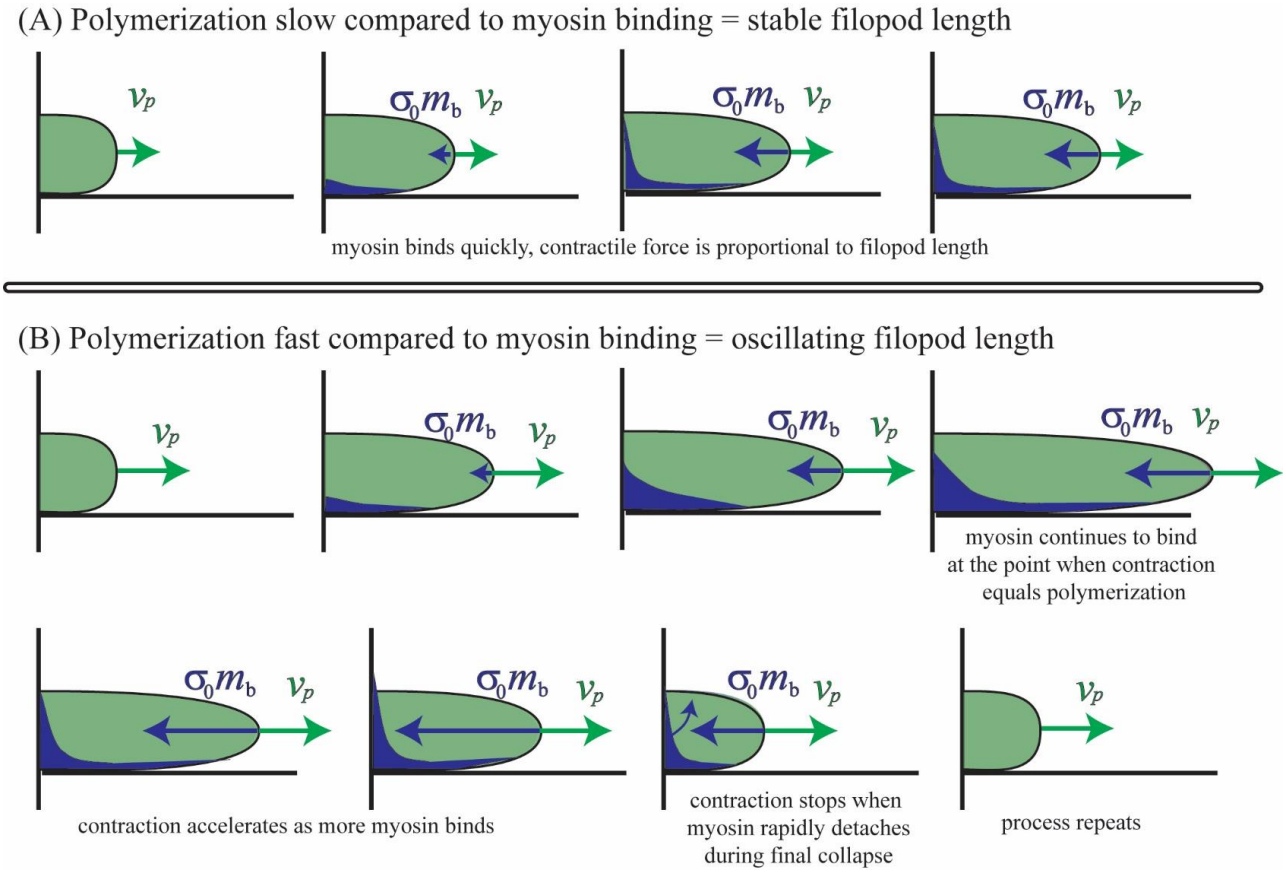
(A) Polymerization slow compared to myosin binding = stable filopod length
v_p
$\sigma_0 m_b$ v_p
$\sigma_0 m_b$ v_p
$\sigma_0 m_b$ v_p
myosin binds quickly, contractile force is proportional to filopod length
(B) Polymerization fast compared to myosin binding = oscillating filopod length
v_p
$\sigma_0 m_b$ v_p
$\sigma_0 m_b$ v_p
$\sigma_0 m_b$ v_p
myosin continues to bind at the point when contraction equals polymerization
$\sigma_0 m_b$ v_p
$\sigma_0 m_b$ v_p
$\sigma_0 m_b$ v_p
v_p
contraction accelerates as more myosin binds
contraction stops when myosin rapidly detaches during final collapse
process repeats

Figure 9. Summary of filopodium non-motile (A) and motile (B) behaviors. A. Non-motile filopodium. The length of filopodium does not change when myosin dynamics is fast enough to counteract the protrusion rate produced by actin polymerization. B. Motile filopodium undergoes protrusion-peak-retraction cycle. At small lengths the total amount of bound myosin is low; hence, retrograde flow is insufficient to overcome polymerization velocity, which results in gradual length increase. Filopodium reaches its maximum length when actin retrograde flow at the tip equals exactly to actin polymerization rate. Peak is followed by retraction stage, which is characterized by the large magnitudes of actin retrograde flow due to large amounts of bound myosin. The retraction lasts until the length is so small that the amount of bound myosin is low, which allows actin polymerization to increase the filopodial length and initiate the protrusion phase. This leads to the cyclical changes in filopodial length.

Supplemental Materials

2. Supplemental Tables and Figures

Table S1. Parameter values for nominal case result in ARF and myosin localization profiles that match experimental data.

Forces/Processes	Parameter	Physical significance	Value range	Units	Reference/source
Force due to viscous flow of actin	η	Viscosity	100	$pN \cdot s$	(Bausch *et al.*, 1998)
Myosin contractility	σ_0	myosin contractility	25	$\frac{pN \cdot \mu m}{molecule}$	Non-dimensional analysis
Adhesion Force	ζ	drag force coefficient	100	$\frac{pN \cdot s}{\mu m^2}$	(Chan and Odde, 2008)
Myosin binding	k_{off} / $k_{on,\ Kd}$	myosin binding rate	0.9310	nM	(Norstrom *et al.*, 2010)
Actin polymerization	v_p	polymerization rate	0.9	$\frac{\mu m}{s}$	(Tatavarty *et al.*, 2012)
Initial filopodia length	L_0	initial length	1	µm	experimental data
Diffusion	D	diffusion coefficient	0.04	$\mu m^2/s$	Calculated from myosin random walk
Resistive force	β	Resistive force coefficient	5250	$\frac{pN \cdot s}{\mu m}$	Parameter screening
Unbound myosin concentration	m_0	Unbound myosin	25	Molecules/µm	Non-dimensional analysis
Membrane tension	$T\kappa$	Tension force on the cell membrane due to curvature	2.0	pN	(Hochmuth, 1996)

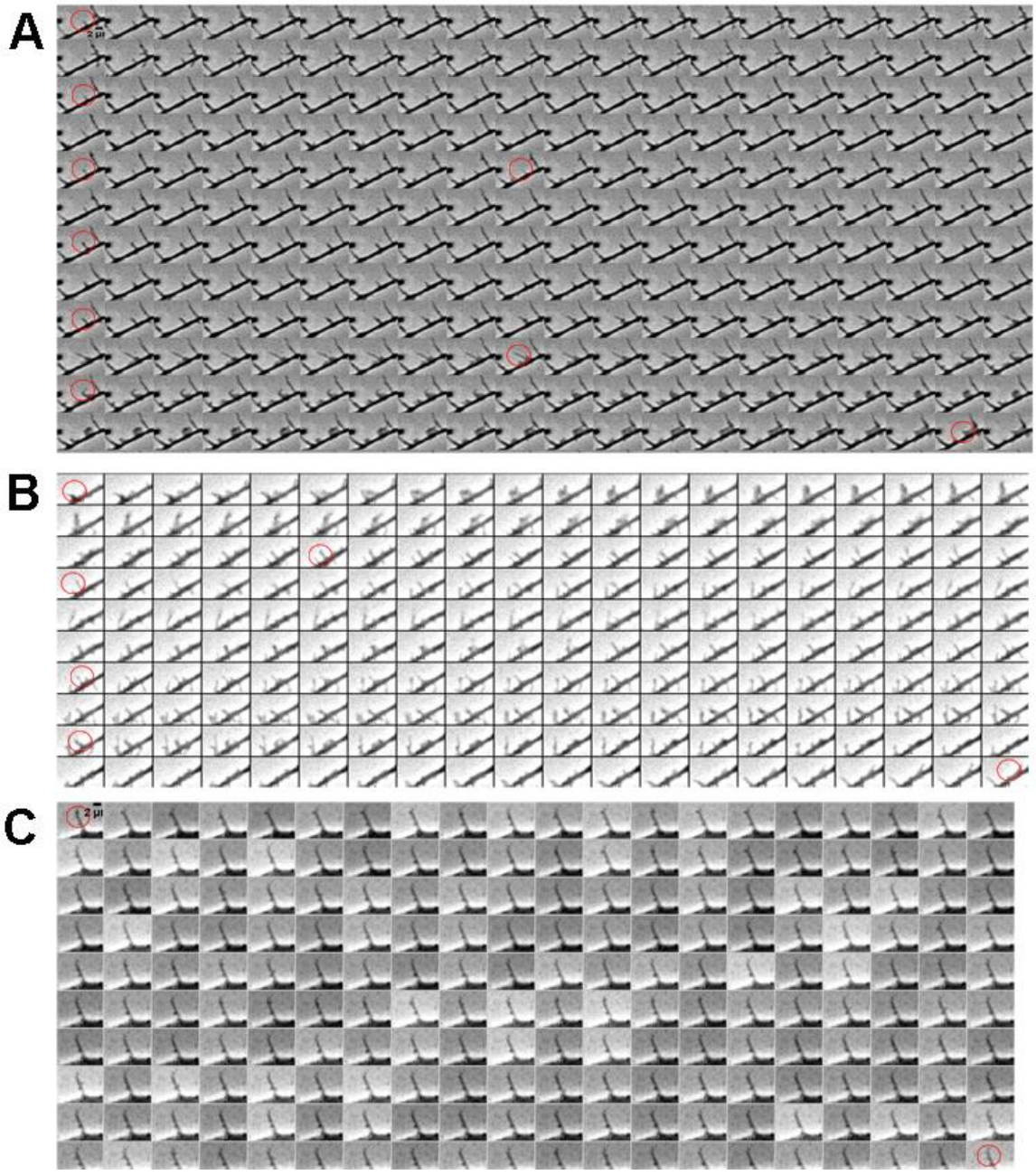

Figure S1. Montage of sequential phase-contrast images taken with acquisition rate 1f/s of different types of filopodial motility A. Continuously motile filopodia exhibit regular lengths fluctuations and have long lifetimes. B. Transiently motile filopodia have short lifetimes with burst dynamics. C. Non-motile filopodia have constant lengths over long periods of times.

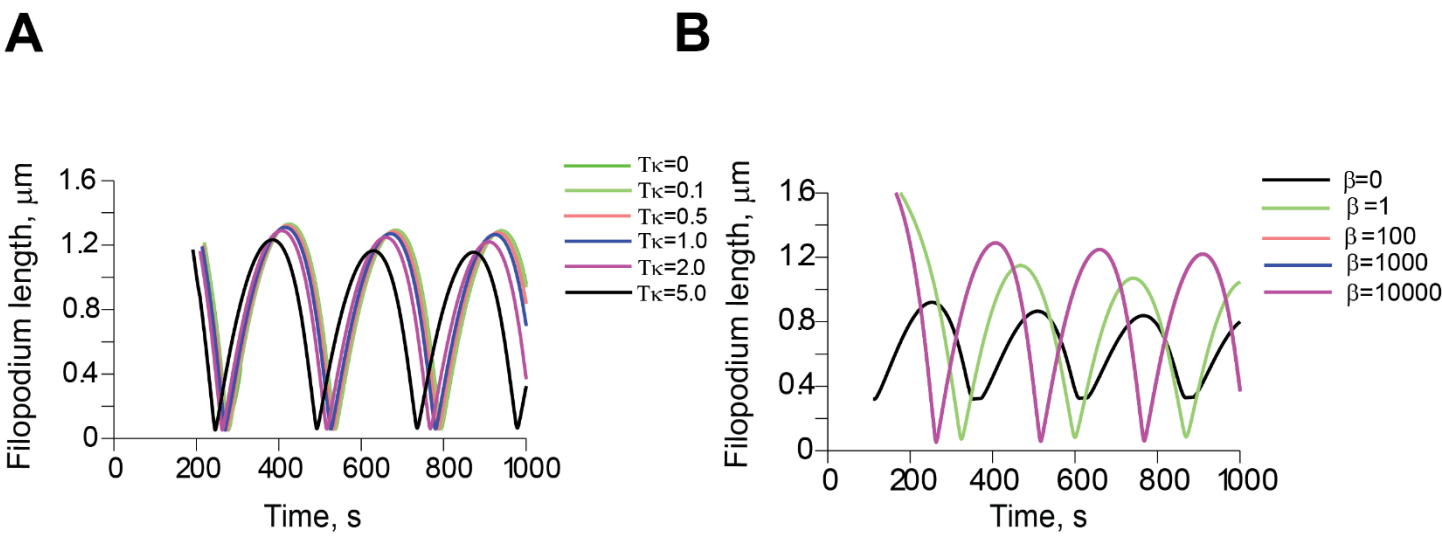

Figure S2. Sensitivity analysis for parameters Tκ. β. A. Model's output for a Tκ range [0,5.0]$\boldsymbol{pN}$. B. Qualitative description of resistance force parameter β significance. β values >100 result in steady-state with oscillations. Parameters used for the simulations are L_0 =1, k_{off}=0.13, k_{on}=0.12,v_p=0.9, m_0 = 25, η =100, ζ=100, σ_0 =25, D=0.04

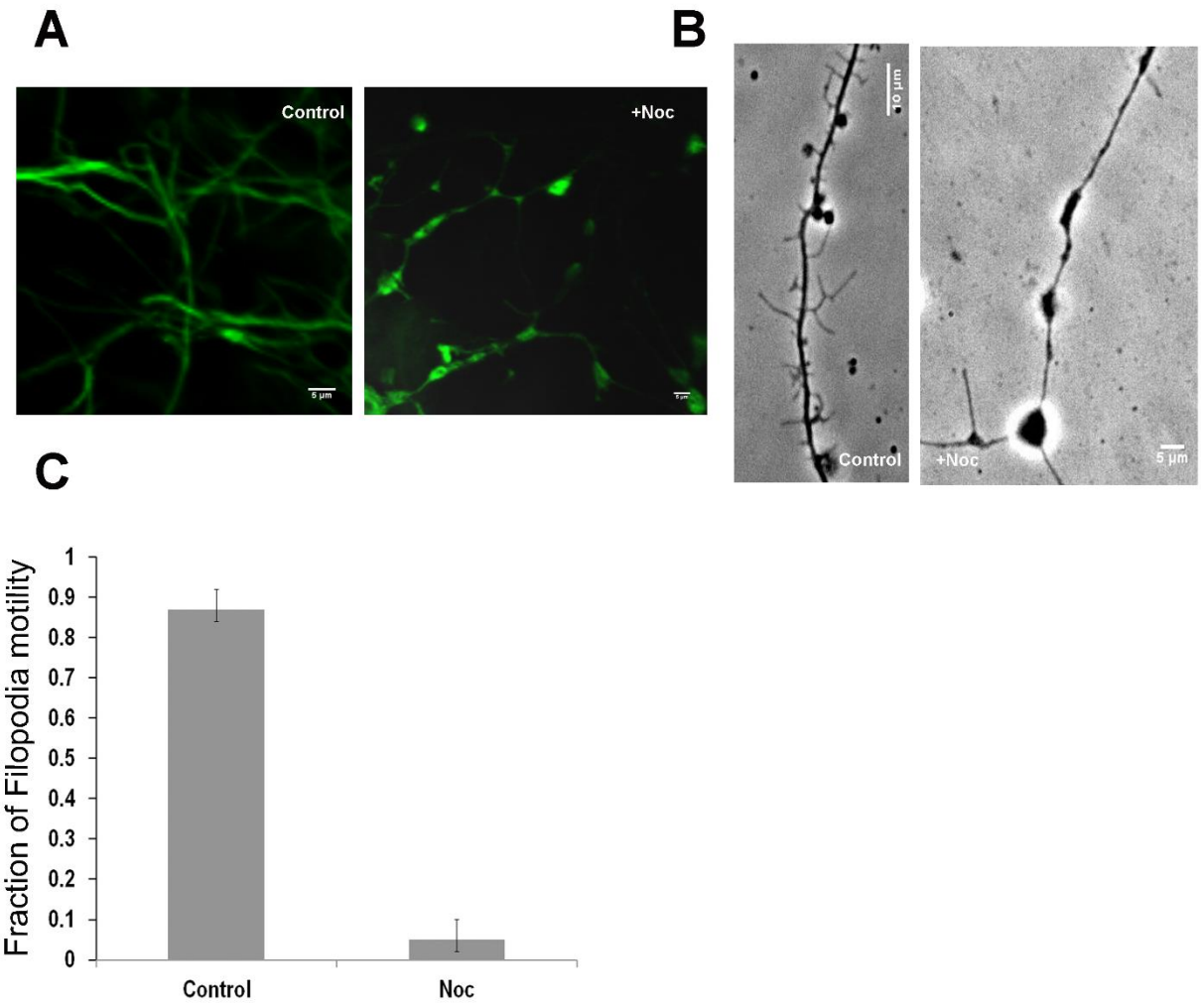

Figure S3. Nocodazole treatment reduces filopodia motility and number. Control neuron cultures and neurons treated with 1.6µM nocodazole after 1hr incubation at 37°C on DIV4 shown with (A) 488-Alexa tubulin staining or (B) phase-contrast microscopy. C. fraction of motile filopodia in nocodazole treated cells, t-test, $P<0.05$ (32 filopodia, 8 neurons).

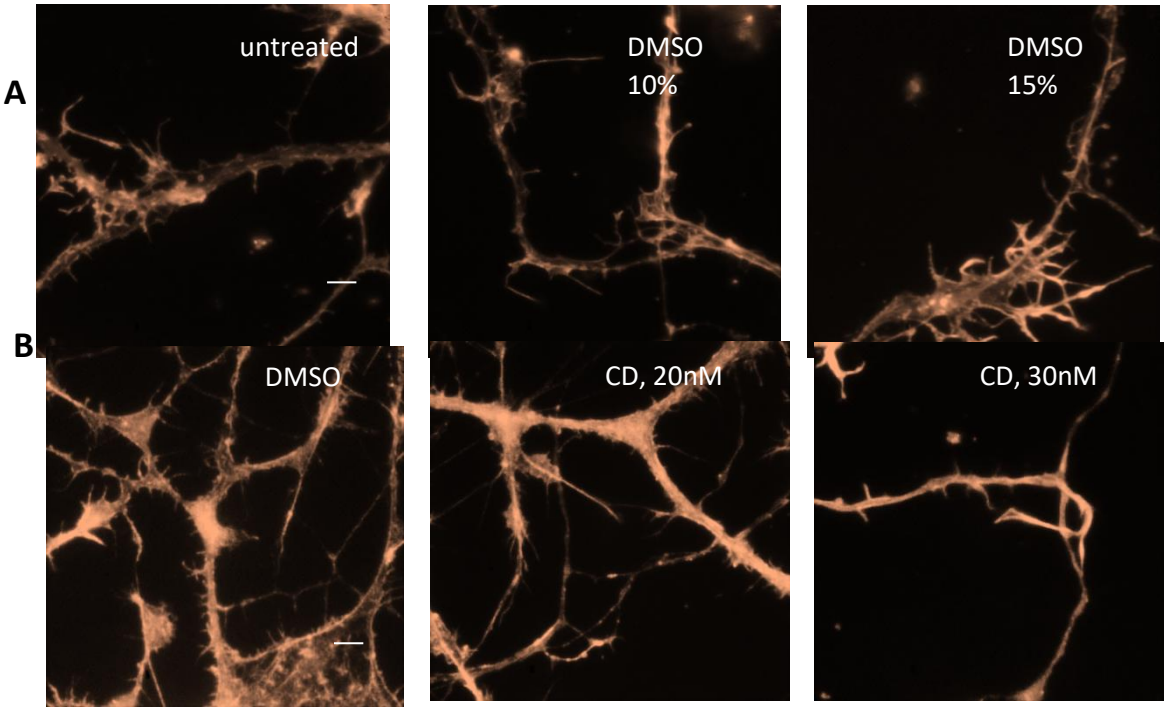

Figure S4. Cytochalasin D and DMSO treatments have not disrupted filamentous actin in aconcentrations used in the drug assays as shown by rhodamine staining of F-actin following drug administration. A. Control DMSO treatment did not have significant effect on density and structure of filamentous actin. B. Cytochalasin D treatment at treatment did not have significant effect on density and structure of filamentous actin at 20nM. Treatment with 30nM CD resulted in significant reduction of filopodia motility and changes in actin network compared to control. Scale bar 10μm

3. List of Supplemental Movies

MovieS1. Filopodium length tracked with FiloTracker Software (red dotted line), acquisition rate =4f/s, play rate 100 f/s, rat hippocampal neuron culture, DIV4, poly-L-lysine 0.5mg/ml, bar 10µm

MovieS2A. - Filopodia motility after 20nM cytochalasin D treatment. rat hippocampal neuron culture, DIV4-7, poly-L-lysine 0.5mg/ml, acquisition rate =1f/s, play rate 100 fr/s ,bar 10µm,

MovieS2B .Filopodia motility after 10nM cytochalasin D treatment, rat hippocampal neuron culture, DIV4-7, poly-L-lysine 0.5mg/ml, acquisition rate =1f/s, bar 10µm, play rate 100 fr/s

MovieS3A. Filopodia motility on poly-L-lysine substrate with 0.05mg/ml, rat hippocampal neuron culture, DIV4-7, acquisition rate =1f/s, bar 10µm, play rate 100 fr/s

MovieS3B. Reduced filopodia motility on poly-L-lysine substrate with 0.01mg/ml, rat hippocampal neuron culture, DIV4-7, acquisition rate =1f/s, play rate 100 fr/s, bar 5µm

MovieS3C. Reduced filopodia motility on poly-L-lysine substrate with 1.00mg/ml, rat hippocampal neuron culture, DIV4-7, acquisition rate =1f/s, play rate 100 fr/s, bar 10µm

MovieS4. Increased filopodia motility and length in the presence of 2.5µM blebbistatin, rat hippocampal neuron culture, DIV4-7, acquisition rate =1f/s, play rate 100 fr/s, bar 10µm

4. Supplemental References

1. Isard M, Blake A. 1998. Conditional density propagation for visual tracking. *International Journal of Computer Vision* 29: 4
2. Norstrom MF, Smithback PA, Rock RS. 2010. Unconventional processive mechanics of non-muscle myosin IIB. *J Biol Chem* 285: 26326

Legends to Supplemental Movies

MovieS1. Filopodium length tracked with FiloTracker Software (red dotted line), acquisition rate =4f/s, play rate 100 f/s, rat hippocampal neuron culture, DIV4, poly-L-lysine 0.5mg/ml, bar 10μm

MovieS2A. - Filopodia motility after 20nM cytochalasin D treatment. rat hippocampal neuron culture, DIV4-7, poly-L-lysine 0.5mg/ml, acquisition rate =1f/s, play rate 100 fr/s ,bar 10μm,

MovieS2B .Filopodia motility after 10nM cytochalasin D treatment, rat hippocampal neuron culture, DIV4-7, poly-L-lysine 0.5mg/ml, acquisition rate =1f/s, bar 10μm, play rate 100 fr/s

MovieS3A. Filopodia motility on poly-L-lysine substrate with 0.05mg/ml, rat hippocampal neuron culture, DIV4-7, acquisition rate =1f/s, bar 10μm, play rate 100 fr/s

MovieS3B. Reduced filopodia motility on poly-L-lysine substrate with 0.01mg/ml, rat hippocampal neuron culture, DIV4-7, acquisition rate =1f/s, play rate 100 fr/s, bar 5μm

MovieS3C. Reduced filopodia motility on poly-L-lysine substrate with 1.00mg/ml, rat hippocampal neuron culture, DIV4-7, acquisition rate =1f/s, play rate 100 fr/s, bar 10μm

MovieS4. Increased filopodia motility and length in the presence of 2.5μM blebbistatin, rat hippocampal neuron culture, DIV4-7, acquisition rate =1f/s, play rate 100 fr/s, bar 10μm

Chapter 3

FiloTracker – Software for Tracking Dynamic Subcellular Protrusions[3].

3.1 Introduction

In order to measure filopodia lengths from phase microscopy filopodia motility assays, a simple yet accurate and efficient software was needed. Automated image data processing is a requirement for unbiased image data analysis and is popular in many industries and leading research institutions. Proprietary and open software packages are increasingly common, however there was no software available that could reliably track thin subcellular protrusions on a neuronal dendrite.

Thus, we decided to design such software to shorten the time needed to track individual filopodial motility as well as eliminate human error and bias from the data analysis procedure. The Matlab prototype algorithm with simple user interface was developed. *(Figure 3.1)*

The workflow included four major steps *(Figure 3.2):* image data pre-processing: segmentation of the filopodia motility movies to yield black and white stacks of frames that can be fed into the algorithm for analysis; identification of the base and tip of the filopodia on the dendrite using user input; tracking of the filopodium shape and measurement of the filopodium length in every frame of the movie; output the file with length measurements as a .csv or .mat file for further quantitative analysis.

Additional steps were taken to test and validate the software against the computer-generated black-white images without noise as well as hand-tracked data. Parameter screening was performed to identify the best parameters for the filopodium dynamics.

[3] This work was done in collaboration with Dr. Igor Novak.

The resulting Matlab prototype code takes 1.5 min to track a single filopodium from 1000 frame movie compared to 2hrs of hand-tracking. The procedure was further optimized to analyze all identified filopodia in the frame in a single run time using parallel programming cores. Thus, FiloTracker software facilitated data image processing and significantly accelerated data extraction for further analysis of filopodia dynamics.

3.2 Description of the FiloTracker algorithm

We developed and implemented in Matlab an algorithm for tracking dendritic filopodial dynamics. The algorithm, which we call FiloTracker, can analyze a binary stack derived from DIC, phase contrast or fluorescence movies by automatically skeletonizing the filopodia into connected linear segments.

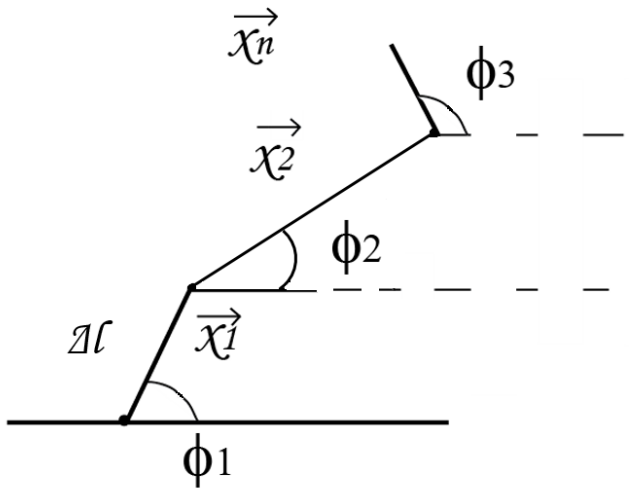

To produce a binary image for the algorithm two feature extraction steps were performed: edge-detection and foreground-background segmentation. At that point all the images in the stack are binary and ready for skeletonizing and tracking. FiloTracker then implements the annealed particle filtering algorithm originally developed to analyze articulated body motion in the computer vision field (Isard and Blake, 1998); the main idea is to compute the best configuration (the set of parameters that describes the object shape) as a statistical average over an ensemble of possible configurations, rather than searching for the best parameter set through some minimization procedure. Each filopodium in our method is represented by its skeleton, which is a non-self-intersecting polygonal chain with a fixed number, n, of segments of equal lengths. The skeleton is parametrized using the angles between the segments and the length of the segments (figure below).

Δl – is the length of each segment,

ϕ_i - are orientation angles of segments.

The default value of n is 4, but it may be adjusted by the user to achieve better results for extremely curvy filopodia. To initiate the skeletonization process, the user chooses filopodia in the first image of the stack by clicking pixel pairs at the base and tip of each filopodium. For each consecutive image, the algorithm first generates a sufficiently large random set of possible configurations in the vicinity of the skeleton from the previous frame; the only required constraint is that the base of all configurations is fixed. We then use pixel values from the new image to compute weights for these configurations, where weight is a measure of how closely a configuration lines up with the pixels in the new frame. For the j-th configuration the weight is calculated from *Eq.8*

$$w_j = \frac{1}{z} e^{-E_j}, \qquad (8),$$

where $z = \sum_{j=1}^{N} e^{-E^j}$ is a normalization parameter, *N* is the number of skeletons. Another parameter E_j in *Eq8* is the "strain energy" associated with the j-th configuration, which tends to be smaller if a configuration lines up better with the pixels Ω in the new frame. This energy is calculated as

$$E = k_1 \sum d_i^2 - k_2 \Delta l + k_3 \sum (\phi_i - \phi_{i+1})^2, \quad (9)$$

$$d_i = \min_{\vec{\xi} \in \Omega} \left\| \overrightarrow{x_i} - \vec{\xi} \right\|,$$

Finally, in the new frame, the algorithm computes the configuration for the new skeleton as a weighted vector sum of all configurations from the original set. Full details on the mathematics behind the algorithm can be found in (Isard and Blake, 1998). Once the best fit filopodium is found on each consecutive frame, the length measurements are recorded into the output file. We found that image acquisition at 1 frame per second was sufficiently fast for highly precise tracking.

3.3 Algorithm validation

We validated our model with two independent test procedures. For the first, we generated a spatial simulation of a model filopodium that randomly grows, retracts and flails. The filopodium was simulated as a non-self-intersecting polygonal chain with a given bending modulus and given polymerization /depolymerization rates. Random force was applied at each node of the chain to generate realistic filopodia dynamics. Then, we used FiloTracker to measure the filopodium length. We compared the exact length values to lengths from the FiloTracker output and evaluated algorithm's performance *(Figure3.3).* In the second validation we tracked filopodia by hand and compared hand-tracked filopodia length measurements to FiloTracker output *(Figure 3.4).*

Code available publicly at: https://github.com/olemarch/FiloTracker

Figures

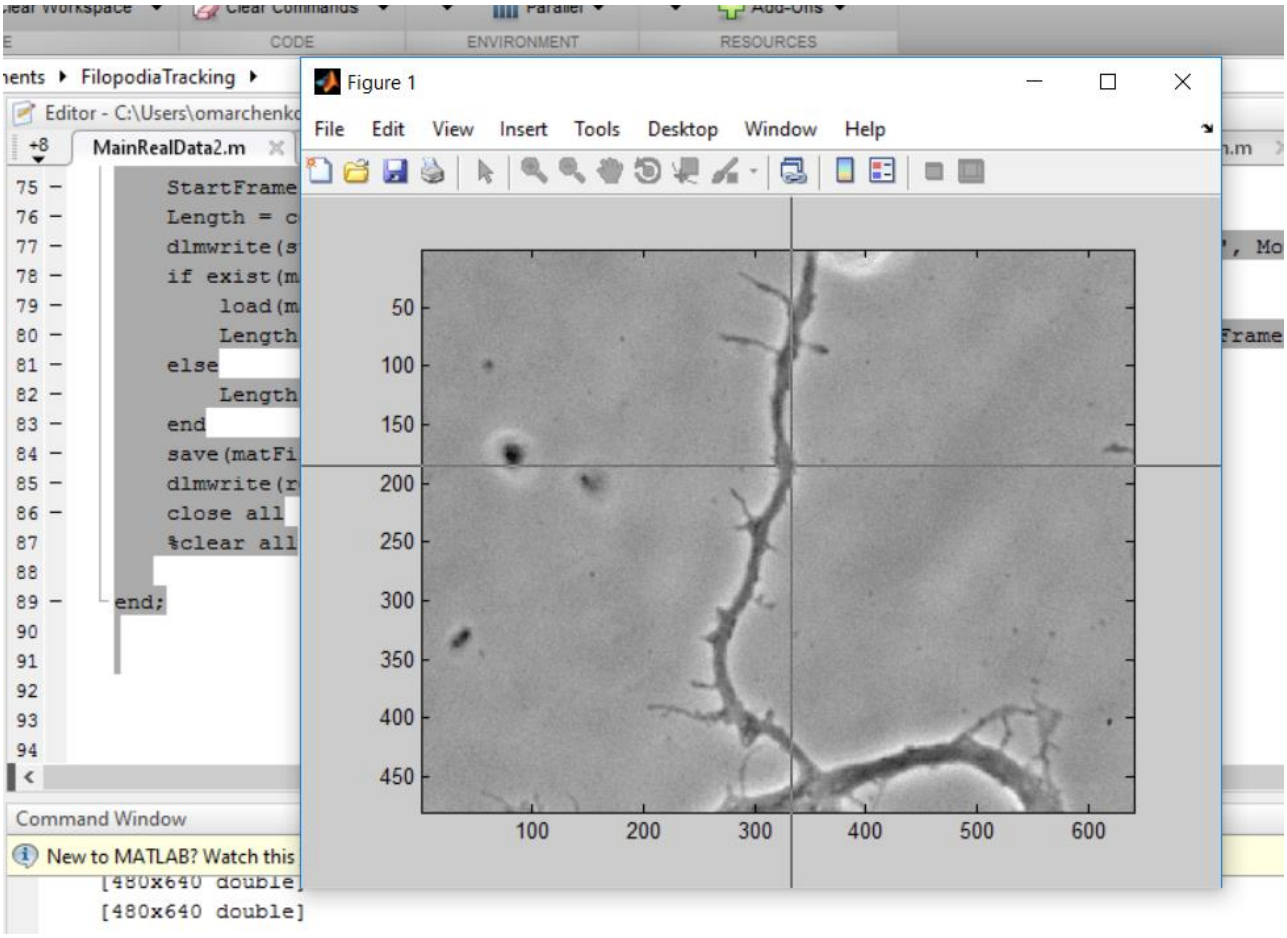

Figure 3.1 Screenshot of the FiloTracker software user input window with greyscale image, on which filopodia are selected for the analysis.

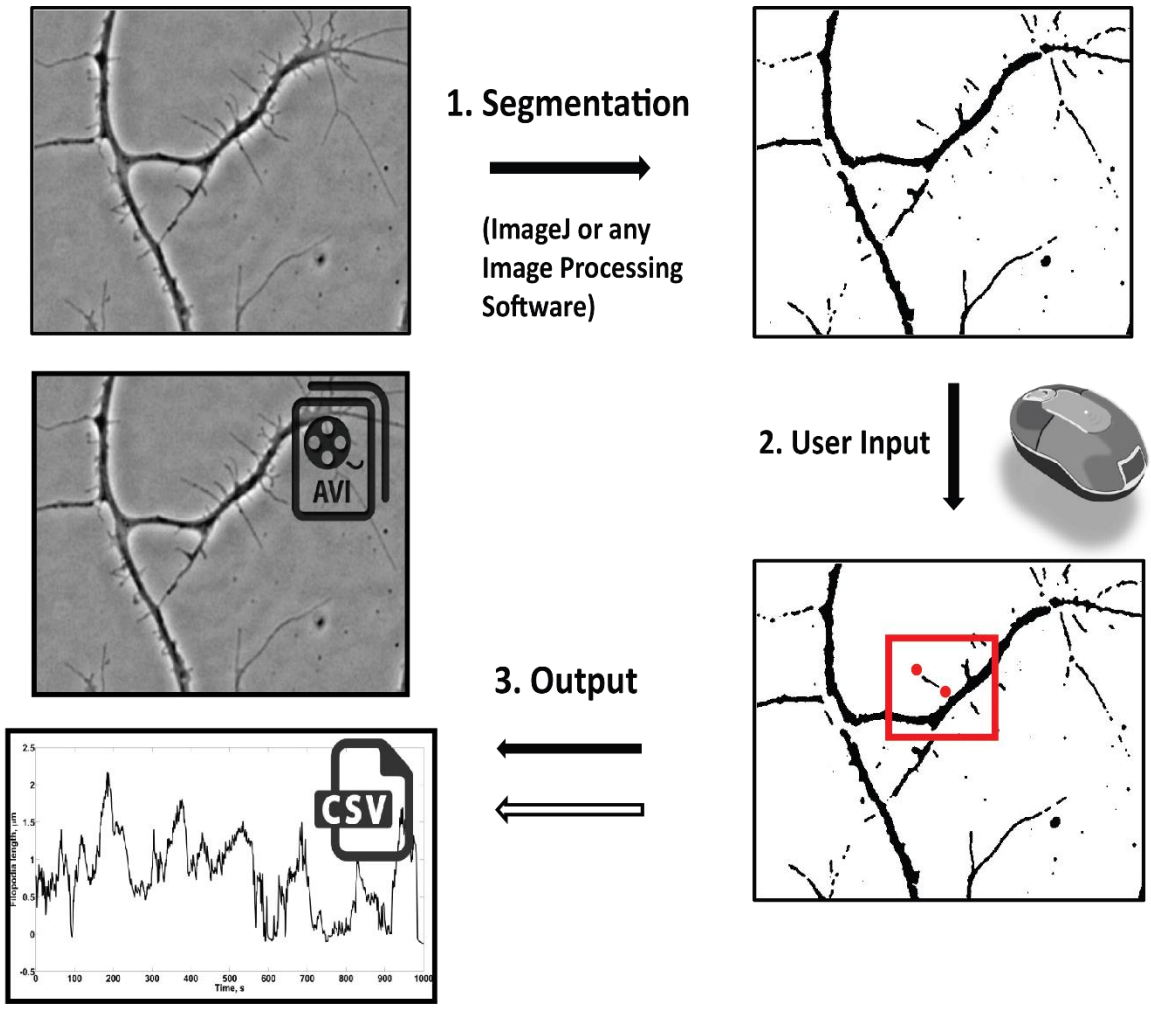

Figure 3.2. FiloTracker Workflow. We start from a phase microscopy greyscale tiff movies that capture dendrites with any motile filopodia. Next, the greyscale movie is thresholded and converted to binary such that filopodia outlines can be easily recognized and the background is clear of debree. The filopodia are the marked by user with the tip and the base on the first frame and the software then determines the filopodia outline and records its lengths measurements in a csv file. The filopodia outlines are drawn on

the original greyscale frames for accuracy comparison and output as avi file

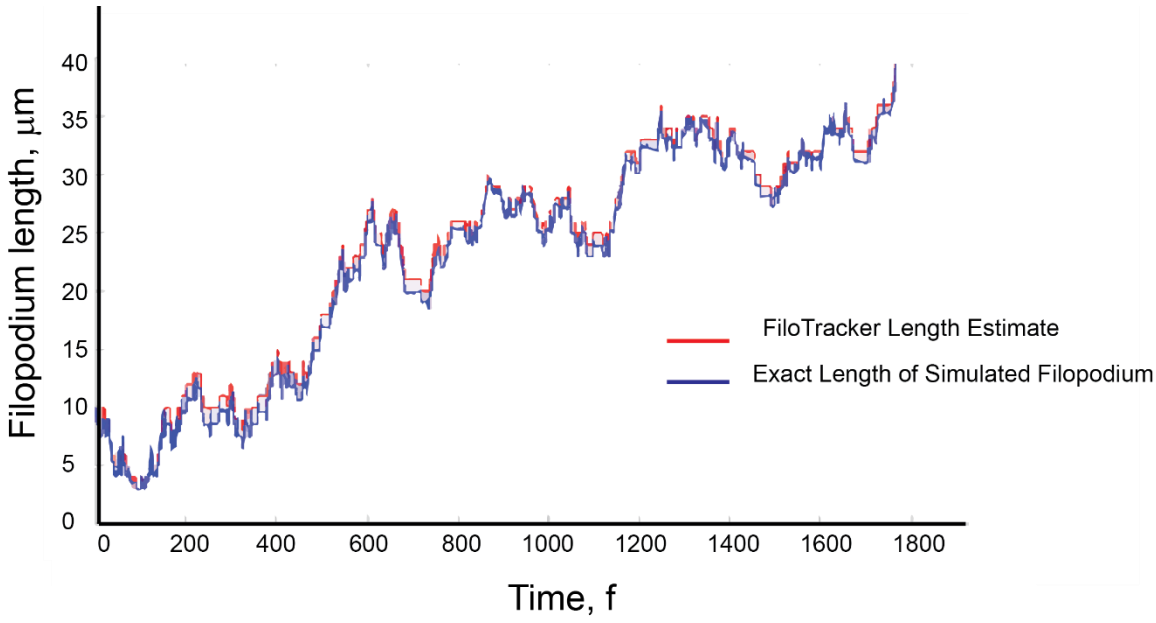

Figure 3.3 Filo tracker algorithm (red line) length measurements closely follow computer-generated binary image of filopodium dynamics simulation (blue line) with standard error E=0.88%. Tracing parameters used to obtain the fit: ΔL = 8, $\Delta\phi$ = 0.2, k1 = 3, k2 = 2, k3 = 3

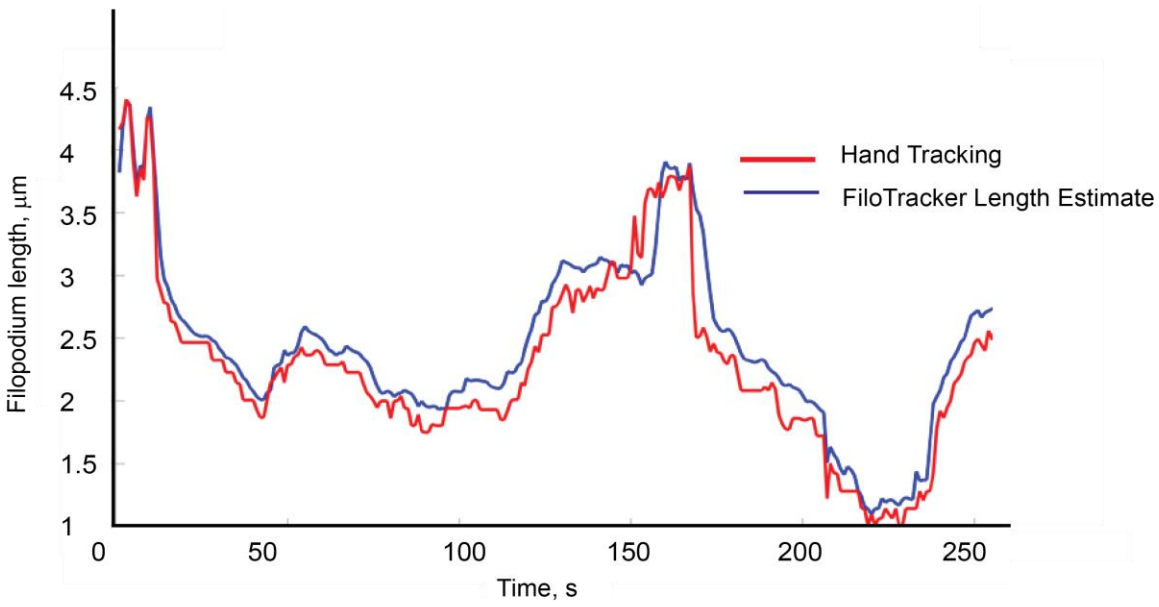

Figure 3.4 FiloTracker algorithm (blue line) length measurements output matches hand tracked filopodium lengths from live phase-contrast microscopy recording (blue line) with standard error E = 8.7%. Tracing parameters used to obtain the fit: ΔL = 5, $\Delta\phi$ = 0.3, k1 = 2, k2 = 2, k3 = 1

Bibliography

Isard M, Blake A. 1998. Conditional density propagation for visual tracking. *International Journal of Computer Vision* 29: 4

Norstrom MF, Smithback PA, Rock RS. 2010. Unconventional processive mechanics of non-muscle myosin IIB. *J Biol Chem* 285: 26326

Chapter 4

Dendritic Spine Morphogenesis in Chromosome 15q11-q13.1 Deletion Syndrome (AS) and Chromosome 15q11-q13.1 Duplication Syndrome (Dup15q) [4]

4.1 Introduction

The study of human neurodevelopment is important for understanding brain evolution and diseases, but is difficult due to limitations of experimental approaches. New methods to model human neural development and its disorders were introduced with the advent of stem cell technologies. Specifically, recent technological developments in induced pluripotent stem cells (iPSCs) and genome editing opened a unique avenue to compare patient-derived and artificially generated genotypes, opening new questions on genotype and origin of neurodevelopmental disorders in human brain.

1 in 2500 and 1 in 68 are diagnosed in Intellectual Disability (ID) and Autism Spectrum Disorders (ASD), respectively(Maulik et al. 2011). Variations in ASD clinical presentation, onset and progression are very high, and cases of ASD with a known genetic cause constitute only 59% of all cases *(Figure 4.1A)* (Vissers et al. 2015; Gaugler et al. 2014). Because ASD is comorbid with 30-70% of ID and 25% of epilepsy(Gaugler et al. 2014)(Vissers et al. 2015), syndromic ASD is a very relevant problem in the healthcare. Furthermore, intellectual disability and developmental conditions often go hand in hand, with total numbers reaching almost 2 mln adult people in the United States alone *(Figure 4.1B).* The most common developmental disorders that have high prevalence of autistic symptoms and intellectual disability include Fragile X Syndrome, Rett Syndrome, Dup15q and Angelman Syndromes, which have well documented genetic etiology. In an effort to understand ASD and intellectual disability, animal and human iPSCs models of the syndromes listed above have been developed. Successful projects that use hiPSC models apply a variety of

[4] This work was done in collaboration with Dr. Levine and Dr. Chamberlain's labs. Levine's lab supplied iPSCs derived cultures for morphology analysis in Figure 4.6 and 4.7, Chamberlain lab provided training and iPSC patient-specific cell lines for neurodifferentiation and filopodial data in Figure 4.7.

techniques from electrophysiology to genome wide sequencing. (Germain et al. 2014; Espuny-Camacho et al. 2013; Mariani et al. 2015). In this chapter, we are going to focus on dendritic spine development in Dup15q and Angelman Syndrome through collaboration with Dr. Chamberlain and Dr. Levine.

Dup15q and Angelman Syndromes are congenital neurodevelopmental conditions that arise from duplications and deletions respectively in q11-13 region of the chromosome 15, have a frequency from approximately 1/15000 to 1/30000 live births, and constitute 1-3% (Ardhanareeswaran et al. 2015) of ASD cases. Because the genes in the 15q11-13 region are regulated by genomic imprinting, the functional proteins are translated only from one parental allele. There are many variations of the deletion and duplication locations on chromosome 15q11-13 due to DNA repeat positions on the breakpoints B1-B5 *(Figure 4.2*)(Kalsner & Chamberlain 2015).

Deletions and duplications in this region result in similar clinical presentation. Angelman Syndrome is characterized by developmental delay, mental and motor disability, absent speech with comprehension exceeding expressive communication and epilepsy (80-95% of cases (Laan et al. 1999))(Kalsner & Chamberlain 2015). On the other hand, Dup15q Syndrome patients have developmental delay, intellectual disability, seizures and central hypotonia. Verbal skills are often limited and expressive language is absent.

The common gene between the two disorders is UBE3A (Ubiquitin Protein Ligase E3A), whose deletion or duplication contributes significantly to the phenotypes by mechanisms that are not yet fully understood. Mouse models of AS exhibits deficits in LTP and inhibitory calcium/calmodulin dependent protein kinase phosphorylation(Pi et al. 2010; Pignatelli et al. 2014; Kim et al. 2016).

Currently, there is no well-accepted animal model for Dup15q Syndrome. The mouse model with 6.3Mb duplication of the conserved region on parental chromosome 7 has presented with poor social interaction, and symptoms of anxiety but no seizures, hypotonia or absence of vocalization (Nakatani et al. 2009), Other genes that may contribute to the syndromic phenotype are CYFIP1, HERC2, GABRB3, GABRA5 and GABRG3, but their functional roles are to be determined.

Given that there are clear effects of UBE3A shortage or excess on synapse function and development, it is expected that there should be a neuronal phenotype associated with them. In this chapter, I present results on the neurodevelopment of Dup15q and Angelman patient iPSC-derived neurons.

4.2 Results

4.2.1 Process Arborization is Increased in Dup15q and Decreased in Angelman Patient iPSC-derived Neurons at 28 weeks

To study neuron morphology we used Dup15q iPSC lines (Rx68i and Dup1-8) generated previously (Germain et al. 2014) and Angleman patient specific Rx33i iPSC cell line with 2 base pair deletion in UBE3A *(Figure 4.2)*. Two neurotypical individuals were used as controls (564-2 and MCH2-10). Neuron tissue culture was generated using the embryoid body (EB) method *(Figure 4.3B)*. After 196 days of differentiation *in vitro*, the neurons were transfected with volumetric marker mCherry and imaged using a semi-automated confocal imaging routine*(Figure 4.4)*. We randomly selected 22 neurons for each line of iPSC-derived neuronal cultures from four independent experiments. Representative images showed that neurons from the two normal controls (564-2 and MCH2-10) had more extensive and elaborate neuronal processes than neurons from the Angelman patient with deletion (Rx33i) *(Figure 4.5A)*, observation that was supported by Sholl Analysis *(Figure 4.5B)*. The morphology of these neurons was traced and analyzed by using FIJI ImageJ2 with the Sholl plugin. The average total neurite length and the average number of primary branches were significantly reduced in iPSC-derived neurons from Rx33i, compared to the situations in 564-2 and MCH2-10 (n = 22 neurons from four independent experiments).

4.2.2. Dendritic spine density is increased in Dup15q and decreased in Angelman patient iPSC-derived neurons compared to controls at 28 weeks

Since cell body and dendrite complexity were increased in the Dup15q neurons and decreased in AS neurons, we wondered whether spine density and size might be affected. Thus, we analyzed dendritic protrusions density at 28 weeks and identified a significant increase in spine density in Dup15q compared to control and AS neurons*(Figure 4.6A,B)*.

Morphology and spine density findings in AS neurons correlate with the electrophysiological deficits. Neurons derived from AS patients were comparable to controls at 3-10 weeks, but showed developmental delayes that were generally apparent by 6-8 weeks in culture. Specifically, AS-derived neurons showed a significantly more depolarized resting membrane potential, spontaneous excitatory synaptic activity, impaired development of mature action potential firing and spontaneous and deficits in synaptic long term potential. Importantly, these differences were maintained as late as 20 weeks in culture. These genotypic differences can be directly attributed to loss of UBE3A because these differences could be mimicked in control neurons by knocking out UBE3A in an isogenic CRISPR-Cas9 gene-edited cell line or knocking down UBE3A with antisense oligonucleotides against UBE3A, and the phenotype could be rescued in AS neurons by pharmacologically increasing paternal UBE3A expression.

4.2.3. Dendritic filopodia density and motility is increased in Dup15q Syndrome neurons at 7 weeks

The increased dendritic spine density in Dup15q neurons may correspond to the increased dendritic filopodia density or reduced pruning during early neurodevelopment (7-12 weeks). The Dup15q and control iPSCs were cultured using monolayer on MEF feeder and the derived neural progenitors were plated onto laminin at week 5*(Figure 4.3A)*. Imaging was performed during week 7, when dendrites and axons were differentiated sufficiently and dendrites were covered with dendritic filopodia.

Filopodial density was significantly greater in Dup15q cell lines compared to control (P=0.001, t-test, N=871, n(cells) = 31). *(Figure 4.7A,B).* The filopodia in both cell groups were dynamic and continuously making connections with the neighboring processes *(Movies 1-3)*. To learn more about this phenotype we used the Filotracker software described in Chapter 3 to identify any differences in protrusion and retraction rates, as well as the overall motility fraction. Dendritic filopodia from Dup15q lines had 1.5 times faster protrusion *(Figure 4.7C)* and 2 times faster retraction rates compared to filopodia from control line*(Figure 4.7D)*. Interestingly, Dup15q filopodia had overall faster retraction events compared to their protrusion rate, while control line filopodia protruded and retracted in symmetrical fashion. Motility analysis at later timepoints 10 and 12 weeks is needed to confirm the observed phenotype.

4.3 Discussion

Dup15q and Angelman Syndromes are debilitating neurodevelopmental conditions caused by duplication or deletion respectively within q11.2-13.1 region on chromosome 15. While the symptoms are similar, the functional causes for the dysfunctions in the central nervous system associated with the disorders remains unclear. Given the evidence on the regulatory function of UBE3A in the synapse development and maturation, we hypothesized that the morphology of dendritic spine and neuron morphology overall has differences.

To study the neuron morphology in Dup15q and Angelman Syndrome we used iPSCs-derived neurons carrying mutations from Angelman and Dup15q patient cell lines, previously characterized (Germain et al. 2014; Chamberlain et al. 2010). The morphology assessment was performed at 28 week old cultures. We were able to show that the neuronal process arborization is reduced in AS neurons and increased in Dup15q and the dendritic protrusion density is reduced in AS and increased in Dup15q neurons when compared to neurotypical controls. Reduced dendritic arborizations and especially reduced length of terminal processes

has been associated with mental retardation(Kaufmann & Moser 2000) presumably due to the fact that shortened dendrites and axons lead to fewer connection and smaller intercellular networks and thus a reduced rate of maturation and compromised functionality. Indeed, an electrophysiological profile of AS cells also reveals evidence for delayed maturation in AS cells with increased number of immature action potential propagation compared to control(Fink et al, manuscript under review). Increased arborization of the processes has also been associated with neurodevelopmental conditions(Kaufmann & Moser 2000). Electrophysiology data showed increased spontaneous action potential firing and excitatory synaptic activity in Dup15q-derived neurons (under review).

At 7 weeks, dendritic filopodia density and motility was increased in Dup15q compared to control cells. These results suggest that the differences between control and patient groups arise very early in neurodevelopment and are directly related to the Dup15q phenotype observed at 28 weeks. In particular, the increased filopodia motility in Dup15q Syndrome cell lines promotes axon-dendrite connections enhancing both filopodia and dendritic spine structures. The biochemical pathways affected by Dup15q Syndrome that promote filopodia motility and number include CYFIP1(Pathania et al. 2014) and UBE3A. Rescue experiments with oligonucleotide treatments that reduce levels of CYFIP1 and UBE3A to control in Dup15q cell lines are needed to confirm the effect on the dendritic filopodia motility and dendritic spine density. If confirmed, differences in filopodia motility can be used to significantly shorten the time needed for drug screening experiments.

While more evidence is needed to draw definitive conclusions about the morphological differences between control, Dup15q and AS patient-derived neurons, my data indicates that iPSCs-derived neurons can be used to study and compare cellular phenotypes, track neurodevelopment of individual cell lines, design and test new treatment approaches and their application at different neurodevelopmental time points.

Image data acquisition methods described in this study needs to be improved to yield more accurate neuronal morphology identification. In comparison to neuronal soma dendritic branches can extend through large tissue volumes and require high-resolution imaging protocols for correct reconstruction. Evaluation

of synapse maturation in the cell lines of interest has not been completed, and it is unknown how the neuron development in culture correlates with the neuron development in utero. Immunostaining and co-localization of presynaptic and post-synaptic proteins such as PSD-95 and Synapsin I with the dendrite marker (MAP2) is needed to support dendritic protrusion density analysis. Finally, rescue of phenotype in the knock-out Dup15q lines and AS patient line with reengineered functional UBE3A gene is required for definitive results.

4.4 Materials and Methods

Patients and Cell lines

Neurons derived from iPSC lines from two Dup15q Syndrome patients were used in the study: Idic(15) fibroblasts (catalog ID: GM07992) were obtained from the Coriell Institute for Medical Research Cell Repository (Dup1-8). Idic(15) umbilical cord blood cells were donated by the patient's family through the Dup15q Alliance and were exempted from consideration as human subject research by the University of Connecticut Health Center Institutional Review Board (IRB)(Germain et al. 2014).

Neurons derived from uPSC line from Angelman Syndrome patient harbors a 2 base pair deletion in UBE3A gene and was obtained from Dr. Levine's lab (Rx33i)

Control cell lines were derived from normal male individuals in Dr. Levine's lab (MCH2-8, 562-4)

Neuronal differentiation EB body protocol

iPSC-derived neural progenitors were generated by embryoid body (EB)-based protocol (Chamberlain et al, 2010) with minor modifications. Briefly, iPSCs were co-cultured with Mytomycin-C-treated mouse embryonic fibroblasts (Millipore) in standard human embryonic stem cell medium consisting of DMEM-F12 (Life Technologies), 20% knockout serum replacer, 0.1 mM NEAA, 1 mM L-glutamine, 0.1 mM 2-

mercaptoethanol, and 10 ng/mL bFGF, replaced daily. Cells were maintained in a humidified incubator at 37°C with 5% CO2 and passaged once per week with the aid of a 28-gauge needle. Chamberlain et al, 2010. Briefly, iPSCs were manually detached and grown in suspension to form embryoid-like aggregates. The following day, cell aggregates were cultured in neural induction media (DMEM/F12, 1X N2 Supplement, 0.1 mM NEAA, 2 μg/mL heparin, and 10 ng/mL bFGF). DMH1 (Millipore) and SB431542 (Stemgent) were added to the media at a final concentration of 2 μM on day 1 and day 4 of neural induction to enhance the formation of columnar cells 20. The cell aggregates were then plated onto laminin-coated plates. Within a week, neural precursor cells were manually dissected and grown in suspension, forming neurospheres. After 6 days, the neurospheres were manually dissociated and plated in neural differentiation medium (Neurobasal, 1X B-27 Supplement, 0.1 mM NEAA, 2 mM L-glutamine and 1 μg/mL laminin) onto polyornithine/laminin-coated glass coverslips. ROCK inhibitor Y-27632 (10 μM; Wako) was added to the neural differentiation media during initial plating to promote cell attachment. After 2 days, 1 μM cAMP (Sigma), 0.2 mM L-ascorbic acid (Sigma), 20 ng/ml GDNF (Peprotech), and 20 ng/ml BDNF (Peprotech) were added to the media that were replaced 2-3 times per week. All experiments were conducted on neural cultures that were 28-35 weeks.

Monolayer culture for dendritic filopodia motility and density analysis.

Patient (Dup1-8 and Rx68i) and control (MCH2-10) iPSC colonies were prepared and neurodifferentiated as described previously (Germain et al. 2014). After three weeks of neural differentiation, neural progenitors were plated on poly-ornithine/laminin coated substrates in neural differentiation medium consisting of Neurobasal Medium, B-27 supplement, nonessential amino acids, and L-glutamine (all Gibco products through Life Technologies, Grand Island, NY, USA) supplemented with 1 μM ascorbic acid, 200 μM cyclic adenosine monophosphate (cAMP), 10 ng/mL brain-derived neurotrophic factor (BDNF, Peprotech, Rocky Hill, NJ, USA), and 10 ng/mL glial-derived neurotrophic factor (GDNF, Peprotech, Rocky Hill, NJ, USA). Imaging was conducted on neural cultures that were 7, weeks old.

Transfection

Neurons were transfected with the mCherry construct using Lipofectamine3000 (Thermofisher, Waltham, MA) at 28 weeks to image neuron morphology and dendritic protrusions as described in the company protocol and previous studies(Tatavarty et al. 2012)

Dendritic protrusion densities.

Neurons were transfected with mCherry plasmid (gift from Dr. Ji Yu). 13mm coverslips were placed in imaging chamber RC-6G (Harvard Apparatus, Holliston, MA), bathed in Hibernate E Low Fluorescense medium (BrainBits, Springfield, IL) and fluorescent neurons were imaged at RT collecting z-stack planes (15μm depth with interval 0.4μm). All images were captured using 63xOil objective with 1.25NA on LSM 780 confocal microscope (Carl Zeiss, Germany) with LSM software at the same imaging settings (pinhole, laser intensity) per experiment.

Collapsed *z*-stacks were analyzed using FIJI ImageJ: Each protrusion ≤4 μm was considered a spine and counted. Individual planes were evaluated to detect protrusions extending perpendicular to the collapsed *z*-stack. The analysis was restricted to 50 μm from the soma, due to the variations in spine densities at larger distances. Total spine number for each segment was normalized to the length of the dendritic segment to generate density values. Dendritic segments without spines were not counted, and all scoring was conducted by a single blinded counter.

A student's t-test was used for statistical analysis.

Sholl Analysis.

Neurons were transfected with mCherry plasmid (gift from Dr. Ji Yu). Neurons with clear morphology were used for analysis. Binary images of neuron morphology were automatically generated from collapsed z-stacks of transfected neurons. Standard Sholl analysis was performed on binary images of individual

neurons at 28-30 weeks in culture using FIJI software, i.e. the. number of branches intersecting with concentric circles centered on the soma were quantified. A student's t-test was used for statistical analysis.

Dendritic filopodia imaging.

Dendritic filopodia imaging was performed with Nikon Plan NA1.25x100 objective on DIV 3-12 on Nikon diaphot 300 inverted microscope with 1f/s acquisition rate. Images were collected with back- illuminated CCD camera (CH350, Roper Scientific) driven by Metamorph image acquisition and analysis software (Metamorph, Sunnyvale, CA). Protrusion and retraction rates were calculated using the custom written FiloTracker algorithm described in Chapter 3.

A student's t-test was used for statistical analysis.

Legends to Supplemental Movies

Movie1. Filopodial motility in control cell line at 7 weeks on poly-o/laminin, acquisition rate =1f/s, play rate 100 f/s, bar 10μm

Movie2. - Filopodial motility in Dup1-8 cell line at 7 weeks on poly-o/laminin, acquisition rate =1f/s, play rate 100 f/s, bar 10μm

Movie3. Filopodial motility in Rx68i cell line at 7 weeks on poly-o/laminin, acquisition rate =1f/s, play rate 100 f/s, bar 10μm

Figures.

A

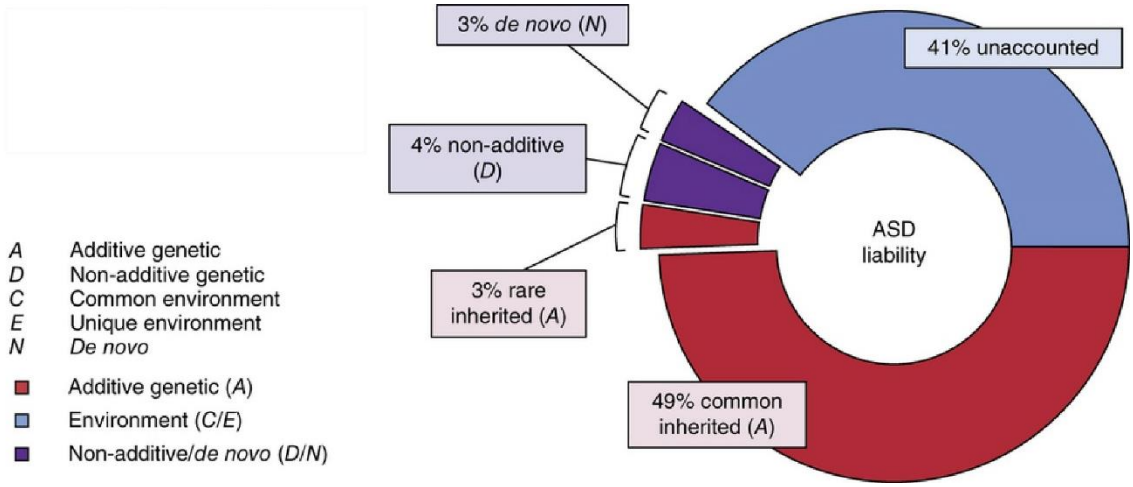
A Additive genetic
D Non-additive genetic
C Common environment
E Unique environment
N De novo
Additive genetic (A)
Environment (C/E)
Non-additive/de novo (D/N)
3% de novo (N)
4% non-additive (D)
3% rare inherited (A)
41% unaccounted
ASD liability
49% common inherited (A)

B

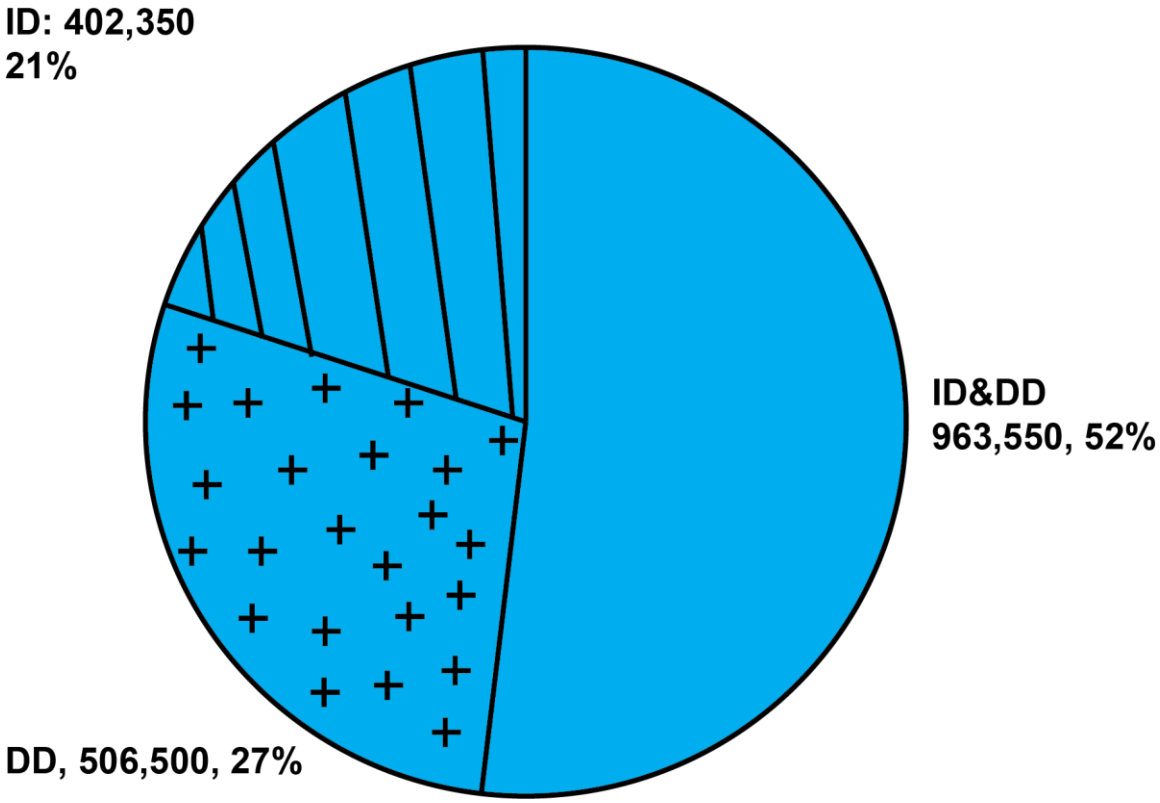
ID: 402,350
21%
ID&DD
963,550, 52%
DD, 506,500, 27%

Figure 4.1. Occurrence of Autism Spectrum Disorder (ASD) and Intellectual disability (ID) in general population

A. Studies on genetic origin of ASD (figure 1f from Gaugler et al. 2014) shows the distribution of cases in ASD among de novo(3%), non-additive(4%), rare inherited(3%), common inherited(49%) and unaccounted mutations(41%). Used with permission, Copyright©2014 by Nature Publishing Groups B. Incidence of Intellectual Disability(ID) and Developmental Disability (DD) among adults (18+) (combined data from national household survey and national data on out-of-family residential programs, children and youth are excluded). According to the studies there are an estimated 1.9 million adults, 18 years or older with either ID or DD. More than half (51.5%) of 1.9 mln are estimated to have both intellectual and developmental disabilities, while 21.5% are identified as suffering from intellectual disability, but not developmental disability, and about 27% are diagnosed with developmental disability but not intellectual disability (Figure adopted and modified from data from Center for Disease Control and Prevention CDC.gov. 2016. *Research Developmental Disabilities NCBDDD,CDC.* Available at: https://www.cdc.gov/ncbddd/developmentaldisabilities/research.html.

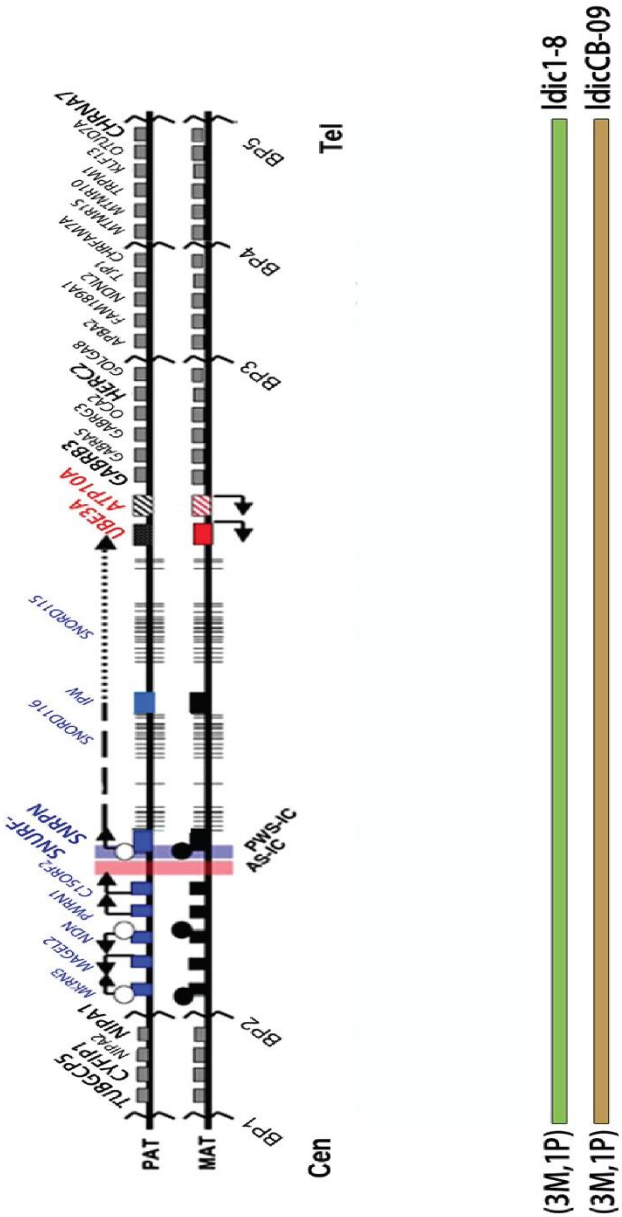

Figure 4.2 Dup15q Syndrome genetic map and cell lines. Neurons derived from iPSC lines from two patients were used in the study: Idic(15) fibroblasts (Dup1-8) with maternal duplication BP1-BP5 forming a separate mini chromosome (total 3 maternal copies and 1 paternal) and Idic(15) umbilical cord blood cells with maternal duplication forming a separate chromosome (total 3 maternal copies and 1 paternal)(Rx68i).(Figure modified and adapted from Chamberlain et al., 2010 Used with permission, Copyright©2010 Elsevier (Germain et al. 2014)).

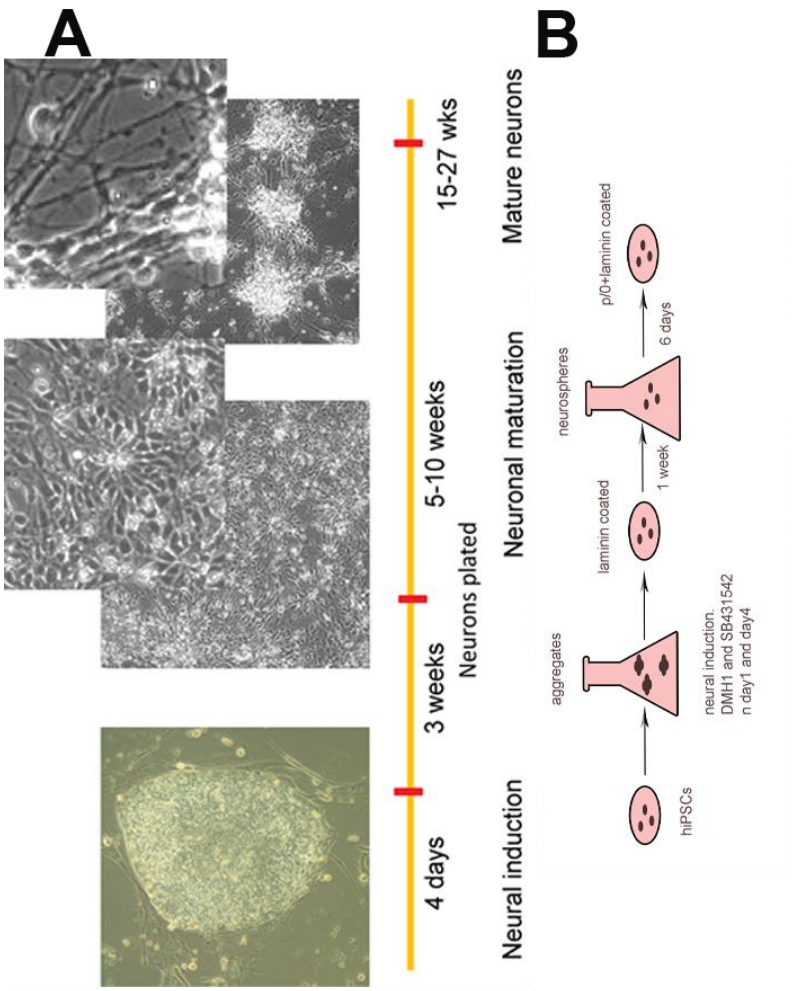

Figure 4.3 Schematized protocols of neurodifferentiation used for dendritic filopodia motility and neuron morphology analysis .A. Depiction of Monolayer protocol that was used to generate neuronal cultures for dendritic filopodia density and motility analysis at 7 weeks B. Graphics of Embryoid Body (EB) protocol that was used to generate neuronal cultures for neuron morphology, dendritic protrusion density analyses.

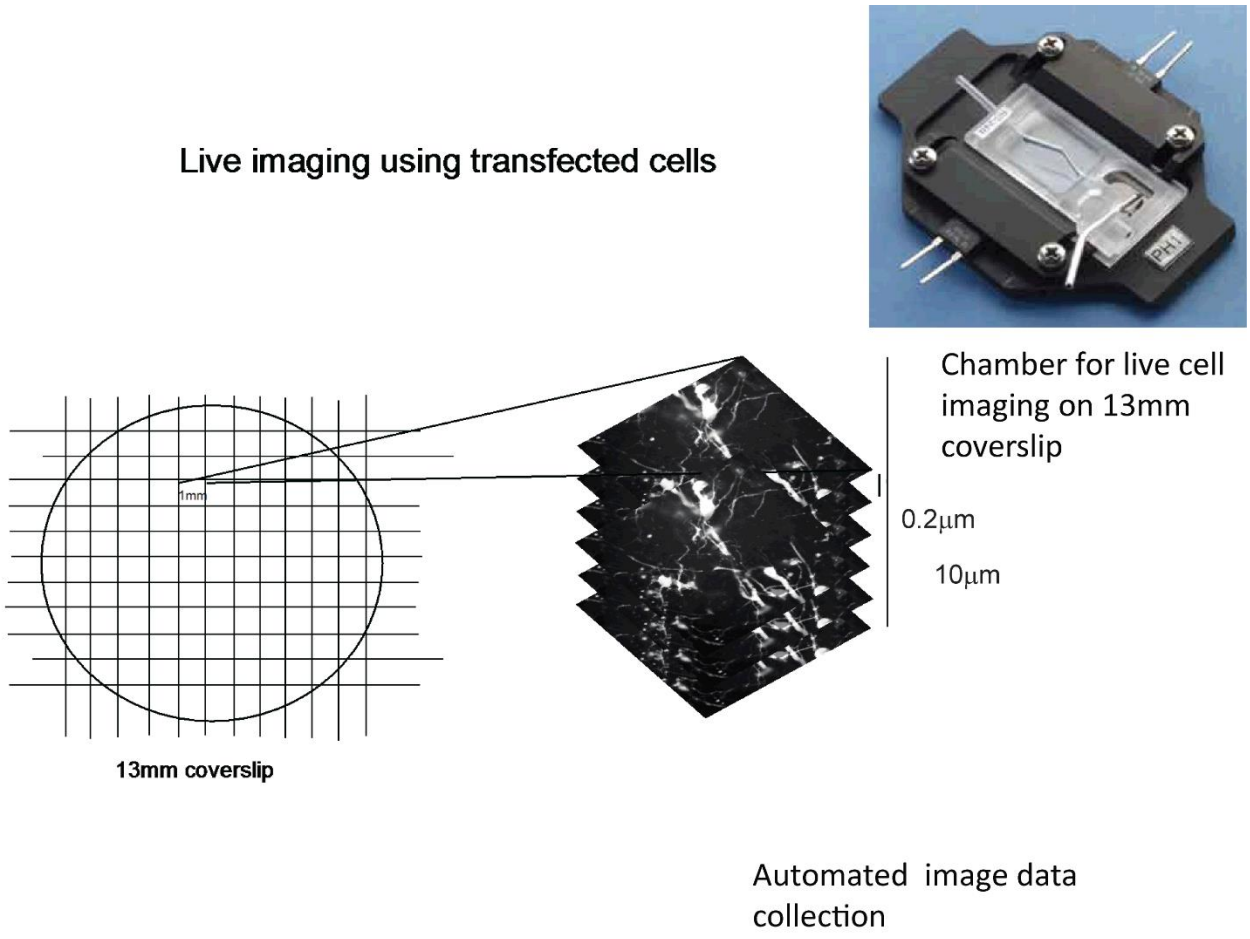

Figure 4.4 Live imaging of transfected cells for Sholl Analysis. Neurons derived from patient iPSCs via EB protocol are plated on 13mm coverslip and maintained until appropriate developmental age (25-32wks). Then they are transfected with fluorescent volumetric marker mCherry, placed in an imaging chamber bathed with Hibernate E and imaged under confocal microscope using automated imaging routine.

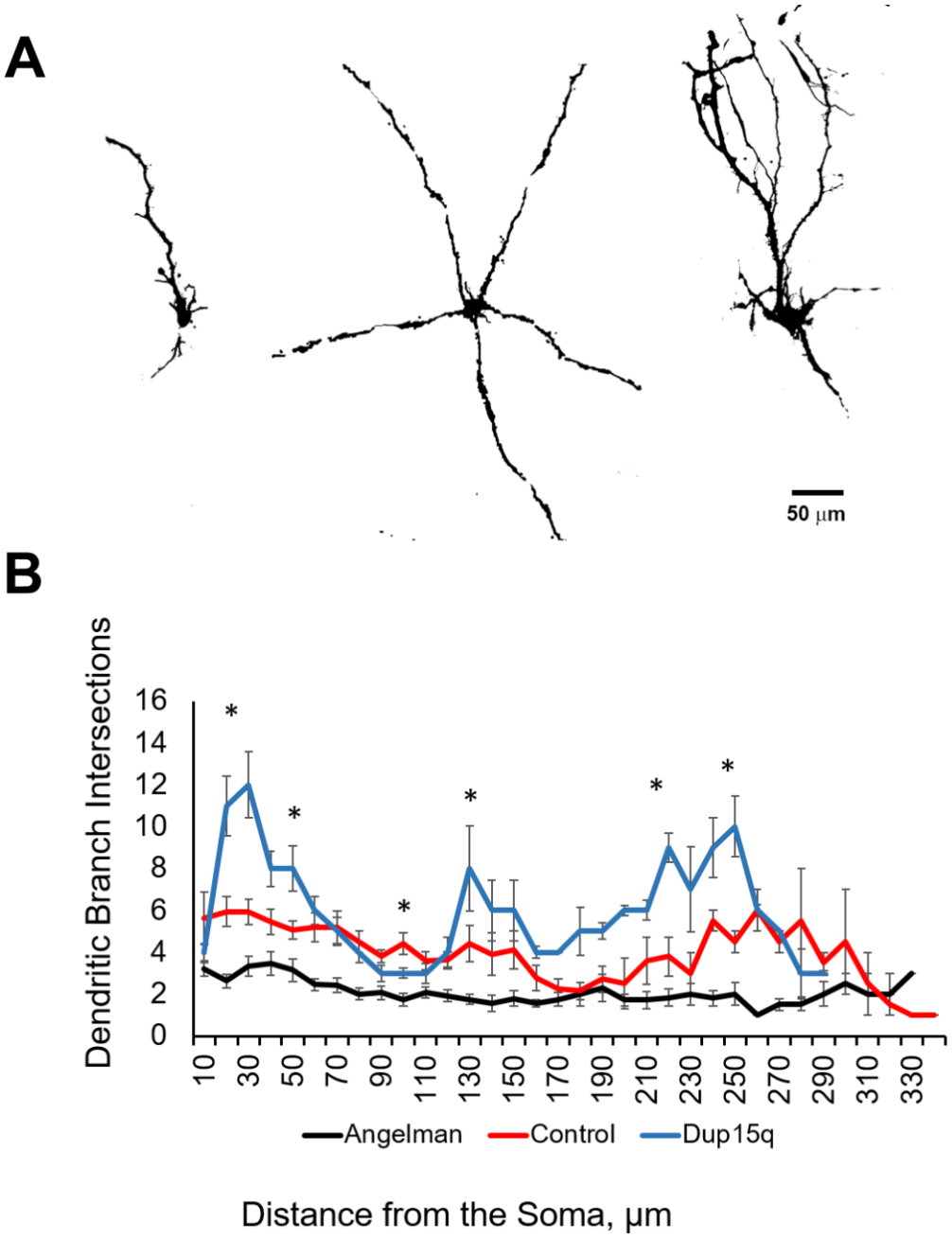

Figure 4.5 Morphology Analysis in control, Angleman and Dup15q neurons at 28 weeks. A. Representative images of in control, Angleman and Dup15q neuron morphology at 28 weeks. B. Sholl Analysis for control (N=21, coverslips=6) Angelman (N=22, coverslips=4) and Dup15q (N=33, coverslips=10) neurons at 28 weeks, (t-test, **P=0.001, ***P=0.001)

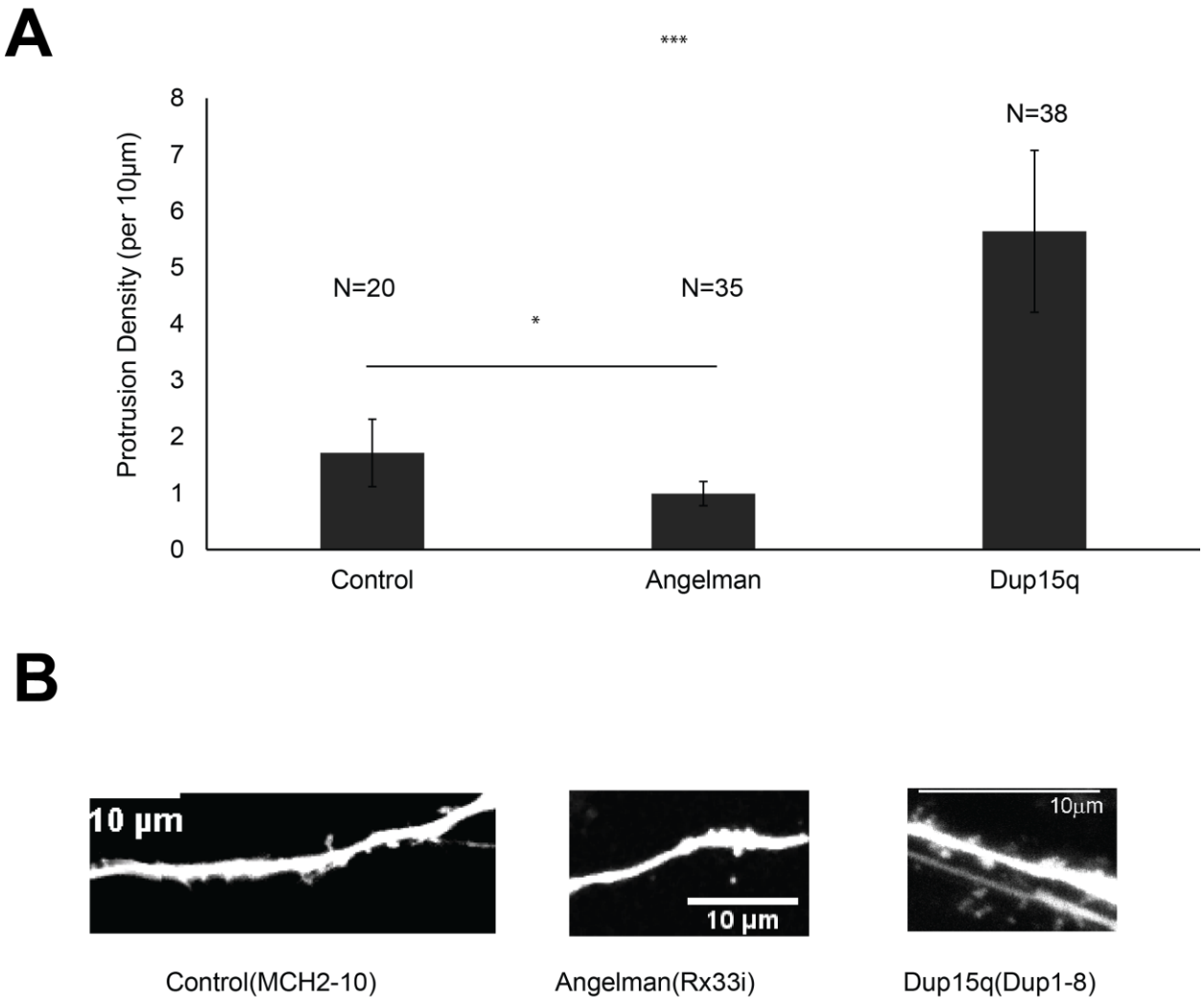

Figure 4.6 Dendritic Protrusion Density Analysis in Dup15q, Angelman and control neurons transfected with mCherry at 28 weeks. A. Quantification of protrusion density per 10um in control ($N_{dendrite}$ = 20, coverslips=5), Angelman($N_{dendrite}$ = 35, coverslips=6) and Dup15q($N_{dendrite}$ = 63, coverslips = 14. *P<0.01, ***P<0.001), B. Representative images for dendritic protrusion densities in control, Angelman and Dup15q iPSC-derived neurons.

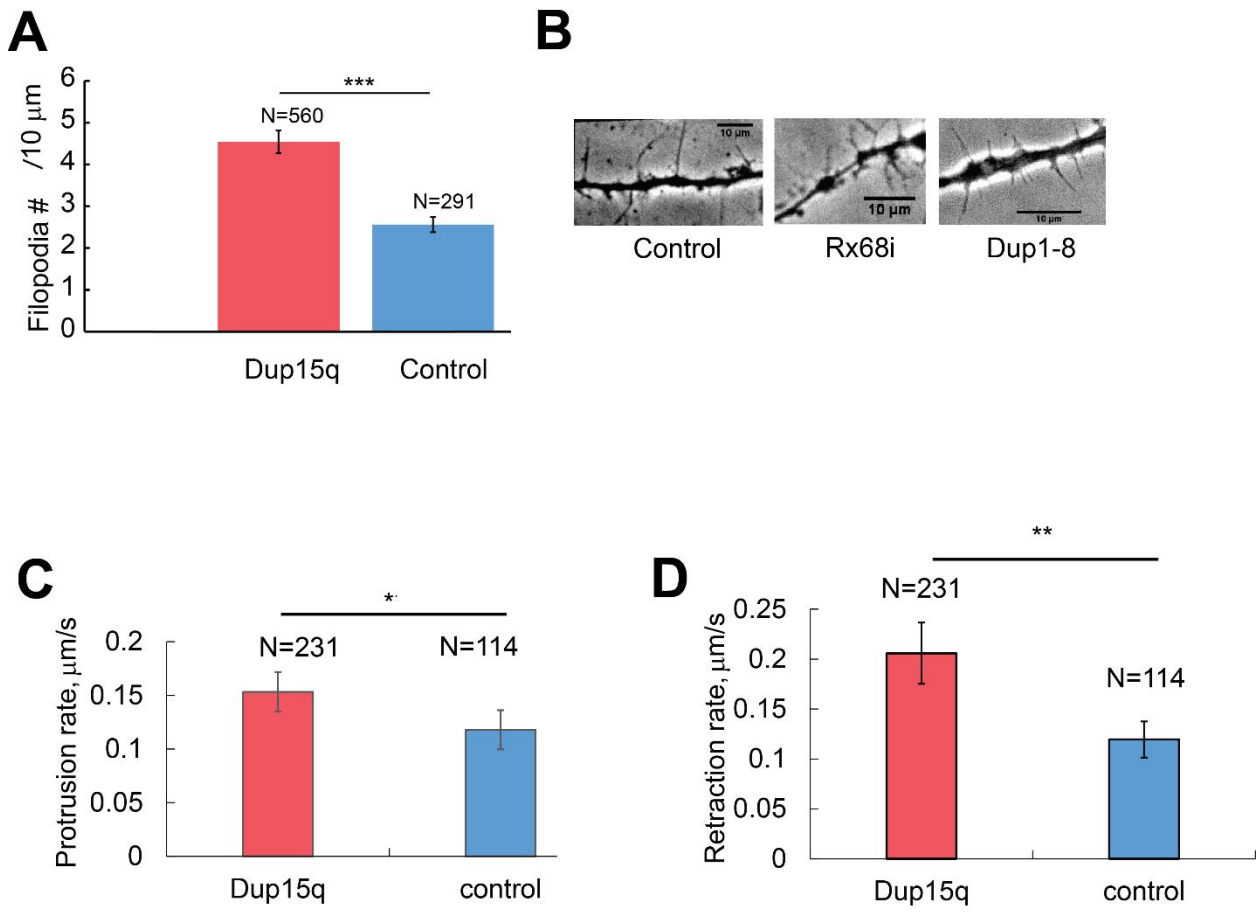

Figure 4.7 Dendritic Filopodia Density and Motility at 7 weeks in monolayer iPSC-derived neuron culture from Dup15q (Dup1-8, Rx68i) and control individuals.

A. Quantification of dendritic filopodia density per 10µm in randomly selected dendrite regions in Dup15q (Dup1-8 $N_{dendrite}$ =15, Rx68i $N_{dendrite}$=18, with N filopodia counted for each group) and control ($N_{dendrite}$=24) neurons (T-test, *** P<0.0001, SEM based on dendrite number). B. Representative dendritic segments for filopodia density in control, Rx68i and Dup1-8 neurons. C. Quantification of dendritic filopodia protrusion and retraction rates. (Dup1-8 $N_{dendrite}$ =8, Rx68i $N_{dendrite}$=6, control $N_{dendrite}$=4, *P<0.01, **P<0.001 T-test, SEM based on number of dendrites).

Bibliography

Ardhanareeswaran, K., Coppola, G. & Vaccarino, F., 2015. The Use of Stem Cells to Study Autism Spectrum Disorder. *The Yale journal of biology and medicine*, 88(1), pp.5–16.

Arellano, J.I. et al., 2007. Ultrastructure of dendritic spines: correlation between synaptic and spine morphologies. *Frontiers in neuroscience*, 1(1), pp.131–143.

Blanchoin, L. et al., 2014. Actin dynamics, architecture, and mechanics in cell motility. *Physiological reviews*, 94(1), pp.235–63.

Bourgeois, J.P. & Rakic, P., 1993. Changes of synaptic density in the primary visual cortex of the macaque monkey from fetal to adult stage. *J Neurosci*, 13(7), pp.2801–20.

Brown, S.A. et al., 2011. Virtual NEURON: A strategy for merged biochemical and electrophysiological modeling. *Journal of Computational Neuroscience*, 31(2), pp.385–400.

Caroni, P., Donato, F. & Muller, D., 2012. Structural plasticity upon learning: regulation and functions. *Nature Reviews Neuroscience*, 13(7), pp.478–490.

Chamberlain, S.J. et al., 2010. Induced pluripotent stem cell models of the genomic imprinting disorders Angelman and Prader-Willi syndromes. *Proceedings of the National Academy of Sciences of the United States of America*, 107(41), pp.17668–73.

Chazeau, A. et al., 2015. Mechanical coupling between transsynaptic N-cadherin adhesions and actin flow stabilizes dendritic spines. *Molecular Biology of the Cell*, 26, pp.859–873.

Chazeau, A. et al., 2014. Nanoscale segregation of actin nucleation and elongation factors determines dendritic spine protrusion. *The EMBO journal*, 33(23), pp.1–20.

Chazeau, A. & Giannone, G., 2016. Organization and dynamics of the actin cytoskeleton during dendritic spine morphological remodeling. *Cellular and Molecular Life Sciences*, pp.1–21.

Comery, T. a et al., 1997. Abnormal dendritic spines in fragile X knockout mice: maturation and pruning deficits. *Proceedings of the National Academy of Sciences of the United States of America*, 94(10), pp.5401–5404.

Craig, E.M. et al., 2012. Membrane tension, myosin force, and actin turnover maintain actin treadmill in the nerve growth cone. *Biophysical Journal*, 102(7), pp.1503–1513.

Cui, J. et al., 2016. Quantification of dopaminergic neuron differentiation and neurotoxicity via a genetic reporter. *Scientific Reports*, 6(April), p.25181.

Danuser, G., Allard, J. & Mogilner, A., 2013. Mathematical modeling of eukaryotic cell migration: insights beyond experiments. *Annual review of cell and developmental biology*, 29(July), pp.501–28.

Dindot, S. V. et al., 2008. The Angelman syndrome ubiquitin ligase localizes to the synapse and nucleus, and maternal deficiency results in abnormal dendritic spine morphology. *Human Molecular Genetics*, 17(1), pp.111–118.

Ditlev, J.A. et al., 2009. An open model of actin dendritic nucleation. *Biophysical Journal*, 96(9), pp.3529–3542.

Espuny-Camacho, I. et al., 2013. Pyramidal Neurons Derived from Human Pluripotent Stem Cells Integrate Efficiently into Mouse Brain Circuits In Vivo. *Neuron*, 77(3), pp.440–456.

Fiala, J.C. et al., 1998. Synaptogenesis via dendritic filopodia in developing hippocampal area CA1. *J Neurosci*, 18(21), pp.8900–8911.

Gaugler, T. et al., 2014. Most genetic risk for autism resides with common variation. *Nature genetics*, 46(8), pp.881–5.

Germain, N.D. et al., 2013. Derivation and isolation of NKX2.1-positive basal forebrain progenitors from human embryonic stem cells. *Stem cells and development*, 22(10), pp.1477–89.

Germain, N.D. et al., 2014. Gene expression analysis of human induced pluripotent stem cell-derived neurons carrying copy number variants of chromosome 15q11-q13.1. *Molecular Autism*, 5(1), p.44.

Harris, K.M., 1999. Structure, development, and plasticity of dendritic spines. *Current Opinion in Neurobiology*, 9(3), pp.343–348.

Hill, T.C. & Zito, K., 2013. LTP-Induced Long-Term Stabilization of Individual Nascent Dendritic Spines. *Journal of Neuroscience*, 33(2), pp.678–686.

Hogart, A. et al., 2010. The comorbidity of autism with the genomic disorders of chromosome 15q11.2-q13. *Neurobiology of Disease*, 38(2), pp.181–191.

Hotulainen, P. & Hoogenraad, C.C., 2010. Actin in dendritic spines: Connecting dynamics to function. *Journal of Cell Biology*, 189(4), pp.619–629.

Ivanov, A. et al., 2009. Drebrin A regulates dendritic spine plasticity and synaptic function in mature cultured hippocampal neurons. *Journal of cell science*, 122(3), pp.524–534.

Kalsner, L. & Chamberlain, S.J., 2015. P r a d e r- W i l l i , A n g e l m a n , and 15q11-q13 Duplication S y n drome s. , 62, pp.587–606.

Kaufmann, W.E. & Moser, H.W., 2000. Dendritic anomalies in disorders associated with mental retardation. *Cerebral cortex*, 10(10), pp.981–991.

Kayser, M.S., Nolt, M.J. & Dalva, M.B., 2008. EphB Receptors Couple Dendritic Filopodia Motility to Synapse Formation. *Neuron*, 59(1), pp.56–69.

Kim, H. et al., 2016. Maternal Loss of Ube3a Impairs Experience-Driven Dendritic Spine Maintenance in the Developing Visual Cortex. *Journal of Neuroscience*, 36(17), pp.4888–4894. Available at:

Korobova, F. & Svitkina, T., 2010. Molecular Architecture of Synaptic Actin Cytoskeleton in Hippocampal Neurons Reveals a Mechanism of Dendritic Spine Morphogenesis. *Molecular Biology of the Cell*, 21, pp.165–176.

Kotaleski, J.H. & Blackwell, K.T., 2010. Modelling the molecular mechanisms of synaptic plasticity using systems biology approaches. *Nature reviews. Neuroscience*, 11(4), pp.239–251.

Laan, L. a, v Haeringen, a & Brouwer, O.F., 1999. Angelman syndrome: a review of clinical and genetic aspects. *Clinical neurology and neurosurgery*, 101, pp.161–170.

Lohmann, C. & Bonhoeffer, T., 2008. A role for local calcium signaling in rapid synaptic partner selection by dendritic filopodia. *Neuron*, 59(2), pp.253–260. Available at: http://www.ncbi.nlm.nih.gov/pubmed/18667153.

Mariani, J. et al., 2015. FOXG1-Dependent Dysregulation of GABA/Glutamate Neuron Differentiation in Autism Spectrum Disorders. *Cell*, 162(2), pp.375–390.

Maulik, P.K. et al., 2011. Prevalence of intellectual disability: A meta-analysis of population-based studies. *Research in Developmental Disabilities*, 32(2), pp.419–436.

Mogilner, A. & Rubinstein, B., 2005. The Physics of Filopodial Protrusion. *Biophysical Journal*, 89(2), pp.782–795. Available at: http://www.pubmedcentral.nih.gov/articlerender.fcgi?artid=1366629&tool=pmcentrez&rendertype=abstract.

Nakatani, J. et al., 2009. Abnormal Behavior in a Chromosome- Engineered Mouse Model for Human 15q11-13 Duplication Seen in Autism. *Cell*, 137(7), pp.1235–1246.

Novak, I.L. & Slepchenko, B.M., 2014. A conservative algorithm for parabolic problems in domains with moving boundaries. *Journal of computational physics*, 270, pp.203–213. Available at: http://www.ncbi.nlm.nih.gov/pubmed/25067852.

Pankratz, M.T. et al., 2007. Directed Neural Differentiation of Human Embryonic Stem Cells via an Obligated Primitive Anterior Stage. *Stem Cells*, 25(6), pp.1511–1520. Available at:

Parent, J.M. & Anderson, S.A., 2015. Reprogramming patient-derived cells to study the epilepsies. *Nature neuroscience*, 18(3), pp.360–6. Available at:

Pathania, M. et al., 2014. The autism and schizophrenia associated gene CYFIP1 is critical for the maintenance of dendritic complexity and the stabilization of mature spines. *Translational psychiatry*, 4, p.e374.

Penzes, P. et al., 2011. review Dendritic spine pathology in neuropsychiatric disorders. *Nature Publishing Group*, 14(3), pp.285–293.

Phillips, M. & Pozzo-Miller, L., 2014. Dendritic spine dysgenesis in autism related disorders. *Neuroscience Letters*, 601, pp.30–40.

Pi, H.J. et al., 2010. CaMKII control of spine size and synaptic strength: role of phosphorylation states and nonenzymatic action. *Proceedings of the National Academy of Sciences of the United States of America*, 107(32), pp.14437–42.

Pignatelli, M. et al., 2014. Changes in mGlu5 receptor-dependent synaptic plasticity and coupling to homer proteins in the hippocampus of Ube3A hemizygous mice modeling angelman syndrome. *The Journal of neuroscience : the official journal of the Society for Neuroscience*, 34(13), pp.4558–66.

Purpura, D.P., 1974. Dendritic spine “dysgenesis” and mental retardation. *Science (New York, N.Y.)*,

186(4169), pp.1126–1128.

Rubio, M.D. et al., 2011. Cellular/Molecular Regulation of Synapse Structure and Function by Distinct Myosin II Motors. *Journal of Neuroscience*, 31(4), pp.1448–1460.

Saneyoshi, T., Fortin, D.A. & Soderling, T.R., 2010. Regulation of spine and synapse formation by activity-dependent intracellular signaling pathways. *Current Opinion in Neurobiology*, 20(1), pp.108–115.

Sun, J. et al., 2015. UBE3A Regulates Synaptic Plasticity and Learning and Memory by Controlling SK2 Channel Endocytosis. *Cell reports*, 12(3), pp.449–461.

Tashiro, A., Minden, A. & Yuste, R., 2000. Regulation of dendritic spine morphology by the Rho family of small GTPases: antagonistic roles of Rac and Rho. *Cerebral Cortex*, 10(10), pp.927–938.

Tatavarty, V., Das, S. & Yu, J., 2012. Polarization of actin cytoskeleton is reduced in dendritic protrusions during early spine development in hippocampal neuron. *Molecular Biology of the Cell*, 23(16), pp.3167–3177.

Toro, R. et al., 2010. Key role for gene dosage and synaptic homeostasis in autism spectrum disorders. *Trends in Genetics*, 26(8), pp.363–372.

Vissers, L.E.L.M., Gilissen, C. & Veltman, J.A., 2015. Genetic studies in intellectual disability and related disorders. *Nature Reviews Genetics*, 17(1), pp.9–18.

Weeber, E.J. et al., 2003. Derangements of hippocampal calcium/calmodulin-dependent protein kinase II in a mouse model for Angelman mental retardation syndrome. *The Journal of neuroscience : the official journal of the Society for Neuroscience*, 23(7), pp.2634–2644.

Yang, C. & Svitkina, T., 2011. Filopodia initiation: focus on the Arp2/3 complex and formins. *Cell adhesion & migration*, 5(5), pp.402–408.

Yashiro, K. et al., 2009. Ube3a is required for experience-dependent maturation of the neocortex. *Nature neuroscience*, 12(6), pp.777–83.

Yasuda, S. et al., 2014. Activation of Rheb, but not of mTORC1, impairs spine synapse morphogenesis in tuberous sclerosis complex. *Scientific reports*, 4, p.5155.

Yuste, R. & Denk, W., 1995. Dendritic spines as basic functional units of neuronal integration. *Nature*, 375(6533), pp.682–684.

Ziv, N.E. & Smith, S.J., 1996. Evidence for a role of dendritic filopodia in synaptogenesis and spine formation. *Neuron*, 17(1), pp.91–102.

Chapter 5

Conclusions and Future Directions: Preliminary Study of 2D Model

5.1 Proceedings from the Results of the Previous Chapters

In the previous chapters we have started an exploration of the big question: how do dendritic filopodia transform into functional dendritic spines. To address this problem we formulated three questions:

1. **How do dendritic filopodia move and maintain stability as a result of actin cytoskeleton rearrangement and myosin activity?**
2. **How do dendritic spine density and shape compare in neurodevelopmental conditions?**
3. **How does dendritic spine shape develop as a results of actin network interaction with myosin?**

The main conclusion to our first question is that dendritic filopodia movement can be modeled by an interplay of myosin contractility, actin retrograde flow and adhesion of the cell membrane to the substrate.

Briefly, our 1D Filopodium model reproduces experimental actin flow patterns, as well as the effects of varying myosin, adhesion and actin polymerization that lead to emergence of dynamic filopodia through the following mechanism. In a filopodium with a stable steady state length, the actin retrograde flow due to contraction and tension balance the polymerization rate.

The model describes the biophysical mechanisms associated with the viscoelastic actomyosin network and can serve as a starting point for testing the effects of biochemical signaling that takes place during neurodevelopment. For instance, actin depolymerization promotes actin network turnover by binding ativities of LIMK-1 and cofilin. The changes in G-actin concentration can be sufficient to increase the filopodium motility or on the contrary, if depolymerization is very high, to halt filopodium growth. Since

G-actin concentration is not addressed in our model, including an additional species will be necessary prerequisite for detailed modeling of biochemical signals.

After understanding filopodia dynamics and stability, we set out to answer the question about dendritic spine morphogenesis in the neurodevelopmental disorders. We compared dendritic process arborization, dendritic protrusion density, and filopodia density and motility in hiPSC-derived neurons from Dup15q, Angelman Syndromes and control subjects. The data suggests that neurons derived from Dup15q Syndrome patient cells have significantly greater process arborization, dendritic protrusion density and filopodia motility compared to the control parameters, while Angelman neurons have less developed processes and fewer dendritic protrusions. All cultures analyzed were positive for PSD95, MAP2 and SynI markers indicating presence of mature neurons at 28 weeks and beyond.

One of the technical difficulties of the experimental system described in Chapter 4 was presented by the data acquisition approach. Imaging over large confocal volumes is challenging and requires long hours of scanning to capture the details required for correct identification of neurons and dendritic protrusions in sufficient numbers for data analysis, even with automatization. Given recent development in the fluorescent labeling and image processing techniques, a more effective and accurate approach can be implemented. First, two-photon imaging has a distinct advantage in 3D imaging and reconstruction of neuron morphology and allows use of brain tissue, in our case slices (or organotypic slices) prepared from patient-specific iPSC-derived brain organoids. Second, genetic labeling is required to highlight the neurons of the desired type. For example, highlighting dopaminergic neurons by inserting luciferase reporter into the tyrosine hydroxylase gene locus would eliminate uncertainty on the cell type and allow to select the excitatory neurons among inhibitory and other cell types such as astrocytes and glia (Cui et al. 2016) Presynaptic and postsynaptic marker pairs (PSD95 and Synapsin I and/or Gephyrin and Synapsin I) and NMDA/AMPA receptors (surface) would be used to quantify functional synapses and evaluate the quality of the synaptic connection.

This approach would not only enhance the significance of findings in Angelman and Dup15q Syndrome cells but allow development and optimization of various drug trial assays. As in any experiments concerning the neural tissue, where variability in neuronal architecture is vast, sufficient number of experiments for organoids and variations of the cell lines should be used to confirm the results.

Finally, to understand dendritic spine formation and consolidate neurotypical and patient-derived synaptogenesis we developed 2D PDE model of dendritic spine growth.

This project benefited immensely from an interdisciplinary approach. In an expensive and time-demanding experimental setting, a possibility to model neurodevelopmental scenarios is crucial for selecting the most promising treatment. Furthermore, complex pathways that are involved in the spine maturation would be modeled to understand possible main and off-target effects for the treatments of interest.

5.2 2D Model Formulation and Governing Equations

To lay the foundation for the third question, I conducted a preliminary studies to develop a 2D spine model with realistic geometry on a moving boundary, that can be modified to include biochemical pathways and neurodevelopmental events during spine morphogenesis: actin cytoskeleton remodeling, myosin contractility and adhesion to the cell surface.

Changes to filopodia shape introduced by an encounter with a barrier will inevitably alter the actin flow pattern. As the polymerization sites redistribute from the filopodia tip, the actin flow directions will also redistribute. Because there are multiple sites of polymerization along the spine head, we expect to see formation of heterogeneously directed actin flows in spine heads (Honkura et al.2008, Tatavarty et al. 2009). Actin dynamics of spine head is complex and has not been characterized in culture or in vivo. Here we will use mathematical modeling to describe actin dynamics in spine head and its contribution to spine shape. Because myosin II is required for spine formation in vivo and in culture (Rex et al, 2008) and is known to maintain the direction of actin retrograde flow in both filopodia and thin spine necks (Craig et al. 2012; Tatavarty et al. 2012), we hypothesize that myosin II activity is crucial in establishing and maintaining the heterogeneous flow of actin in the spine head. Since velocity of actin flow increases due to

myosin crosslinking and contractile activity, we hypothesize that myosin will accumulate at the base of the spine head, where the flow is the slowest(Chazeau & Giannone 2016). Indeed, single molecule PALM data for myosin light chain shows localization in the head of the spines where myosin is presumed to migrate from the base of the filopodia (Tatavarty 2012). To test our qualitative hypothesis for spine formation mechanism, we expanded the 1D model described in Chapter 2 to 2D *(Eq. 12-13)* with boundary conditions that describe adhesive contact between filopodium and axon cell membranes *(Eqs 14-16).* We assume there is no bound myosin at the base B. The shape of the spine is computed based on the polymerization rate at the tip and by actin flow *(Eq.18)*

Main equations:

$$\eta\Delta\mathbf{v} + \sigma_{\mathbf{0}}\nabla m_b = \varsigma\mathbf{v} \qquad (12)$$

$$\frac{\partial m_b}{\partial t} = D\Delta m_b - \nabla(m_b\mathbf{v}) + k_{on}m - k_{off}m_b \qquad (13)$$

Boundary Conditions:

$$\mathbf{v}|_{x\in B} = -0|_{x\in B} \qquad (14)$$

$$\hat{\mathbf{n}}\cdot(\eta\nabla\mathbf{v} + \sigma_0 m_b)|_{x\in M\cup B} = -T\kappa \qquad (15)$$

$$\hat{\mathbf{n}}\cdot(\mathrm{D}\nabla m_b - \mathbf{v}m_b)|_{x\in M\cup B} = 0 \qquad (16)$$

$$m_b|_{x\in B} = 0 \qquad (17)$$

Moving boundary kinematics:

$$\hat{\mathbf{n}}\frac{\partial\mathbf{r}}{\partial t} = \mathbf{v}\cdot\hat{\mathbf{n}} + v_p \qquad (18)$$

Variables:

v- velocity of actin network

m_b - active myosin bound to actin cytoskeleton concentration

Parameters:

D – Diffusion coefficient

m unbound myosin concentration

k_{on} – myosin binding rate

k_{off} – myosin unbinding rate

σ_0 – myosin contractility

η – viscosity of actin network

ζ – drag force

$T\kappa$ – membrane tension and curvature

As in the previous model, behavior of viscoelastic actin is described by force balance equation *(Eq.12)* coupled with mass balance equations for myosin *(Eqs.13)*. We assume that filopodium contact with axon is required for establishment of spine morphology and we start simulation from steady-state mushroom shape (*Figure 5.2*). This imposes a non-slip condition on the axon-spine head boundary, since the actin flow near the boundary becomes zero (*Eq. 15*). The zero velocity at the boundary will give rise to the velocity gradient creating a boundary layer. The size of the boundary layer will depend on actin viscosity times the velocity gradient (Landau and Lifshitz 1987). We assume that the flow of actin into the dendrite is prevented by the resistive force from the spine lower boundary B (Eq. 14). We assume that Axon-dendrite contact is restricted only to the portion of upper boundary (d1-d2), and the actin polymerization is set to a function along a membrane M. We will test a range of Vp functions to define which spatiotemporal organization of polymerization sites leads to steady mushroom shaped/stubby spines. The free-boundary expansion of the membrane meets resistance from the force due to membrane tension(Eq.16). The shape of the spine is computed based on the polymerization rate at the tip and actin velocity (Novak & Slepchenko

2014)(Eq. 18). Thus, the 2D model variables are: F-actin velocity, F-actin and bound myosin concentration, spine shape, actin polymerization. Model parameters are: viscosity, substrate drag coefficient, myosin binding/unbinding rates, myosin contractility, bound myosin diffusion, base resistive force. After we determined which actin polymerization function is suitable for generating stable solutions on fixed boundary, we can proceed to simulate the filopodia tip contact with axon and determine actin dynamics necessary for tip enlargement and consequent spine head formation. Then, we will study the effect of various actin polymerization functions on the spine shape and compare the simulation results with the spine morphologies observed in Chapter 4.

5.3 Preliminary Results on Fixed Boundary

The stable solution for the model on fixed boundary *(Figure 5.3*) demonstrates gradient of myosin concentration in the spine head with maximum myosin activity localized in the base. This results is in agreement with the latest experimental findings(Chazeau & Giannone 2016). The distribution of the actin polymerization along the M region also shows maximum values of actin polymerization at the d1-d2 region of the spine head. From the results on fixed boundary, we hypothesize that the filopdium tip incorporates additional actin polymerization sites and expands radially to form spine head with dynamic actin network inside (*Figure 5.4*). To validate this model we plan to solve the equations defined on the moving boundary with the parameters identified.

5.4 Integrating UBE3A and RhoA Signaling into Spine Morphology Model

Unique properties of the dendritic spine include its plasticity and a multitude of biochemical pathways that converge on dendritic spine actin cytoskeleton. Modeling these interactions presents a challenge in deciding which physical properties of actin cytoskeleton are affected by an upstream regulator like UBE3A, where information on biochemical interactions is limited. For example, CYFIP1 (Cytoplasmic FMRP-interacting protein 1) – which is overexpressed in Dup15q - activates Rac1, that is known to

stabilize F-actin via increased actin polymerization, and thus increases F-actin pool and actin retrograde flow in dendritic spines. This effect can be reproduced in the 2D model by changing actin polymerization function v_p, and/or actin viscosity η . UBE3A is a powerful regulator of synapse development in both Dup15q and AS syndromes and is also upstream the Rac pathway as described in Chapter 1. Thus, modeling the effect of UBE3A and CYFIP1 overexpression/absence on synaptic development should be started from introducing an additional parameter that modifies actin polymerization function and F-actin pool fraction in the spine head accordingly.

Figures.

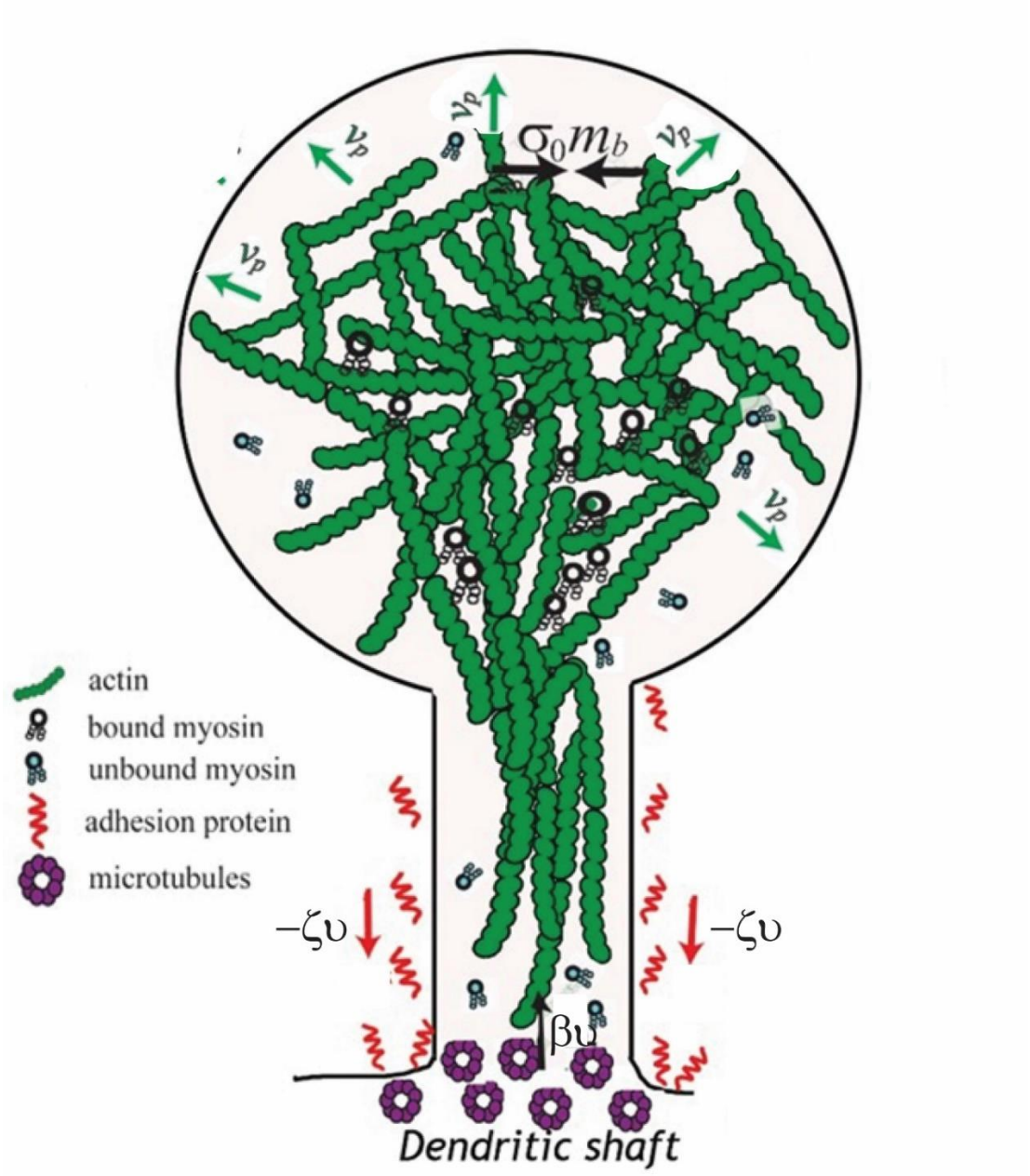

Figure 5.1 Cartoon that illustrates the balance of forces in a dendritic spine described by the 2D PDE model. The model captures five essential processes: a) polymerization of F-actin at periphery of the spine head; b) binding and unbinding of myosin to F-actin network; c) isotropic contractile stresses exerted by bound myosin on F-actin; d) viscous flow of F-actin (ARF) induced by these contractile stresses and membrane tension; e) friction between the spine

membrane and the substrate due to adhesion. Bound myosin contractile stress is shown by blue arrows σ_0, m_b, v_p - polymerization rate, ζv – the substrate adhesion force is denoted by the red arrow, and black arrow is βv– resistance force at the base due to microtubule network inside the dendrite. Unbound myosin freely diffuses inside the spine.

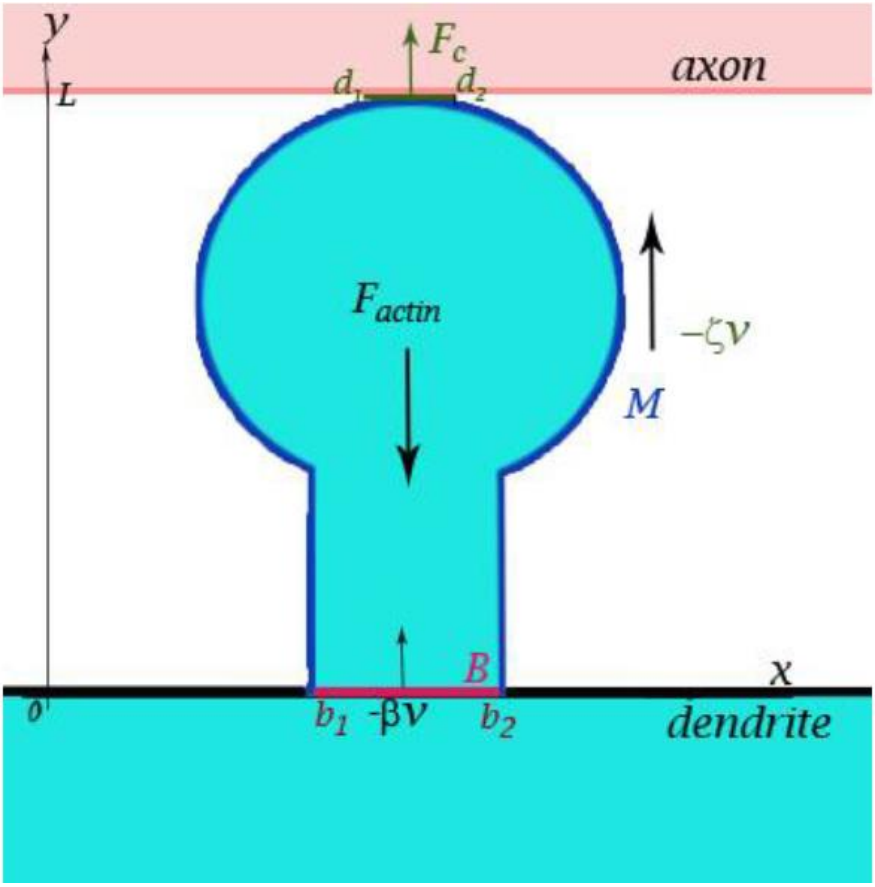

Figure 5.2 Dendritic spine boundary conditions schematics. M – boundary for the spine head, B $[b_1\text{-}b_2]$ – boundary for the base of the spine, $[d_1\text{-}d_2]$ – region of contact, where $v_p=0$, L – length of the spine, x – dendrite. Factin-actin retrograde flow inside spine, –βv– resistive force inside the spine. ζv- drag force

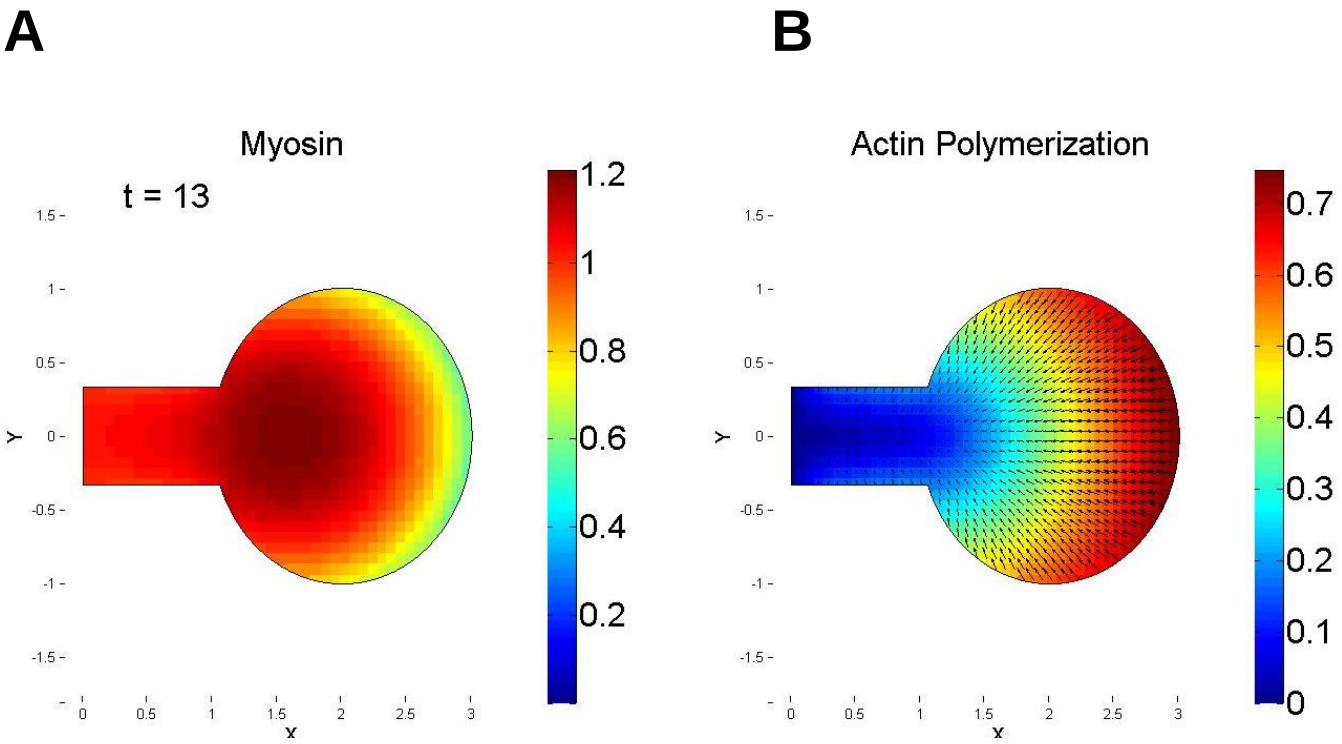

Figure 5.3 Distribution of bound myosin (A) and actin polymerization (B) in a fixed boundary solution. A. At steady-state the distribution of active myosin concentration (heat map) inside spine head solved on fixed boundary. B. Actin polymerization (vp) gradient in the spine head at steady- state solved on fixed boundary. Parameters used*:* D =0.1, $\eta = 2$, $\zeta = 0.5$, $\sigma = 0.3$, $k_{on} = 1$, $k_{off} = 1$

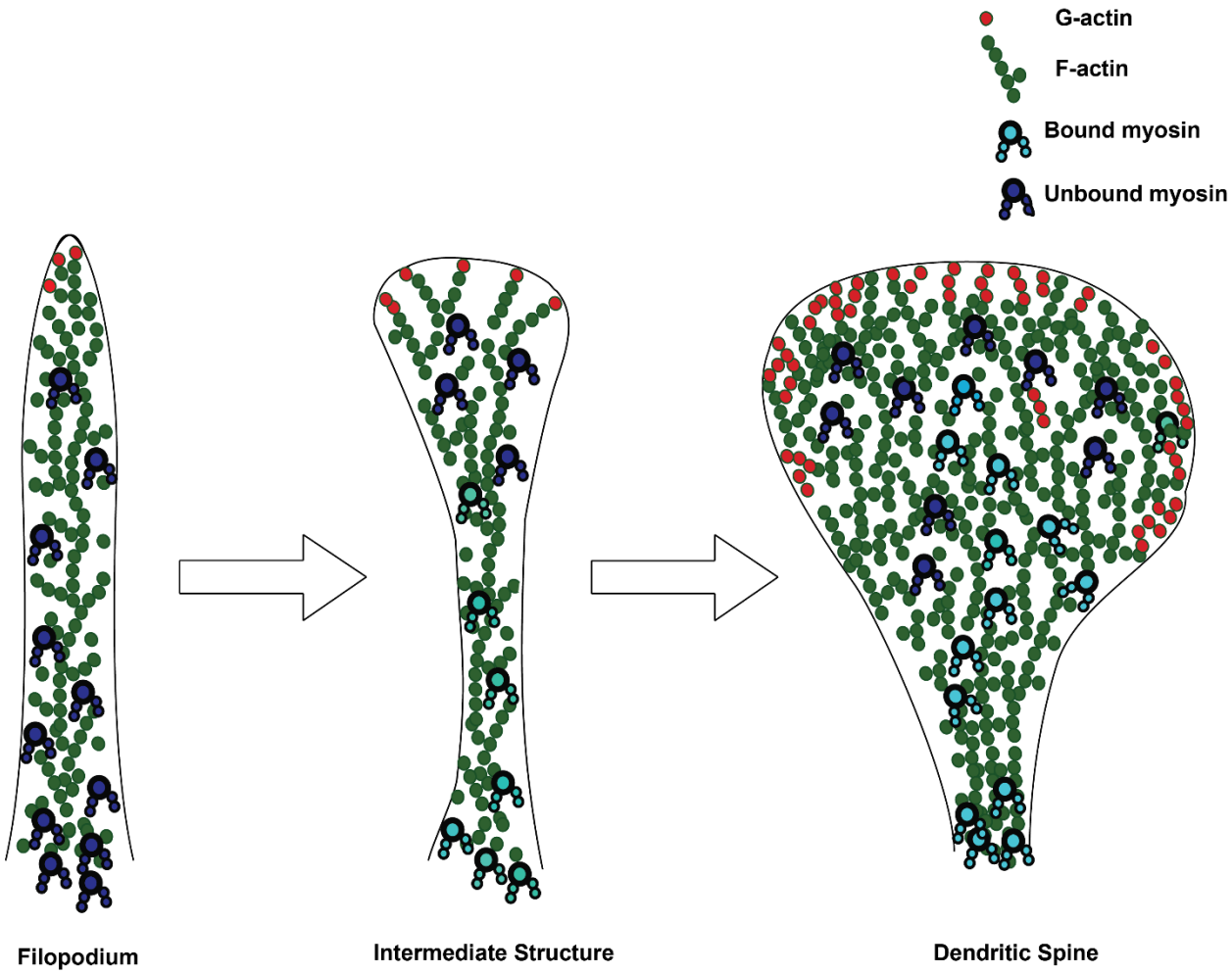

Figure 5.4 Model of Spine Morphogenesis. The cartoon depicts expansion of filopodial head during the transition into dendritic spines. Incorporation of one or any combination of these processes widens the list of questions that can be answered in regards to the modeling of dendritic spine morphogenesis and neurodifferentiation.

Bibliography

Chazeau, A. & Giannone, G., 2016. Organization and dynamics of the actin cytoskeleton during dendritic spine morphological remodeling. *Cellular and Molecular Life Sciences*, pp.1–21.

Craig, E.M. et al., 2012. Membrane tension, myosin force, and actin turnover maintain actin treadmill in the nerve growth cone. *Biophysical Journal*, 102(7), pp.1503–1513.

Cui, J. et al., 2016. Quantification of dopaminergic neuron differentiation and neurotoxicity via a genetic reporter. *Scientific Reports*, 6(April), p.25181.

Korobova, F. & Svitkina, T., 2010. Molecular Architecture of Synaptic Actin Cytoskeleton in Hippocampal Neurons Reveals a Mechanism of Dendritic Spine Morphogenesis. *Molecular Biology of the Cell*, 21, pp.165–176.

Novak, I.L. & Slepchenko, B.M., 2014. A conservative algorithm for parabolic problems in domains with moving boundaries. *Journal of computational physics*, 270, pp.203–213.

Tatavarty, V., Das, S. & Yu, J., 2012. Polarization of actin cytoskeleton is reduced in dendritic protrusions during early spine development in hippocampal neuron. *Molecular Biology of the Cell*, 23(16), pp.3167–3177.